Semiconductor Photocatalysis

Electronic Hole Trapping in TiO2

Zawadzki, Pawel; Rossmeisl, Jan; Jacobsen, Karsten Wedel

Publication date:
2011

Document Version
Publisher's PDF, also known as Version of record

Citation (APA):
Zawadzki, P., Rossmeisl, J., & Jacobsen, K. W. (2011). Semiconductor Photocatalysis: Electronic Hole Trapping in TiO2. Technical University of Denmark, Center for Atomic-Scale Materials Physics.

Semiconductor Photocatalysis: Electronic Hole Trapping in TiO_2

Paweł Zawadzki

Ph.D. Thesis
Kongens Lyngby, 2011

Technical University of Denmark
Department of Physics
Center for Atomic-scale Materials Design
DK-2800 Kongens Lyngby, Denmark
Phone +45 4525173, Fax +45 45932399
www.camd.dtu.dk

Abstract

Photocatalysis (the acceleration of a photoreaction in the presence of a catalyst) is presently used in large variety of applications and is one of the possible strategies for future sustainable fuel production from solar energy. A general picture of a photocatalytic process is well known: photogeneration of electron-hole pairs, excess carrier transport to distinct reactive sites and finally carrier utilization in a chemical reaction. For most photocatalyst a detailed understanding of these steps, however, is lacking yet it is crucial to elucidate photocatalyst limitations. Of particular importance is gaining insight into the nature of photogenerated carriers as they play a central role in all the basics steps of a photocatalytic process.

The main objective of this thesis is to elucidate the experimentally observed localized nature of photogenerated electron holes in titanium dioxide—the most studied, yet poorly understood photocatalyst.

By means of the density functional theory (DFT) and its simple extension, the linear expansion Δ self-consistent field DFT, it is shown that in TiO_2 the photogenerated holes self-trap forming O^- small polarons. Self-trapping strength is significantly modified in surface layers due to the variation of surface electrostatic potential. This finding explains differences in photooxidative properties among rutile and anatase TiO_2 facades.
Optical absorption spectra and hole hopping mobilities of the O^- centers in TiO_2 have been calculated. Since time resolved optical spectroscopies are common techniques to study hole dynamics in TiO_2 these results should aid analysis of photocatalytic processes on TiO_2.

Apart from photocatalysis this thesis also deals with the problem of the localization/delocaliztion error in approximate DFT functionals—the effect of the incorrect, nonlinear description of fractional electron systems by approximate exchange-correlation functionals. It is shown that by removing the total energy nonlinarlity a more consistent description of states with different degrees of localization can be achieved.

Resumé

Fotokatalyse (accelerationen af en fotokemisk reaktion ved tilstedeværelsen af en katalysator) er nu om dage brugt i mange forskellige anvendelser og er en af de mulige strategier for fremtidig vedvarende produktion af brændstof fra solenergi. Det generelle billede af en fotokatalytisk proces er velkendt: Dannelse af elektron-hul par ved fotoeksitation, transport af overskydende ladningsbærere til bestemte reaktive sites og til slut udnyttelsen af ladningsbæreren i en kemisk reaktion. En detaljeret forståelse af disse skridt er dog, for de fleste fotokatalysatorer, mangelfuld, det er dog en vigtig ting at få undersøgt for at forstå begrænsningerne for fotokatalysatorer. Det er særligt vigtigt at få indsigt i de foto-genererede ladningsbæreres natur, da de spiller en central rolle i alle de basale trin af en fotokatalytisk proces.

Hovedformålet med denne afhandling er at belyse de foto-genererede elektron-hul pars eksperimentelt observerede lokaliserede natur i titandioxid—den mest undersøgte, men alligevel lidet forståede fotokatalysator.

Ved hjælp af tæthedsfunktional teori (density functional theory—DFT) og dens simple forlængelse; den lineære ekspansions Δ selvkonsistente felt DFT, har vi vist at i TiO_2 bliver de foto-genererede huller selvfanget og danner små O^- polaroner. Styrken af selvfangningen er signifikant forandret i overfladelag grundet variation i overfladepotentialet. Denne opdagelse gjorde det muligt for os at forklare forskellene i de foto-oxidative egenskaber mellem rutil og anatase TiO_2 facetter. Vi har også for O^- centrene i TiO_2 beregnet de optiske absorptionsspektre og hullernes hop-mobilitet. Da tidsligt opløst optisk spektroskopi er en normal teknik til at undersøge hullernes dynamik i TiO_2 burde vores resultater kunne hjælpe analysen af de fotokatalytiske processer på TiO_2.

Udover fotokatalyse handler denne afhandling også om problemet med delokaliserings fejlen i ikke-eksakt DFT, dvs. effekten af den ukorrekte ikke-lineære beskrivelse af ikke-heltallige elektronsystemer med ikke-eksakte XC funktionaler. Vi har vist at en mere konsistent beskrivelse af tilstande med forskellige grader af lokalisering kan opnås ved at fjerne den ikke-lineære del af den totale energi.

Preface

This thesis was prepared at the Center for Atomic-scale Materials Design, the Technical University of Denmark in partial fulfillment of the requirements for acquiring the Ph.D. degree.
The main focus is on the effects of photogenerated holes trapping on photocatalytic properties of titanium dioxide. The results are based on density functional theory (DFT) calculations.

It is a pleasure to thank those who made this thesis possible. I wish to express my gratitude to my supervisor, Prof. Jan Rossmeisl for the continuous support of my Ph.D. study and research, for his patience and enthusiasm. I am deeply grateful to my supervisor, Prof. Karsten Wedel Jacobsen for his immense knowledge and great efforts to explain things clearly and simply.
I would like to thank all the CAMD stuff for creating great working atmosphere, it was a privilege to work with you. Special thanks to Dr. Marcin Dułak for proofreading the complete thesis and Ivano E. Castelli, Jón Steinar Garðarsson Mýrdal, Dr. Vladimir Tripkovic, Dr. Georgios Tritsaris for proofreading parts of this thesis. I wish to thank Steen Lysgaard for translating the abstract into Danish.

Last but not least, I would like to thank my entire family for their support throughout the years.

Kongens Lyngby, December 2011
Paweł Zawadzki

Papers included in the thesis

- [I] **Zawadzki P.**, Jacobsen K. W., Rossmeisl J.; Electronic hole localization in rutile and anatase TiO_2—Self-interaction correction in Δ-SCF DFT. *Chemical Physics Letters* **506** 42 (2011) doi:10.1016/j.cplett.2011.03.001
- [II] **Zawadzki P.**, Rossmeisl J., Jacobsen K. W.; Electronic hole transfer in rutile and anatase TiO_2: Effect of a delocalization error in the density functional theory on the charge transfer barrier height. *Physical Review B* **84** 121203 (2011) doi:10.1103/PhysRevB.84.121203
- [III] **Zawadzki P.**, Rossmeisl J., Jacobsen K. W.; Polaronic defect states from (semi)local DFT. Application of Δ-SCF DFT to optical absorption of the V^- center in MgO. (manuscript)
- [IV] **Zawadzki P.**, Jacobsen K. W., Dahl S., Rossmeisl J.; Explaining oxidative trends of TiO_2—Hole trapping at anatase and rutile surfaces. (manuscript)
- [V] **Zawadzki P.**; Transient absorption spectra of anatase TiO_2. (manuscript)

Contents

CHAPTER 1

Introduction

Titanium dioxide (TiO_2) is an abundant, chemically inert (in dark) and harmless material. These excellent technological properties translate into a widespread use of this material. In large quantities, TiO_2 is used as a white pigment for paints, plastics, paper, fibres, etc. Its whitening properties, in fact, have been known since ancient times.

TiO_2, while chemically inert material in dark, in UV light becomes a powerful photocatalyst. The photocatalytic potential of TiO_2 has already revealed itself in flaking and bleaching of paints [1].
Research on TiO_2 photocatalysis accelerated after Fujishima and Honda published paper on photolytic water decomposition [2]. This discovery in the time of the oil crisis of 1970s triggered hopes for hydrogen fuel based economy. The conversion of solar energy to chemical in a form of hydrogen fuel could provide sustainable solution for rising energy needs. It has been, however, quickly recognised that TiO_2 efficiency for hydrogen production is far too low for having a chance to be competitive to fossil fuels—TiO_2 large band gap allows to harvest only 3% of the solar spectrum [3]. Nevertheless, TiO_2 remains one of the few materials that are able to split water without a use of sacrificial agents.

Photocatalytic properties of TiO_2 have much more to offer than the catalysis of the photochemical water splitting reaction. Photogenerated holes in TiO_2 are strong oxidising agents for organic compounds [4–6]. Applications for water

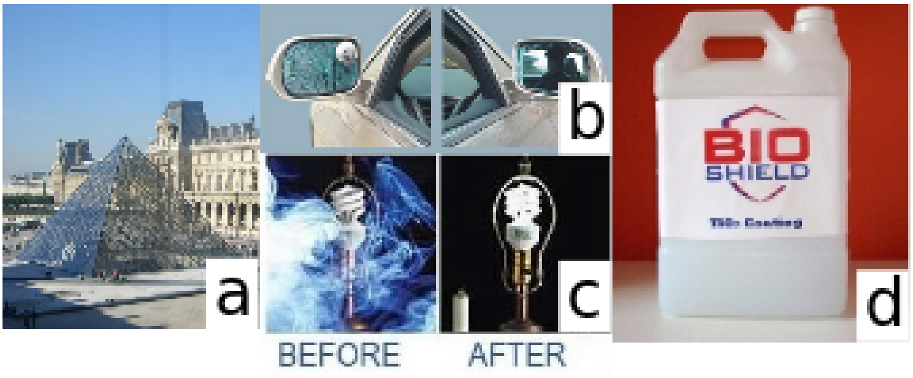

Figure 1.1: Example applications of TiO_2 photocatalytic properties: a) self-cleansing coating on Louvre pyramid, b) anti-fogging mirrors, c) air purifying bulb, d) bacteria killing water bottle.

and air purification systems, bacteria killing coatings or anti-fogging mirrors, to name a few, have already entered the market and are enjoying growing demand (see Fig. 1.1 for illustration).

A basic picture of the semiconductor photocatalysis comprises: photogeneration of electron-hole pairs, they transport to surface reactive sites where they take part in chemical transformations [7–11] (see Fig. 1.2). A detailed, atomic-scale insight into these steps is often lacking, yet it is necessary to elucidate photocatalyst limitations and opportunities. The first step to gain such an insight is to understand the nature of photogenerated carriers as they play a central role in the basic steps of a photocatalytic process.

The electron paramagnetic resonance of UV irradiated TiO_2 samples detects localized hole and electron centers on oxygen and titanium atoms, respectively [12–22]. Transient absorption spectroscopy further revels that the electrons co-exist in free and localized states whereas holes are predominately trapped [23–29]. The exact atomic structure, energetics and distribution of trapping sites is, however, unclear. Particularly important is the elucidation of hole trapping as holes are minority carriers (TiO_2 is an n-type semiconductor). Trapping of photogenerated holes might significantly influence their distribution and transport, and, thus photocatalytic processes.

Despite large amount of experimental data, there have been only few computational studies of charge trapping in TiO_2, see for instance Ref. [30–35]. The reason for this is that the most common computational technique—the semi-

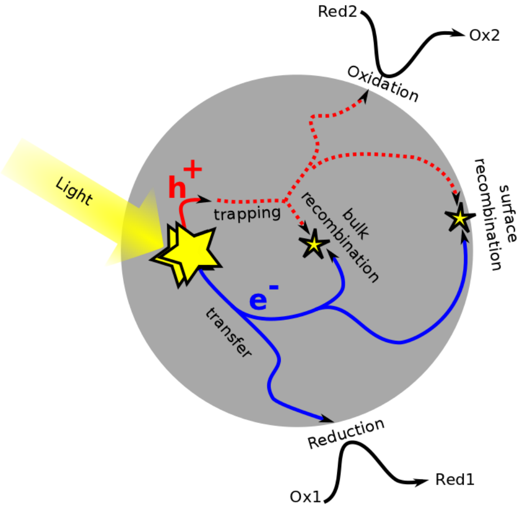

Figure 1.2: Schematic illustration a photocatalytic process. Photogenerated electron-hole pairs in a semiconductor particle separate and transfer to surface reactive sites where they take part in chemical transformations.

local density functional theory—often fails to provide even a qualitative picture of charge localization in crystals [36–40].

The aim of this thesis is to provide insight into the atomic and the electronic structure as well as the spacial distribution of hole trapping centers in TiO_2.

In order to achieve this goal in chapter 2 I first provide a basic introduction to the density functional theory (DFT)—the computational method used in this thesis. Then, chapter 3 discusses charge trapping in crystals. Here, the focus is on small polarons (charge–polarisation field quasiparticles with size comparable to a lattice spacing), and on the physical origins of trapping. This chapter discusses formation of hole small polarons in TiO_2 bulk and in surface layers. In the next chapter, chapter 4, I discuss the application of DFT for description of charge trapping in crystals. The method, due to the total energy nonlinearity problem, often fails to provide even a qualitative picture of charge localization/delocaliztion processes. This chapter provides a simple correction that allows, in some cases, to overcome this issue. Having introduced the tools and concepts, I apply DFT to small polaron optical transitions in chapter 5 and to small polaron mobility in chapter 6. Finally, chapter 7 analyzes the effects of charge trapping on TiO_2 photocatalytic properties.

This thesis also discuses the V^- center in MgO (singly charge Mg vacancy) (chapters 3, 4 and 5). This system served as a test case for the application of DFT to charge localization/delocaliztion processes.

CHAPTER 2

Density Functional Theory

The density functional theory (DFT) is the most common computational technique to study materials properties at atomic scale. Starting from the Born-Oppenheimer approximation the method replaces the wave function based description of an atomic system with a computationally more efficient formulation based on the electron density.

This Chapter discusses the basics of DFT. I start by providing founding theorems by Hohenberg and Kohn (HK) and discuss their applicability to fractional electron systems and excited states. The Kohn Sham equations—the most common realization of DFT—is described in Section three. The last section discusses the linear expansion Δ self-consistent field DFT—a simple extension of the conventional DFT.

2.1 Foundations

The idea that the energy of the electron system can be expressed as a functional of its density reaches 1930s when independent works of Llewellyn Hilleth Thomas [41] (1926) and Enrico Fermi [42] (1927) showed that the kinetic energy of the electron gas in a metal is a functional of the electron density.

The modern theory is based on two theorems by Hohenberg and Kohn [43].

Theorem 1 (Hohenberg and Kohn) *The ground-state electronic density* $\rho_0(\vec{r})$ *and the ground-state wave-function* Ψ_0 *can be used alternatively as full descriptions of the ground state of the system.*

This theorem holds for an arbitrary external potential in the absence of magnetic filed. The density therefore uniquely (up to a trivial constant) defines the external potential, and thus all the properties of the system. This property of the density is termed v-representability.
If an external potential is due to atomic nuclei, the theorem can be justify in a particularly simple manner: Given the electron density $\rho(\vec{r})$ one can identify positions of the nuclei by examining the density for cusps. The atomic number Z_a of the nucleus a at position R_a then can be determined using the cusp condition [44]:

$$Z_a = \frac{1}{2\rho(\vec{r})} \frac{\partial \rho(\vec{r})}{\partial r}\Big|_{r=R_a}, \tag{2.1}$$

which ensures that the wave-function (and the density) does note explode to the infinity at $r = R_a$. The total number of electrons is simply the integral over the density. Having the positions of the nuclei, their atomic numbers and the total number of electrons, the Hamiltonian can be constructed and, in principle, solved for the ground state wave function.

The second theorem provides a practical tool for calculating the ground state energy—a variational principle.

Theorem 2 (Hohenberg and Kohn) *For a given number of electrons and external potential* v*, there exists a functional of* ρ*,* $E_v[\rho]$*, for which the following variational principle is satisfied* $E_v[\rho] \geq E_v[\rho_0] = E_0$*, where* ρ_0 *stands for the ground state electronic density and* E_0 *is the ground state energy.*

Levy proved that such functional can be constructed from densities that are N-representable—nonnegative, continues, and integrable to N electrons—a set that is more easily defined than v-representable densities [45]. The prove is realized via two step constraint minimization:

- over all N-electron, normalized wave-functions Ψ_N that give a certain density ρ,
- over all densities ρ that integrate to N electrons.

$$E_0 = \min_{\rho \to N} \min_{\Psi_N \to \rho} \langle \Psi_N | H | \Psi_N \rangle, \tag{2.2}$$

where H consist of the electron kinetic energy T, the electron repulsion U and the electron interaction with the external potential $v(\vec{r})$. Since the latter is simply

$$V[\rho] = \int v(\vec{r}) \rho(\vec{r}) \mathrm{d}^3\vec{r}, \tag{2.3}$$

the variational principle for the ground state energy can be realized as minimization over the set of N-representable densities.

$$E_0 = \min_{\rho \to N} \left\{ V[\rho] + F_{\mathrm{HK}}[\rho] \right\}, \tag{2.4}$$

where $F_{\mathrm{HK}}[\rho]$ is universal, v-independent functional of the electron density.
The exact form of $F_{\mathrm{HK}}[\rho]$ is unknown and for practical implementations approximate constructions are used. The most common is the Kohn-Sham model of a fictitious noninteracting electron system which is described in Section 2.2.

2.1.1 Noninteger electron numbers

Eq. 2.4 constrains the minimisation to densities ρ that integrate to N electrons

$$\int \rho(\vec{r}) \mathrm{d}^3 r = N. \tag{2.5}$$

Such minimization realized via introduction of a Lagrange multiplier μ

$$\frac{\delta [E_v[\rho] - \mu \int \rho(\vec{r}) \mathrm{d}^3 r]}{\delta \rho} = 0, \tag{2.6}$$

allows the electron density integral to assume a fractional value. For a closed system fractional electron numbers does not have any physical significance. They may arise, however, in an open system as a time average over an ensemble of pure states. System with $N+\omega$ electrons and $\omega \in [0,1]$ is thus a statistical mixture of an N electron system with the probability $1-\omega$ and an $N+1$ electron system with the probability ω [46].
The variational principle can be realized as a two step constrained search: minimization of the energy over ensembles that yield the given density and minimization over all densities that integrate to the given electron number $N+\omega$

$$E_0 = \min_{\rho \to N+\omega} \min_{\Psi_N, \Psi_{N+1} \to \rho} \left\{ (1-\omega) \langle \Psi_N | H | \Psi_N \rangle + \omega \langle \Psi_{N+1} | H | \Psi_{N+1} \rangle \right\}. \tag{2.7}$$

For such statistical mixture subjected to an external potential v the minimum of the energy is attained for:

$$\rho_{N+\omega} = (1-\omega)\rho_N + \omega\rho_{N+1}, \tag{2.8}$$

and

$$E_{N+\omega} = (1-\omega)E_N + \omega E_{N+1}. \tag{2.9}$$

The energy is therefore linear in segments between integer electron numbers.

2.1.2 Excited states

The excited state density does not uniquely define the external potential and therefore Hohenberg-Kohn theorems are invalid for excited states [47]. The variational principle for ith excited state requires knowledge of $i-1$ lowest states of the Hamiltonian so that minimization can be performed over subset of Hilbert space orthogonal to $i-1$ levels.

To realize the variational principle for the excited density, Levy's two step constraint search can be employed. The first minimization is performed over all wave-functions that are orthogonal to the lowest $i-1$ states of the Hamiltonian and give excited state density ρ. The second minimization is a search over all densities that integrate to the total number of electrons N.

$$E_i = \min_{\rho\to N} \min_{\substack{\Psi_N\to\rho \\ \Psi_N\perp\Psi_N^0,\ldots,\Psi_N^{i-1}}} \langle\Psi_N|H|\Psi_N\rangle. \tag{2.10}$$

Similarly to Eq. 2.4 the excited state energy functional takes the form

$$E_i = \min_{\rho\to N}\left\{\int v(\vec{r})\rho(\vec{r})\mathrm{d}^3\vec{r} + F_i[\rho,\rho_0]\right\}. \tag{2.11}$$

Now, since the knowledge of the $i-1$ lowest excited states is required, the energy is bifunctional of the ground state density (or potential) and the excited state density.

For Coulombic external potentials the cusp condition (or its modified version) also holds for excited state densities [48], therefore the Hamiltonian can be constructed, in a way described in Sec. 2.1, from the exact excited state density. Finding the exact excited state density however, is highly nontrivial as requires knowledge of $F_i[\rho,\rho_0]$.

2.2 Kohn-Sham equations

The exact form of the universal functional $F_{\mathrm{HK}}[\rho]$ is unknown and for practical implementations approximate constructions are used. Kohn and Sham proposed a scheme that replaces the problem of interacting many electron system with a noninteracting electron gas in a fictitious effective potential v_{eff} so that the exact ground state density of the system is reproduced. Electrons are hence described by a single particle Schrödinger equations[1]

$$\left(-\frac{1}{2}\Delta + v_{eff}\right)|\psi_n\rangle = \varepsilon_n|\psi_n\rangle. \tag{2.12}$$

The wave function of noninteracting many electron system is a Slater determinant constructed from the KS orbitals $|\psi_n\rangle$ and the total electron density of the N electron system is

$$\rho(r) = \sum_n^N |\psi_n|^2. \tag{2.13}$$

Kohn-Sham's construction of the potential v_{eff} is based on energy expression

$$E[\rho] = T_0 + V[\rho(\vec{r})] + J[\rho(\vec{r})] + E_{xc}[\rho(\vec{r})], \tag{2.14}$$

where T_0 is the kinetic energy of the Kohn-Sham system

$$T_0 = -\frac{1}{2}\sum_n^N \langle\psi_n|\Delta|\psi_n\rangle, \tag{2.15}$$

$V[\rho(\vec{r})]$ is the interaction with an external potential $v(\vec{r})$

$$V[\rho(\vec{r})] = \int v(\vec{r})\rho(\vec{r})\mathrm{d}^3\vec{r}, \tag{2.16}$$

$J[\rho(\vec{r})]$ is the electron density self-interaction

$$J[\rho(\vec{r})] = \frac{1}{2}\int \frac{\rho(\vec{r})\rho(\vec{r'})}{|\vec{r}-\vec{r'}|}\mathrm{d}^3\vec{r'}, \tag{2.17}$$

and E_{xc} accounts for the exchange and correlation effects as well as for the difference in kinetic energy between the real (interacting) electron and the fictitious noninteracting Kohn-Sham systems.

By minimizing the energy functional with respect to change in Kohn-Sham orbitals, the potential v_{eff} is found to be

$$v_{eff} = v_c + v_{xc} + v, \tag{2.18}$$

---

[1] atomic units apply $m_e = \hbar = a_0 = e = 1$

where v_c is the Coulomb potential due to the electron density

$$v_c(\vec{r}) = \int \frac{\rho(\vec{r'})}{|\vec{r} - \vec{r'}|} \mathrm{d}^3\vec{r'}, \tag{2.19}$$

v_{xc} is the exchange correlation potential

$$v_{xc}(\vec{r}) = \frac{\delta E_{xc}[\rho(\vec{r})]}{\delta\rho(\vec{r})}, \tag{2.20}$$

and v is the external potential.

2.2.1 Exchange-correlation energy

The exchange-correlation energy E_{xc} is the only unknown component of the total energy expression for the Kohn-Sham system Eq. 2.14. A physical insight into this term can be gained through the adiabatic-connection approach. The method introduces scaled electron-electron interaction $\lambda U(\vec{r}, \vec{r'})$ where $\lambda \in [0, 1]$ and an external potential v_{ext}^{λ} chosen so that for all λ the electron density equals to the true density. The external potential for $\lambda = 0$ is the effective Kohn-Sham potential whereas for $\lambda = 1$ is the true external potential. The method leads to the following expression for exchange correlation energy:

$$E_{xc}\left[\rho\left(\vec{r}\right)\right] = \int_0^1 \langle \Psi_\lambda | U | \Psi_\lambda \rangle \mathrm{d}\lambda - J\left[\rho\left(\vec{r}\right)\right], \tag{2.21}$$

which can be cast into form

$$\begin{aligned} E_{xc}\left[\rho\left(\vec{r}\right)\right] =& \frac{1}{2} \int \rho(\vec{r}) \frac{\rho_{xc}(\vec{r}, \vec{r'})}{|\vec{r} - \vec{r'}|} \mathrm{d}\vec{r} \mathrm{d}\vec{r'} & (2.22) \\ =& \int \rho\left(\vec{r}\right) \epsilon_{xc}\left[\rho\left(\vec{r}\right)\right] \mathrm{d}\vec{r}, & (2.23) \end{aligned}$$

where $\rho_{xc}(\vec{r}, \vec{r'})$ is the exchange correlation hole averaged over λ and $\epsilon_{xc}\left[\rho\left(\vec{r}\right)\right]$ is the exchange-correlation energy per electron. Exchange correlation hole defines a region of reduced probability of encountering a second electron around a given reference electron

$$\rho_{xc}(\vec{r}, \vec{r'}) = \frac{\rho(\vec{r}, \vec{r'})}{\rho(\vec{r})} - \rho(\vec{r'}), \tag{2.24}$$

where $\rho(\vec{r}, \vec{r'})$ is the two electron density matrix. The hole is created by Pauli exclusion principle (exchange hole) and Coulomb repulsion (correlation hole) effects and for integer electron number satisfies the sum rule

$$\int \rho_{xc}(\vec{r}, \vec{r'}) \mathrm{d}\vec{r'} = -1. \tag{2.25}$$

The exchange-correlation energy is therefore the interaction energy between the electron density and the XC hole.
There are numbers of approximations for the exchange correlation energy. The simplest is the local density approximation (LDA) that assumes ϵ_{xc} to be a local function of electron density of a homogeneous electron gas $\epsilon_{xc}^{homo}\left(\rho\left(\vec{r}\right)\right)$. An improvement is obtained by inclusion of a density-gradient via enhancement factor $F_{xc}\left(\rho\left(\vec{r}\right), |\nabla\rho(\vec{r})|\right)$—the generalized gradient approximation (GGA).

2.3 Linear expansion Δ-SCF

The linear expansion Δ-SCF is an approximate technique to calculate excited state energies that uses [49]

- ground state energy functional,
- approximate excited state density.

The excited state density is constructed by adding or subtracting the density of an orbital $|\phi\rangle$ expanded in KS states while conserving the total number of electrons:

$$\rho(r) = \sum_n f_{N\pm1}(\varepsilon_n)|\psi_n(\vec{r})|^2 \mp |\phi(\vec{r})|^2 \tag{2.26}$$

where f is Fermi-Dirac distribution and

$$|\phi\rangle = \sum_n \langle\psi_n|\phi\rangle|\psi_n\rangle \tag{2.27}$$

The Kohn-Sham equations are then solved till self-consistently is achieved.
The difficult part in application of Δ-SCF is choice of the orbital $|\phi\rangle$ that will lead to excited state density. A physical insight into the nature of the excited state is necessary. Knowledge of the symmetry and the nodal structure of the excited state is helpful.

CHAPTER 3

Charge Trapping

The role of a semiconductor photocatalyst is to accelerate a photochemical reaction by transferring photon energy to reactants via photogenerated electron hole pairs in a semiconductor. Understanding the nature of the photogenerated carriers is therefore crucial for understanding of photocatalytic processes.
Most basically, electrons and holes in crystal can be characterized by their degree of charge localization. In a perfect crystal lattice carriers are delocalized—their wave function is a Bloch state. Interaction with various lattice inhomogeneities, as well as coupling to lattice vibrational degrees of freedom, may lead to carrier localization.

The first section of this chapter outlines the mechanisms that lead to a charge localization and discusses factors that determine the spacial extent of the localized state. In particular, the focus is on small polarons—electron(hole)-polarisation field quasiparticles with the size comparable to lattice spacing. Section two provides examples for small-polarons formed due to a strong electron-lattice coupling as well as due to interaction with a defect potential.

3.1 Charge localization

The possibility of electron self-trapping was first predicted by Landau in 1933 [50]. An electron in a polarizable medium “digs” a potential well for itself.

$$V = -\frac{e^2}{\varepsilon_{\text{eff}} r}, \qquad \frac{1}{\varepsilon_{\text{eff}}} = \frac{1}{\varepsilon_\infty} - \frac{1}{\varepsilon_0} \tag{3.1}$$

where ε_∞ and ε_0 are optical and static dielectric constants, respectively. ε_{eff} represents the strength of the dielectric response of the medium (lattice) to a charge perturbation. According to Eq. 3.1 in nonpolar crystals, such as silicon, no polaronic effect is expected $\varepsilon_\infty = \varepsilon_0$, therefore, a quasiparticle composed of the electron and the induced polarisation field was termed a polaron. This simplistic picture holds if the polaronic radius

$$a \sim \frac{\hbar^2 \varepsilon_{\text{eff}}}{e^2 m_{\text{eff}}}, \tag{3.2}$$

is larger than the lattice spacing—a large polaron limit. A polaron radius smaller than lattice spacing (a small polaron) can arise in the presence of short range interactions.

3.1.1 Continuum model

The existence of small and large polaron limits were clearly explained by Emin and Holstein [51]. They analyzed the adiabatic picture of the electron–continuum (electron–lattice) interaction using Hamiltonian of the form:

$$H_e = \hat{T}_e + \int d\vec{r'} Z(\vec{r}, \vec{r'}) \Delta(\vec{r'}), \tag{3.3}$$

where $\hat{T}_e$ is the electron kinetic energy operator; $Z(\vec{r}, \vec{r'})$ is the strength of the interaction between the electron at r' and the continuum deformation $\Delta(\vec{r'})$. The total energy then is a sum of the electronic part

$$E_e = \int d\vec{r} \Psi(\vec{r}) H_e \Psi(\vec{r}) = T_e + V_{\text{int}}, \tag{3.4}$$

and the strain energy of the medium, which in a harmonic approximation takes the form

$$E_s = \frac{1}{2} S \int d\vec{r'} \Delta^2(\vec{r'}). \tag{3.5}$$

The minimum of the total energy is achieved when deformation is

$$\Delta(\vec{r}) = \frac{1}{S} \int d\vec{r'} \Delta^2(\vec{r'}) Z(\vec{r}, \vec{r'}), \tag{3.6}$$

and the strain energy takes the value $E_s = V_{\mathrm{int}}/2$.
Further, Emin and Holstein decomposed the electron–medium interaction into a long and a short range contribution. The long range part arises due to the displacements of positive and negative components of the polar medium. The first nonvanishing term is $Z(\vec{r},\vec{r'}) = E_L|\vec{r}-\vec{r'}|^{-2}$. For the short range part they assumed a delta function $Z(\vec{r},\vec{r'}) = E_S\delta(\vec{r},\vec{r'})$.
By scaling the original electron wave function $\Psi(\vec{r})$ in three dimensions of spacial coordinate

$$R^{-\frac{3}{2}}\Psi\left(\frac{\vec{r}}{R}\right), \tag{3.7}$$

the minimum of the total energy can be expressed as a function of the extension of the electron localization R

$$E(R) = \frac{T_e}{R^2} - \frac{1}{2}\left(\frac{V^{\mathrm{S}}_{int}}{R^3} + \frac{V^{\mathrm{S,L}}_{\mathrm{int}}}{R^2} + \frac{V^{\mathrm{L}}_{\mathrm{int}}}{R}\right), \tag{3.8}$$

where the constants are defined through:

$$T_e = \frac{\hbar^2}{2m}\int d\vec{r}|\nabla\Psi(\vec{r})|^2, \tag{3.9}$$

$$V^{\mathrm{S}}_{\mathrm{int}} = \frac{E_S^2}{S}\int d\vec{r}|\Psi(\vec{r})|^4, \tag{3.10}$$

$$V^{\mathrm{S,L}}_{\mathrm{int}} = \frac{2E_SE_L}{S}\int d\vec{r}\int d\vec{r''}\frac{|\Psi(\vec{r})|^2|\Psi(\vec{r''})|^2}{|\vec{r}-\vec{r'}|^2}, \tag{3.11}$$

$$V^{\mathrm{L}}_{\mathrm{int}} = \frac{E_L^2}{S}\int d\vec{r}\int d\vec{r'}\int d\vec{r''}\frac{|\Psi(\vec{r})|^2|\Psi(\vec{r''})|^2}{|\vec{r}-\vec{r'}|^2|\vec{r}-\vec{r''}|^2}. \tag{3.12}$$

The effects of the relative magnitude of these components on the electron localization are shown in Fig. 3.1.

- Fig. 3.1a—only the long range interaction is present: $V^{\mathrm{S}}_{\mathrm{int}} = V^{\mathrm{S,L}}_{\mathrm{int}} = 0$. The energy is given by $E(R) = T_e/R^2 - V^{\mathrm{L}}_{\mathrm{int}}/2R$ and has a minimum at $R = 4T_e/V^{\mathrm{L}}_{\mathrm{int}}$. This limit corresponds to a large polaron.

- Fig. 3.1b—only the short range interaction is present: $V^{\mathrm{L}}_{\mathrm{int}} = V^{\mathrm{S,L}}_{\mathrm{int}} = 0$. The energy is given by $E(R) = T_e/R^2 - V^{\mathrm{S}}_{\mathrm{int}}/2R^3$ and has two minima at $R \to 0$ and $R \to \infty$. The former corresponds to a small polaron limit, whereas the latter to an unbound electron state. In a discreet lattice the size of the small polaron is finite as the strain energy and the electron-lattice interaction saturate when R is comparable to lattice spacing. Therefore when the size of the small polaron exceeds the barrier at $R = 3V^{\mathrm{S}}_{\mathrm{int}}/4T_e$, it becomes unbound.

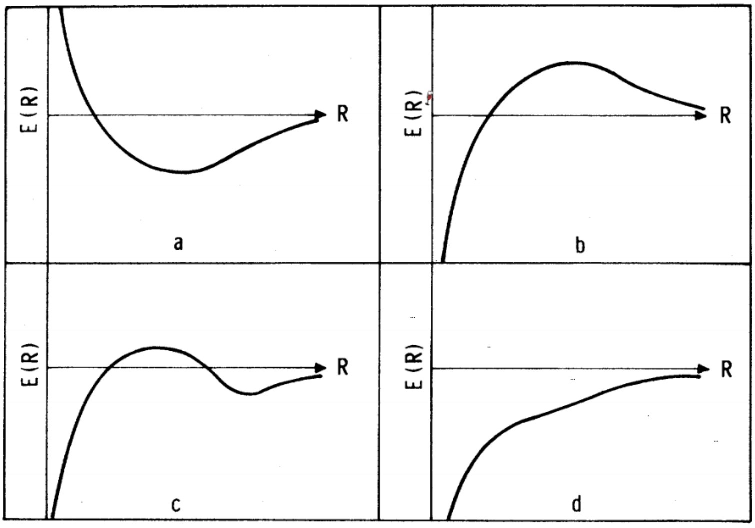

Figure 3.1: Effects of the short and the long range interaction on the spacial extend of the electron wave function: a) only long range interaction is present—large polaron is formed; b) only short range interaction is present—small polaron is formed; c) both interactions are present—the small and the large polarons can coexist; d) both interactions are present—the short range interaction is sufficiently strong and the large polaron collapses into the small polaron state. Figure reproduced from Ref. [51].

- Adding the long range to the short range interaction converts the unbound state at $R \to \infty$ to the bound one (large polaron)—Fig. 3.1c. If the interaction is sufficiently strong the large polaron collapses into the small polaron state—Fig. 3.1d.

3.1.2 Lattice model

To correctly account for the finite size of the small polaron a discreet lattice model is necessary. Shinozuka and Toyozawa considered a simple single band lattice Hamiltonian [52]:

$$H_0 = \sum_{\mathbf{k}} (\varepsilon + t_{\mathbf{k}}) |\mathbf{k}\rangle\langle\mathbf{k}| + \frac{K}{2} Q_0^2, \tag{3.13}$$

where $\varepsilon + t_{\mathbf{k}}$ is the band dispersion and

$$|\mathbf{k}\rangle = \frac{1}{\sqrt{N}} \sum_n e^{i\mathbf{k}\mathbf{R_n}} |n\rangle, \tag{3.14}$$

is the Bloch state formed from lattice orbitals $|n\rangle$.
The charge localization on a single site 0 can be induced by the defect potential $-\Delta$ and/or linear electron-lattice coupling $-DQ_0$:

$$H_1 = -(\Delta + DQ_0)|0\rangle\langle 0|. \tag{3.15}$$

Solution of

$$H = H_0 + H_1 \tag{3.16}$$

for a simple cubic lattice of s-like orbitals leads to two types of the lowest energy states: a free state at the bottom of the band with energy

$$E(Q_0) = \varepsilon - \frac{T}{2} + \frac{K}{2}Q_0^2, \tag{3.17}$$

and a localized state on the lattice site 0 with energy

$$E(Q_0) = \varepsilon - (DQ_0 + \Delta) - \frac{T^2}{24\,(DQ_0 + \Delta)} - \frac{T^4}{1152\,(DQ_0 + \Delta)^3} - \cdots + \frac{K}{2}Q_0^2. \tag{3.18}$$

where T is the band width. The solutions can be characterized by two dimensionless parameters:

- D/T describing the strength of the electron–lattice interaction;
- Δ/T describing the depth of the potential well due to the defect.

Fig. 3.2 shows the potential energy surfaces for different D/T and Δ/T values. Both the electron interaction with the lattice deformation and the defect potential can lead to the formation of a small-polaron. These two origins of trapped electron states are often termed [53] as:

- The intrinsic self-trapping—trapping due to interaction with the lattice ($\Delta = 0$);
- The extrinsic self-trapping—trapping due to interaction with the defect ($D = 0$).

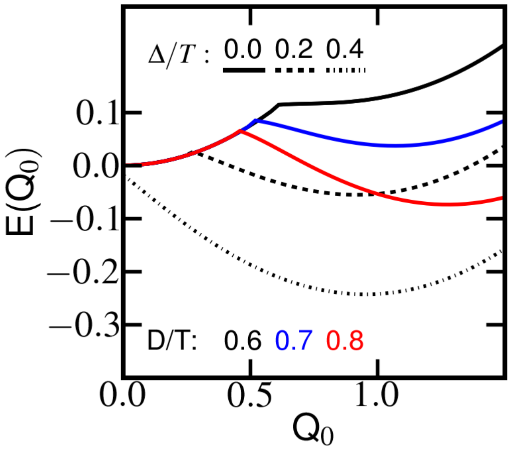

Figure 3.2: Adiabatic potential energy surfaces along lattice distortion Q_0 associated with lattice site 0. The energy is expressed in units of T (the electron band width) and $K = 0.6T$ (see Eq. 3.13). The electron interaction with the lattice distortion D and/or with the defect potential Δ can lead to the formation of the localized bound state.

3.2 Examples

3.2.1 V^- center in MgO

Fig. 3.3 shows nonadiabatic potential energy surfaces for an electronic hole in MgO in the presence of a Mg vacancy. At zero distortion the hole is localized on the six oxygen lattice sites surrounding the defect (the E_g state) and hence, the origin of the self-trapped state is only due to the defect potential. Interaction with the lattice distortion, however, leads to the hole localization on a single oxygen lattice site (the A_1^1 state). For details see paper III.

3.2.2 TiO_2 Bulk

Rutile and anatase TiO_2 are examples where an electronic hole self-traps intrinsically, i.e. only due to interaction with the lattice. The top plot in Fig. 3.4 shows adiabatic potential energy surfaces along the lattice coordinate inducing the hole localization. At zero distortion, the hole is delocalized over oxygen $p_\perp$

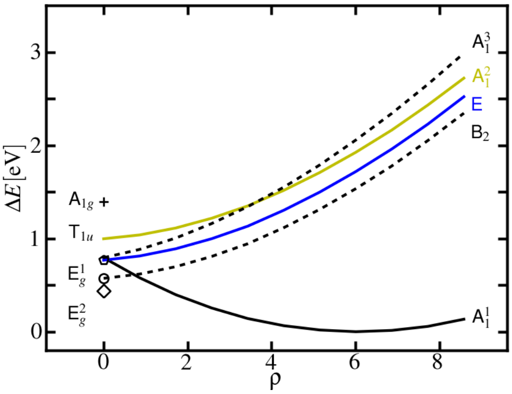

Figure 3.3: The nonadiabatic potential energy surfaces (PESs) for different symmetry states of the V^- center along the $O_h(\rho = 0) \to C_{4v}$ distortion.

orbitals forming the top of the valence band. At larger distortions the hole localizes on a single lattice site. The bottom plot in Fig. 3.4 shows the hole state projection onto $p_\perp$ orbital of the oxygen lattice site. For details see paper I.

3.2.3 TiO$_2$ Surface

In surface layers the self-trapping strength is modified due to a potential variation induced by the crystal termination. Fig. 3.5 illustrates self-trapping strength and the electrostatic energy depth profile for the anatase (101) facet. Clearly, surface potential can significantly modify trapping strength and give rise to self-trapped states even if the electron-lattice interaction alone is insufficient for the formation of trapped states. For details see paper II.

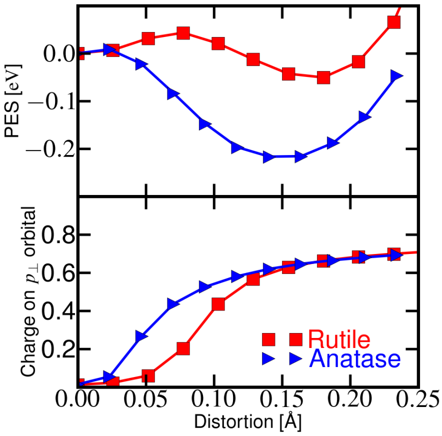

Figure 3.4: Hole self-trapping in TiO_2. Top: adiabatic potential energy surfaces; bottom: charge localization on the oxygen $p_\perp$ orbital of the oxygen lattice site surrounded by the distortion.

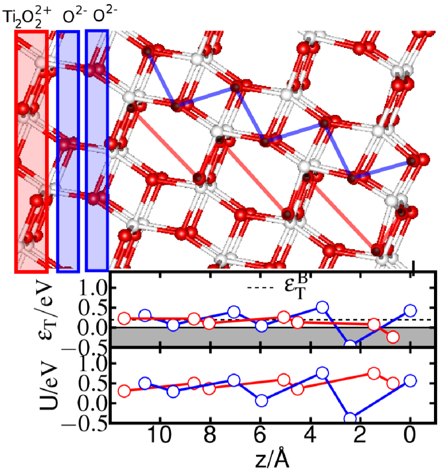

Figure 3.5: Hole trapping in anatase (101) surface layers. Trapping strength ε_T is modified due to the variation of the surface electrostatic potential. U is the interaction energy of the hole with the surface electrostatic potential.

Chapter 4

Total Energy Nonlinearity in DFT

Accurate description of charge localization/delocalization processes is one of the biggest challenges of DFT approximations [54–63]. In particular application of DFT to small polaron problem often leads to qualitatively incorrect results [36–40]. This failure is largely a consequence of an incorrect, nonlinear behaviour of total energies in fractional electron number segments [64–71].

This chapter begins with a brief discussion of the origin of the total energy nonlinearity and demonstrate how the nonlinearity can lead to large systematic errors in description of states with different degrees of localization. Sections two and three examines the consequences of the error for the description of small polarons and provide a simple, ad hoc, solution with a few illustrative examples. Finally, the last section lists some of the methods that attempt to improve approximate DFT energies for fractional electron systems.

4.1 Origin and effects

The exact DFT energy is linear in fractional electron number segments [46, 72], see also Sec. 2.1.1. Approximate XC functionals violate this exact behaviour and provide nonlinear total energies due to incorrect description of exchange-correlation hole $\rho_{xc}(\vec{r},\vec{r'})$ for systems with fractional electron number [73, 74]. For instance (semi)local XC functionals provide convex curves—total energies are too low between integer electron numbers (see Fig. 4.1). This energy underestimation has been explained as a result of an incorrect sum rule for the exchange-correlation hole. The exchange-correlation hole for (semi)local XC functionals integrates to -1 which is a correct value only for an integer electron number (see Sec. 2.2.1). For open systems with fractional electron number, the exact exchange hole should integrate to a value smaller than -1. Therefore the semi-local exchange correlation energy

$$E_{xc}\left[\rho\left(\vec{r}\right)\right] = \frac{1}{2}\int \rho(\vec{r})\frac{\rho_{xc}(\vec{r},\vec{r'})}{|\vec{r}-\vec{r'}|}\mathrm{d}\vec{r}\mathrm{d}\vec{r'}, \tag{4.1}$$

is too negative at fractional electron number leading to convex total energy curves.

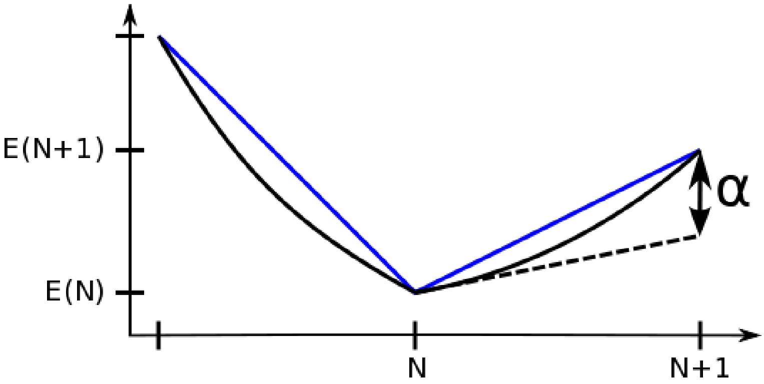

Figure 4.1: A total energy as a function of electron number. The exact energy (blue line) is linear in integer electron number segments. Semi-local XC functionals provide convex total energy curves (black line). Dashed line denotes a tangent to the semi-local total energy curve at N_+ and α is the energy nonlinearity.

The nonlinearity of the total energy leads to systematic errors which depend on the degree of charge localization. To illustrate this let us consider a single atom with energy

$$E(N+\lambda) = \alpha\lambda^2 + \left[E(N) - E(N+1) - \alpha\right]\lambda + E(N), \tag{4.2}$$

in $[N, N+1]$ electron number segment; $E(N)$ and $E(N+1)$ are correct energies at N and $N+1$ electron numbers, respectively; and α is a quadratic energy nonlinearity (see Fig 4.1). Adding a single electron to a system composed of K noninteracting N electron atoms should increase the energy by $E(N+1)-E(N)$. For $\alpha \neq 0$ however, the total energy increase is

$$\Delta E = \alpha\left[\frac{1}{M} - 1\right] + E(N+1) - E(N), \tag{4.3}$$

where the additional electron delocalizes over M atoms. Solutions for $M \in \{1, \ldots, K\}$ should be degenerated, however, for $\alpha < 0$ (convex functionals) the delocalized solution $M = K$ has the lowest energy, whereas for $\alpha > 0$ (concave functionals) the localized solution $M = 1$ is the most stable.

M dependent part of the energy change is quadratic in fractional electron number λ:

$$\Delta E(\lambda) = \left\{\alpha\left[\frac{\lambda}{M} - 1\right] + E(N+1) - E(N)\right\}\lambda. \tag{4.4}$$

Thus α/M can be calculated as the quadratic nonlinearity of $\Delta E(\lambda)$. Removal of α/M from Eq. 4.3 renders the equation M independent. Such correction then allows for an unbiased comparison of energies of states with a different degree of localization.

4.2 Nonlinearity removal

Quadratic nonlinearities of total energies of noninteracting atoms translate into linear dependencies of onsite energies in a single band model presented in Sec. 3.1.2. A nonzero α will shift the eigenvalues of the lattice Hamiltonian (see Eq. 3.16) by the value dependent on the degree of localization of the eigenstate

$$\frac{\alpha}{M} = \frac{\alpha\sum_n |\langle n|\Psi\rangle|^4}{\left[\sum_n |\langle n|\Psi\rangle|^2\right]^2}, \tag{4.5}$$

where $|\langle n|\Psi\rangle|^2$ is the occupation of site n in solution $|\Psi\rangle$. For a free state ($|\Psi\rangle = |\mathbf{k}\rangle$) $M \to \infty$; for a localized state ($|\Psi\rangle = |0\rangle$) $M = 1$. Therefore the comparison of energies of the two states is burden with error α. By removing the total energy nonlinearity α/M, a more consistent description of the charge localization can be achieved.

Such an a posteriori correction obviously does not affect the eigenstates $|\Psi\rangle$. A nonzero α will have the strongest effect on the localized wave function. In zeroth order the localized state on site 0 can expressed as

$$|0\rangle' = |0\rangle + \sum_n \frac{t_{n0}}{\Delta + DQ_0 - \alpha}|n\rangle \tag{4.6}$$

where t_{n0} is the coupling between site 0 and n; and $\Delta + DQ_0 > 0$ is the trapping energy at site 0. Positive and negative α will therefore provide too delocalized and localized solutions, respectively.

4.3 Examples

4.3.1 Polaronic defect states

Defects states of a magnesium vacancy in MgO provide a clear illustration of $1/M$ dependence of the localization/delocalization error. The defect states are largely formed from six oxygen p-like orbitals $|\gamma_i\rangle$ pointing toward the vacancy. At the O_h symmetry (the symmetry of the Mg lattice site in the perfect MgO crystal) the defect states are

$$\begin{aligned}
A_{1g} &= (|\gamma_0\rangle + |\gamma_1\rangle + |\gamma_2\rangle + |\gamma_3\rangle + |\gamma_4\rangle + |\gamma_5\rangle)/\sqrt{6} \\
T^1_{1u} &= (|\gamma_0\rangle - |\gamma_5\rangle)/\sqrt{2} \qquad T^2_{1u} = (|\gamma_1\rangle - |\gamma_3\rangle)/\sqrt{2} \\
T^3_{1u} &= (|\gamma_2\rangle - |\gamma_4\rangle)/\sqrt{2} \\
E^1_g &= (|\gamma_1\rangle - |\gamma_2\rangle + |\gamma_3\rangle - |\gamma_4\rangle)/\sqrt{4} \\
E^2_g &= (2|\gamma_0\rangle - |\gamma_1\rangle - |\gamma_2\rangle - |\gamma_3\rangle - |\gamma_4\rangle + 2|\gamma_5\rangle)/\sqrt{12}
\end{aligned}$$

whereas at the C_{4v} symmetry (the symmetry of the relaxed V^- center) these are

$$\begin{aligned}
A^1_1 &= |\gamma_0\rangle \qquad A^2_1 = (|\gamma_1\rangle + |\gamma_2\rangle + |\gamma_3\rangle + |\gamma_4\rangle)/\sqrt{4} \\
A^3_1 &= |\gamma_5\rangle \qquad B_2 = (|\gamma_1\rangle - |\gamma_2\rangle + |\gamma_3\rangle - |\gamma_4\rangle)/\sqrt{4} \\
E^1 &= (|\gamma_1\rangle - |\gamma_3\rangle)/\sqrt{2} \qquad E^2 = (|\gamma_2\rangle - |\gamma_4\rangle)/\sqrt{2}
\end{aligned}$$

The degree of localization of these states equals to $f = 1/M \in \{1, 1/2, 1/4, 1/6\}$. For instance $f = 1/6$ for the A_{1g} state as this state is delocalized over six sites. Fig. 4.2 shows the total energy nonlinearities for the different states. Clearly, the nonlinearities follow $1/M$ behaviour.
Fig. 4.3 shows potential energy surfaces of defect states calculated with the PBE XC functional (top panel); and results corrected for the energy nonlinearity (the bottom panel). The two predictions provide qualitatively different behaviours. The PBE calculated states are not only shifted but also incorrectly ordered. For details see paper III.

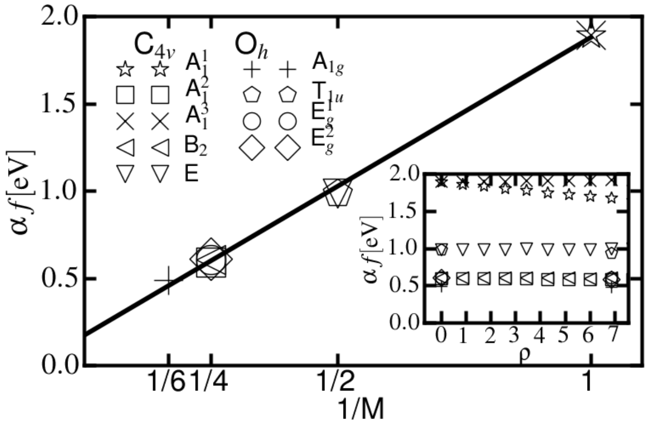

Figure 4.2: The energy nonlinearity αf follows $f = 1/M$ trend; f is the degree of state localization, e.g. $f = 1/2$ for the T_{1u} as this state is localized over two sites. The inset plot shows the energy nonlinearity along the $O_h(\rho = 0) \to C_{4v}$ distortion.

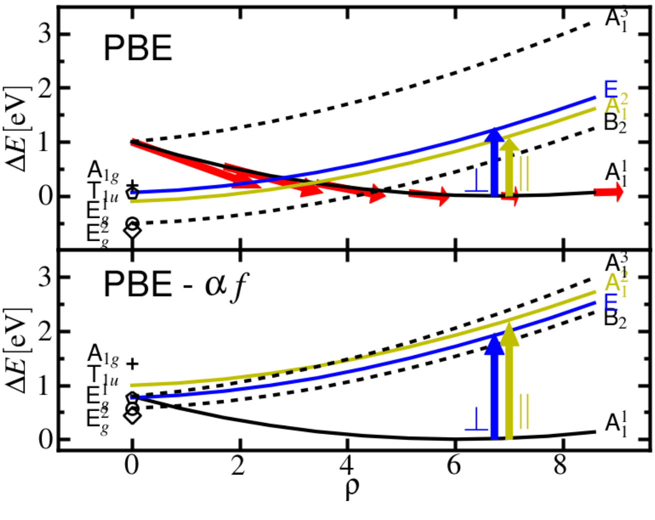

Figure 4.3: The nonadiabatic potential energy surfaces (PESs) for the different symmetry states of the V^- center along the $O_h(\rho = 0) \to C_{4v}$ distortion. Top: PBE PESs not corrected for the delocalization error; Bottom: PESs corrected by removal of the energy nonlinearity αf. Full lines denote states involved in optical transitions of the center; arrows tangent to the A_1^1 are proportional to sum over Hellman-Feynman forces.

4.3.2 Barrier hight

Another example where the incorrect description of total energies leads to qualitatively incorrect behaviours is a charge transfer process. Let us consider an electron transfer between two centers L and R

$$\begin{array}{ccc} \text{Ininial} & \text{Transition} & \text{Final} \\ L^1 + R \rightarrow & L^{1/2} + R^{1/2} \rightarrow & L + R^1 \end{array} \tag{4.7}$$

$$\tag{4.8}$$

For the initial and final states $M = 1$, whereas at the transition state $M = 2$. Therefore if α is the nonlinearity of the total energy at a single site R and L, the energy at the transition point is depleted by $\alpha/2$.
Fig. 4.4 shows PESs for a charge transfer between two equivalent sites. A nonzero α leads to characteristic kink around the transition state. For details see paper II.

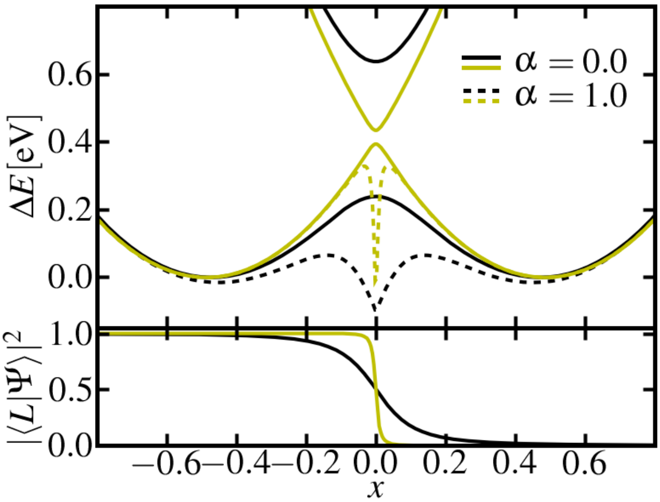

Figure 4.4: Top: the PESs for the two state model for a charge transfer between two equivalent sites coupled to the lattice coordinate x (full lines) and the deformed PESs due to δN convexity of the energy of single site (dashed lines). Bottom: the charge localization on L site.

4.3.3 Self trapping

Charge self-trapping in extended systems is the process where the localization/delocalization error reaches its maximum. For the delocalized state $M \rightarrow \infty$, whereas for the localized one $M = 1$. Paper I, analysis an electronic hole self-trapping in TiO_2. The semi-local RPBE XC functional [75] predicts localized hole state to be unstable. Removal of the total energy nonlinearity leads to a stable self-trapped state (see Fig. 3.4).

4.4 Other approaches

- Range separated hybrid schemes such as HSE XC functional [67, 76]
  These functionals incorporate a portion of the exact exchange from the Hartree-Fock theory. The improvement of the description of fractional electron systems relies on the cancellation of the δN convexity of a (semi)local DFT by the δN concave Hartree-Fock energy. So far, none of the mixing schemes have been able to recover the δN linearity universally.

- Scaling Correction [77]
  This is an interesting recent development based on an observation that the only terms that are nonlinear in the electron density are Coulomb, exchange and correlation terms. By linearizing Coulomb and exchange terms with respect to fractional electron number so that the correction is zero at integer electron numbers largely linear the total energy curves are obtained. More studies are however necessary to reveal to which extent the method can be applied to more general problems such as the discussed defect states of the V^- center in MgO.

- Non-Koopmans correction [78]
  This technique imposes the Koopmans condition, i.e. linearity of the total energy with respect to the change of the occupations of the Kohn-Sham states, by fixing eigenvalues around a chosen reference point. The method needs to be tested for its ability to deal with charge localization and delocalization processes. Since the error of the eigenvalues changes with their degree of localization, the choice of the reference points is nontrivial.

- DFT+U based techniques [79]
  In a rotationally invariant formulation [80], the total DFT+U energy is

$$E^{\mathrm{DFT}+U} = E^{\mathrm{DFT}} + \frac{U}{2} \sum_{a,\sigma} \mathrm{Tr}\, \left[\mathbf{n}_a^\sigma \left(1 - \mathbf{n}_a^\sigma \right) \right], \qquad (4.9)$$

where $\mathbf{n}_a^\sigma$ is the atomic density matrix due to the atom a and the spin σ and where U is a parameter. The correction is quadratic in atomic density matrix, therefore, in principle, it can account for the spurious quadratic energy nonlinearity [81]. Since there is a certain degree of arbitrariness in definition of atomic density matrices, and they do not necessarily follow linearly the change in electron number a single U may not suffice for a complete removal of energy nonlinearities.

  - Non-local external potential [39]
    This DFT+U like method has been specifically formulated for the problem of polaronic hole localization. Since different U values are required for a correct description of a host band structure and a localized hole state, a nonlocal potential is constructed so that it affects the localized hole state only.
  - DFT+U+V [82, 83]
    DFT+U is extended by introduction of an inter-site parameter V. Both U and V are calculated internally based on linear response.

- Perdew-Zunger self-interaction correction [84, 85]
  The method improves the description of the exchange-correlation hole by removing the orbital electron self-interaction. This correction however, only partially removes the total energy nonlinearity and worsens equilibrium properties [86].

Chapter 5

Small Polaron Optical Absorption

Time resolved optical spectroscopies are the most commonly used techniques to monitor the dynamics of the photo generated charge carriers. To exploit the full wealth of information these techniques provide, one first has to understand the physical origins of the optical absorption bands.

In this Chapter DFT is applied to small polaron optical absorption. The first section analyzes the origin of small polaron optical transitions. Section two provides absorption coefficient for vibrionic transitions and briefly discusses assumed approximations. In the last section, DFT is applied to optical absorption of the V^- center in MgO and to the bulk and surface self-trapped holes in TiO_2.

5.1 Interpolaron transitions

Small polarons have strong absorption features due to optical charge transfer transitions i.e., promotions of the electron (hole) trapped on one site to one of the neighboring sites (interpolaron transitions) [87–90]. This concept is illustrated in Fig. 5.1. A carrier localized on site L is promoted to site R. The transition

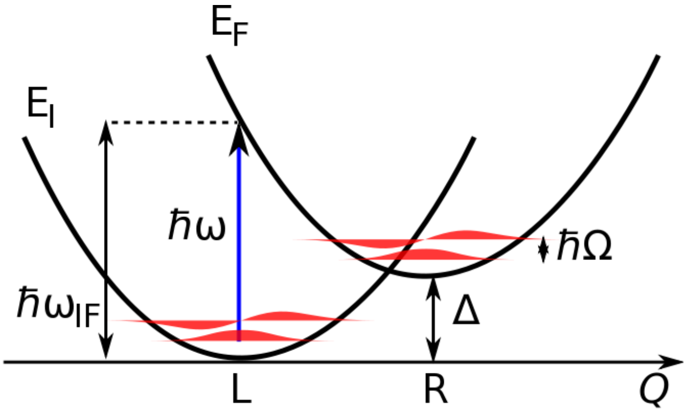

Figure 5.1: Promotion of a small polaron localized on site I to a neighboring site F (inter-polaron transition). The transition is vibronic as it involves simultaneous change of the electron state and nuclear quantum numbers.

involves simultaneous change of electronic state and nuclear quantum number—has a vibronic character.

5.2 Absorption coefficient

The optical absorption coefficient $k(\omega)$ is defined through Beer-Lambert law:

$$I(\omega, z) = I(\omega, 0) \exp -k(\omega)z, \tag{5.1}$$

where the light of initial intensity $I(\omega, 0)$ is attenuated along the direction of the propagation z and ω is the light angular frequency. When the absorption occurs due to distinct centers such as defects, it is convenient to define absorption cross-section per center:

$$\sigma(\omega) = k(\omega)/N, \tag{5.2}$$

where N is the number of centers. Absorption cross-section can be derived from quantum mechanical description of transition probability between two states induced by coupling to the radiation. The transition rate is

$$W = \frac{2\pi}{\hbar^2}|\langle i|\mathbf{V}|f\rangle|^2\delta(\omega - \omega_{if}), \tag{5.3}$$

where $\mathbf{V}$ is the coupling operator; and i, f are the initial and the final states, respectively.

5.2.1 Vibronic Transitions

In the derivation of the absorption cross-section for the vibronic transitions usually three approximations are employed [91, 92]:

1. Born-Oppenheimer approximation breaks the wave-function into the product of an electronic and a nuclear part:
$$i(\mathbf{r}, \mathbf{Q}) = I(\mathbf{r}; \mathbf{Q})\chi(\mathbf{Q}), \tag{5.4}$$
where the electronic part $I(\mathbf{r}; \mathbf{Q})$ depends parametrically on the nuclear coordinate $\mathbf{Q}$.
2. Condon approximation: $\langle I|\mathbf{V}|F\rangle$ is independent on $\mathbf{Q}$.
3. Dipolar approximation: only electric dipole moment transitions are involved.

The application of the above approximations leads to the absorption cross-section:[1]
$$\sigma(\omega) = \frac{2\pi^2 e^2 \hbar}{m} f_{IF} G_{IF}(\omega), \tag{5.5}$$
where G_{IF} is the shape function and f_{IF} is the oscillator strength. The shape function takes the form:
$$G_{IF}(\omega) = \mathrm{Av}_\alpha \sum_\beta |\langle\alpha|\beta\rangle|^2 \delta(\omega_{IF} + \omega_{\alpha\beta} - \omega), \tag{5.6}$$
where Av_α denotes thermal average over initial states and the sum runs over final states. $G_{IF}(\omega)$ is normalized to unity over ω.
The oscillator strength is a dimensionless quantity:
$$\vec{f}_{IF} = \frac{2m_e\omega_{IF}}{e^2\hbar}\vec{\mu}^2_{IF}, \tag{5.7}$$
where $\vec{\mu}_{IF}$ is the electronic transition dipole moment. f_{IF} expresses the strength of the transition and satisfies the sum rule $\sum_F f_{IF} = 1$.

5.2.2 Transition Dipole Moment

The transition dipole moment between the initial $|I\rangle$ and final $|F\rangle$ states equals
$$\vec{\mu}_{IF} = \langle I| - e\vec{r}|F\rangle. \tag{5.8}$$

---

[1] For the effective field and the difference in the velocity of light propagation in a material medium corrections see [93].

If the states $|I\rangle$ and $|F\rangle$ are associated with transnationally equivalent sites R and L, respectively, their first order expansions take the forms:

$$|I\rangle = |L\rangle + \frac{t}{\hbar\omega_{IF}}|R\rangle, \tag{5.9}$$

$$|F\rangle = |R\rangle - \frac{t}{\hbar\omega_{IF}}|L\rangle, \tag{5.10}$$

where $|R\rangle$ and $|L\rangle$ are orthonormal wave-functions associated with noninteracting sites R and L, respectively; t is the electron coupling between the two sites; and $\hbar\omega_{IF}$ is the transition energy (see Fig.5.1). Inserting Eq.5.9 and Eq.5.10 to Eq.5.8 and using translational equivalence between sites R and L:

$$R(\vec{r}) = L(\vec{r} + \vec{p}), \tag{5.11}$$

where $\vec{p}$ is the vector connecting the two sites, $\vec{\mu}_{IF}$ takes the final form [94]:

$$\vec{\mu}_{IF} = \frac{te}{\hbar\omega_{RL}}\vec{p}. \tag{5.12}$$

5.3 Examples

5.3.1 V^- MgO

The top part of Fig. 5.2 shows the experimental and calculated absorption spectra of the V^- center in MgO. The optical absorption spectrum consists of a broad peak centered at ≈ 2.3 eV and the low energy part involves hole transfer transitions between oxygen p-like orbitals pointing toward the vacancy[2] [94, 95]. In an electric field, the V^- centers align and absorption of light polarized parallel ($\|$) to the direction of the applied electric field has a peak at 1.85eV ($A_1^1 \rightarrow A_1^2$); whereas the absorption peak for the light polarized perpendicularly ($\perp$) is located at 2.30eV ($A_1^1 \rightarrow E$) [90, 94, 95]. The bottom part of Fig. 5.2 shows $\sigma_{\|} - \sigma_{\perp}$. For defect states and associated PES see Sec.4.3.1 or paper III.

5.3.2 Self-trapped hole in TiO$_2$

The shaded bands in Fig. 5.3 show the calculated optical absorption of the self-trapped holes in anatase. The band X is due to the holes trapped in the

---

[2] The high energy part involves also transition for other p orbitals surrounding the vacancy.

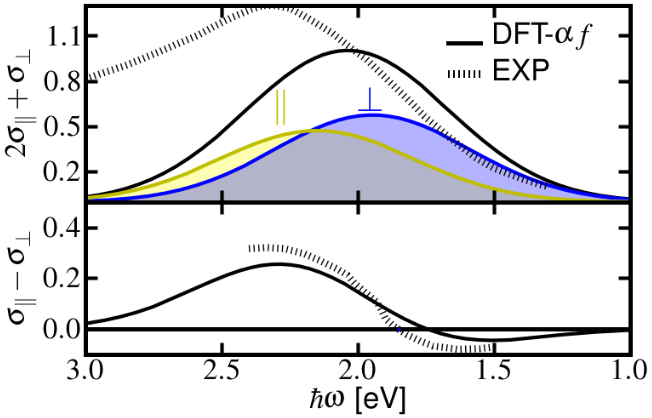

Figure 5.2: Top: the optical absorption spectra of the V^- center. Bottom: the dichroism curve. Dotted and full lines denote the experimental data [95] and calculated bands, respectively. Shaded areas denote transitions due to the perpendicular ($\perp$) and parallel ($\parallel$) light polarization.

bulk, whereas bands $Y1$, $Y2$, $Y3$, Z are due to the most stable (sub)surface hole trapping sites, see Fig. 5.4 for the locations. Transition energies form the surface trapped holes are at higher energies than form the bulk trapped holes. This is largely because in surface layers trapping strength oscillates (see section 3.2.3) and an additional energy is needed to optically transfer hole to neighboring trapping sites (Δ on Fig. 5.1). For details see paper V.

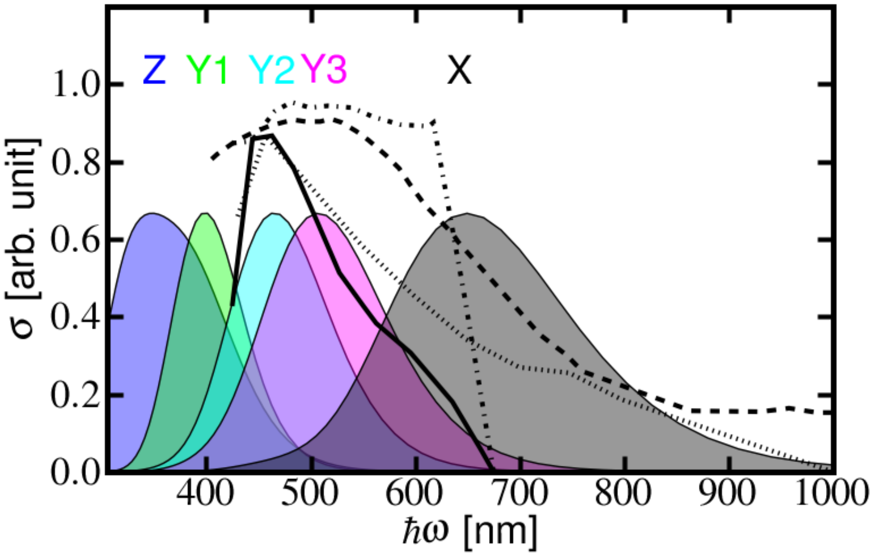

Figure 5.3: The optical absorption spectra of the self-trapped holes in anatase TiO_2. The absorption energy increases with the increase in stability of the hole state relative to its neighbours. Bands: X—bulk holes; $Y1$, $Y2$, $Y3$—holes in (101) surface layers; Z—hole on (001) surface. Lines denote experimental measurements: full line[23]; dashed line [96]; dash-dotted line [96]; dotted line [28].

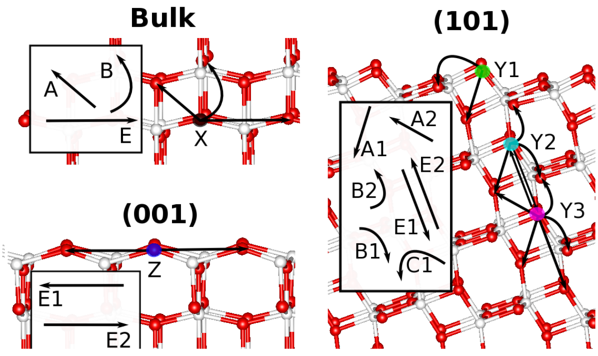

Figure 5.4: Location of trapping centers $X, Y1, Y2, Y3, Z$. Arrows indicate the strongest transitions. Letters $A - E$ denote distinct charge transfer paths in the anatase bulk, and accompanied numbers denote nonequivalence of paths in surface layers.

CHAPTER 6

Small Polaron Mobility

Delivery of photogenerated carriers to surface reactive sites is a crucial step in any photocatalytic process. Transport of electrons and holes should not be a limitation for reaction kinetics.

This Chapter first introduces the concept of electron mobility. The next two sections describe the two possible charge transport mechanisms in semiconductors: 1) band conduction and 2) small polaron hopping. Finally, the last section discusses hole transport in TiO_2.

6.1 Electron Mobility

A phenomenological description of electron conductivity is expressed in Ohm's law: the current density $\vec{j}$ at a given location in a conductor is proportional to the applied electric filed $\vec{E}$ at that location

$$\vec{j} = \boldsymbol{\sigma}\vec{E}, \tag{6.1}$$

where the electronic conductivity $\boldsymbol{\sigma}$ is material dependent second rank tensor. For the sake of simplicity, in the following, I consider isotropic conductivity i.e. σ to be a scalar quantity and $\vec{j} \parallel \vec{E}$.

The accelerating force $-eE$ acting on charge carriers in a material is counterbalanced by scattering processes, therefore σ has a finite value. Defining τ as the mean electron time, the electron conductivity can be expressed as

$$\sigma = \frac{ne\tau}{m^*} = n\mu, \tag{6.2}$$

where n is the carrier density and m^* is the electron effective mass. The electron mobility μ characterises motion of a single electron in a material i.e., is the drifted velocity v_d in a unit electric filed E:

$$\mu = \frac{v_d}{E}. \tag{6.3}$$

6.2 Band Transport

This section provides a basic introduction to the band transport mechanism. Electrons in a crystal occupy Bloch states labeled by crystal momentum quantum number k. The electric conductivity is therefore a sum over all contributions arising from occupied k states. Using definition in Eq. 6.1, σ takes the form

$$\sigma = \frac{j}{E} = \frac{e}{EV}\sum_k v(k)F(k), \tag{6.4}$$

where V is the crystal volume, $F(k)$ is the Fermi-Dirac distribution in the applied electric field E and

$$v = \frac{1}{\hbar}\frac{d\varepsilon(k)}{dk} \tag{6.5}$$

is the group velocity of the electron particle-wave in energy band $\varepsilon(k)$.
In electric field E, the electron acceleration increases crystal momentum $\hbar k$:

$$\hbar\frac{dk}{dt} = -eE. \tag{6.6}$$

Due to scattering processes however, the shift of the Fermi distribution $F(k) \approx f(k + \Delta k)$ saturates at some finite Δk:

$$\Delta k \approx -\frac{eE\tau}{\hbar}, \tag{6.7}$$

where τ is the mean free electron time and $f(k)$ is the Fermi-Dirac distribution at zero field. Expanding the Fermi-Dirac distribution in the first order in Δk

$$f(k + \Delta k) = f(k) + \frac{df(k)}{dk}\Delta k, \tag{6.8}$$

and performing simple arithmetic manipulations, the electron conductivity is found to be

$$\sigma = \frac{e\tau}{V} \sum_k \left[\frac{d^2\varepsilon}{\hbar^2 dk^2} \right] f(k). \tag{6.9}$$

Defining the effective mass m^* as

$$m^* = \left[\frac{d^2\varepsilon}{\hbar^2 dk^2} \right]^{-1} \tag{6.10}$$

and carrier density n as

$$n = \frac{1}{V} \sum_k f(k) \tag{6.11}$$

we arrive to Eq. 6.2. In general, the effective mass is a second rank tensor therefore the conductivity is an anisotropic quantity.

6.2.1 Mobilities in Semiconductors

In semiconductors there are no states at the Fermi level and charge transport can only be realized via thermally or optically excited carriers—the electrons in the conduction band and holes in the valence band.

$$\sigma = n_h \mu_h + n_e \mu_e \tag{6.12}$$

In most semiconductors, the Fermi level is well separated from the conduction and valence band edges. Thus, the Fermi-Dirac distribution approximates to Boltzmann distribution and when carriers are thermalized, their mean speed is the thermal velocity

$$< v >= \sqrt{\frac{8k_bT}{3\pi m_e}}. \tag{6.13}$$

Typical band mobilities in semiconductors are 10–10^4 cm^2 V^{-1}s^{-1} at room temperatures. For instance for conduction band electrons in Si $\mu_e = 1500$ cm^2 V^{-1}s^{-1}. Using Eq.6.2, the thermal velocity at room temperature $< v >= 10^7$ cm/s, and the effective mass of electrons in Si conduction band $m_e^* = 1.18 m_e$, we find the mean free electron time $\tau = 10^{-12}$ s and the mean free electron path of the electron of 10^3 Å.

6.3 Hopping Transport

In number of materials mobilities are smaller that 1 cm^2 V^{-1}s^{-1}. Such low values would require unphysically short mean free electron paths of ~ 0.1 Å.

Furthermore the electron mobility in these materials increases with temperature which is in contrast to band transport mechanism where the mobility decreases with temperature.

The mechanism explaining above observations is thermally activated hopping. Taking a hop distance of $a \sim 3$ Å (a typical atomic spacing in crystals) and hopping frequency $k \sim 10^{12} - 10^{13}\ \mathrm{s}^{-1}$ (a typical value for phonon frequencies), one can estimate the hopping mobility at room temperature to be

$$\mu = \frac{ea^2k}{k_BT} \sim 0.1\,\mathrm{cm}^2\ \mathrm{V}^{-1}\mathrm{s}^{-1}. \tag{6.14}$$

The hopping mechanism holds if the time between hops k^{-1} is smaller than the residence time of an electron on transitionally equivalent lattice sites $\tau \approx t/h$, where t is the resonance integral related to the electron band width. Typically t is of the order of 1 eV therefore $\tau \approx 4 \times 10^{-15}\mathrm{s} \ll k^{-1}$.

Hopping transport becomes relevant under strong electron-phonon coupling when t renormalizes exponentially

$$t' = t\exp(-S_T). \tag{6.15}$$

The factor S_T is proportional to $\coth[\hbar\Omega/(2k_BT)]$ and the proportionality constant is related to the strength of the electron coupling to the phonon mode of angular frequency Ω [97–99]. Thus for strong electron-phonon coupling the resonance integral t' becomes exponentially small at temperature:

$$T_h \gg \frac{\hbar\Omega}{2k_B}. \tag{6.16}$$

6.3.0.1 Hopping mobility

At the small polaron limit i.e., when the electron is confined to a single lattice site, the hopping is limited to the neighboring sites [97–99]. Depending on the relative dynamics of the electron and the lattice, two limiting situations can be distinguished:

- The adiabatic limit—the electronic motion is much faster than the nuclear and the system remains on a single PES. The charge transfer proceeds via thermally activated barrier crossing.
- The nonadiabatic limit—the electron does not follow the fast nuclear dynamics and transitions occurs via tunneling at the cross-section of two nonadiabatic potential energy surfaces.

For the two limits, the hopping frequency takes the form:

$$k = \frac{\Omega}{2\pi} e^{-\frac{E_b}{k_B T}} \times \begin{cases} 1 & \text{for } \eta_2 > 1, \text{ adiabatic limit} \\ \pi^{3/2}\eta_2 & \text{for } \eta_2 \ll 1, \text{ nonadiabatic limit} \end{cases} \tag{6.17}$$

Where

$$\eta_2 = \frac{t^2}{\hbar\Omega\sqrt{E_a k_B T}} \tag{6.18}$$

describes relative dynamics of the electron and the lattice systems [97–99].

6.4 Example

Fig. 6.1 shows PES for the different hole transfer paths between neighboring oxygen lattice sites in TiO_2. The single effective atomic nuclear coordinate is defined as a linear interpolation between the final and the initial geometries for the hole transfer. The effective mode energies along the coordinate are ≈ 0.04 and ≈ 0.02 eV for rutile and anatase, respectively. Therefore according to Eq. 6.16 hopping is a relevant mechanism at temperatures above ~230 and ~120 K for rutile and anatase, respectively.

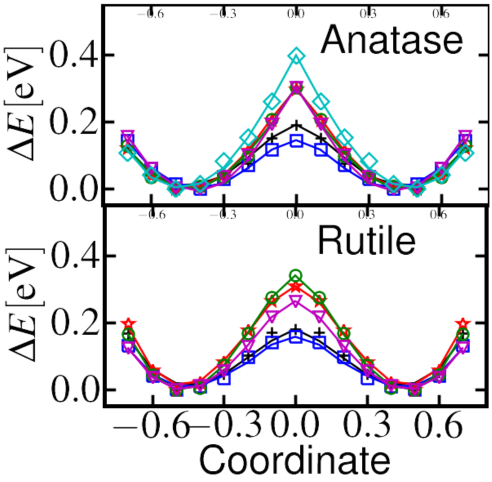

Figure 6.1: Potential energy surfaces for hole transfer paths between neighboring oxygen lattice sites in TiO_2.

Using Einstein-Smoluchowski relation between the mobility μ and the diffusion coefficient D:

$$\mu = \frac{eD}{k_B T} \tag{6.19}$$

and Eq. 6.17 and 6.18, the averaged hopping mobility takes the form

$$D = \sum_{i \in \mathrm{A}\ldots} n_i k_i |\mathbf{R_i}|^2/3, \tag{6.20}$$

where n_i is a number of equivalent paths, k_i is the transfer frequency, $|\mathbf{R_i}|$ is the transfer distance, and the summation is over nonequivalent hole transfer paths. For details see paper II.

CHAPTER 7

TiO_2 photocatalyst

Photogenerated charge carriers (electrons and holes) play a central role in any photocatalytic process [6, 100]. In TiO_2 the holes trap, but the nature of trapping sites as well as effects of trapping on photocatalytic performance are unclear.

This chapter first summarises the properties of TiO_2 that are relevant to the photocatalytic processes. The second section discusses possible effects of charge trapping on a photocatalyst performance. Finally, the third section discusses hole trapping in TiO_2.

7.1 Properties of TiO_2

7.1.1 Structural

The two main polymorphs of TiO_2 are rutile (D_{4h}^{14}-$P4_2/mnm$, $a = 4.584$ Å, $c = 2.953$ Å) and anatase (D_{4h}^{19}-$I4_1/amd$, $a = 3.782$ Å, $c = 9.502$ Å)[101, 102]. Both crystal forms are tetragonal and their basic building block is a deformed TiO_6 octahedron (see Fig. 7.1) and the deformation is larger in anatase. A characteristic feature of both structures is a planar first coordination shell of oxygen sites—a C_{2v} symmetric OTi_3 unit. Such coordination is achieved by sharing each vertex of the TiO_6 octahedron with two other octahedra: in rutile through one edge- and one corner-type connection (see Fig. 7.1(a)); in anatase through two edges (see Fig. 7.1(b)).

Bulk rutile is the stable phase of TiO_2 under pressures below ~ 10GPa [103–105]. Anatase becomes stable for nano-particle sizes smaller than ~ 14 Å [106] due to lower surface energies as well as smaller destabilization effects of corners and edges [107].

Tab. 7.1 shows surface energies of rutile and anatase facets in vacuum. For rutile the most stable is the (110) surface whereas for anatase it is the (101) surface. In a nonvacuum environment surface stability changes. For instance, for anatase in solutions containing F^- anions the (001) surface becomes more stable than the (101) [108–111].

Table 7.1: Surface energies of TiO_2 facases in J/m^2.

	Calculated[a]	Reference
	Rutile	
(110)	not converged	0.48[b], 0.31[d], 0.69[d], 0.47[f]
(100)	0.66	0.67[b], 0.60[f]
(011)	1.11	1.01[b], 1.12[d], 0.95[f]
(001)	not converged	1.21[b],
	Anatase	
(101)	0.45	0.41[c], 0.44[d], 0.41[e], 0.35[f]
(100)	0.76	0.53[d], 0.51[e], 0.39[f]
(001)	1.04	0.96[c], 0.90[d], 0.96[e], 0.51[f]

[a] RPBE, PAW
[b] [112]
[c] [111]
[d] [113, 114]
[e] [107]
[e] [105]

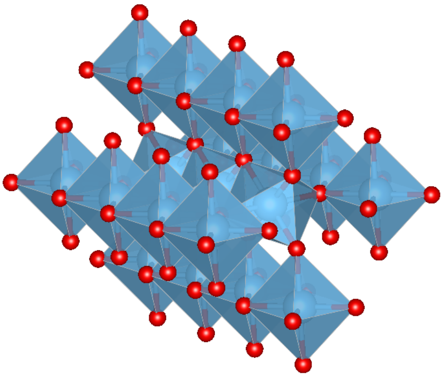

(a) Rutile

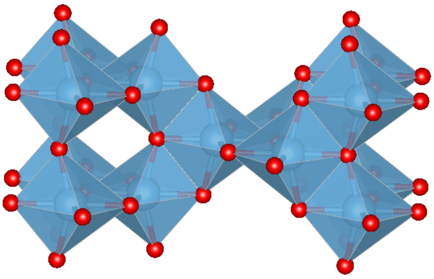

(b) Anatase

Figure 7.1: TiO_2 structures. Each vertex of the TiO_6 octahedron is shared with two other octahedra: in rutile through one corner- and one edge-type conductions; in anatase through two edge-type conductions.

7.1.2 Electronic and optical

TiO_2 is an n-type semiconductor[1] and the excess electrons originate from oxygen under-stoichiometry:

$$2\mathrm{O_O} \rightarrow \mathrm{O_2} + 2\mathrm{V_O^{2+}} + 4e^-. \tag{7.1}$$

Apart from oxygen vacancies (V_O) in various charge states, titanium interstitial (Ti_i) and vacancies (V_Ti) as well as more complex defects have been reported [115–117].

---

[1] High oxygen pressures could transform TiO_2 to a p-type semiconductor. Such material, however, has not been yet reported.

Both phases have similar electronic structure. The valence band is due to oxygen p states and its edge is formed from p-like orbitals perpendicular to the planar OTi_3 unit. The conduction band is due to titanium d states, and it is split into the e_g and t_{2g} symmetric components. (For the projected density of states onto atomic orbitals see paper I.)

The experimental optical band gaps in rutile and in anatase are 3.0 eV [118] and 3.3 eV [119], respectively. In rutile the direct and indirect band gaps are very close, the latter being 0.04 eV lower in energy (GW calculations); in anatase the band gap is indirect [120]. A characteristic feature of anatase optical absorption is an exponential increase of the absorption with the photon energy (Urbach tail) what suggests strong exciton effects [121].

7.2 Photocatalysis

Semiconductor photocatalysis is a process of accelerating a photochemical reaction by transferring photon energy to reactants via photogenerated electron-hole pairs in a semiconductor. Most of photocatalytic processes are electrochemical transformations. Photocatalyst there plays a role of a photoelectrode—photocathode for reduction half reaction:

$$\mathrm{Ox1} + e^- \rightarrow \mathrm{Red1}, \tag{7.2}$$

photoanode for oxidation half reaction:

$$\mathrm{Red2} + h^+ \rightarrow \mathrm{Ox2}. \tag{7.3}$$

Product formation at standard conditions (temperature $T = 298$ K, pressure $p = 1$ bar) and unit activities requires the electrochemical potential of the electron (hole) to be lower (higher) than the standard electrochemical potential of the respective half-reaction (see Fig. 7.2).

Fig. 1.2 illustrates the necessary steps of a photoelectrochemical process: photogeneration of electron-hole pairs (excitons); charge separation and transfer to surface reactive sites; and electrochemical reaction. Recombinations processes as well as side and reverse reactions limit photocatalytic performance. The efficiency of photoelectrochemical transformation of absorbed photons—a quantum yield η—can be expressed as

$$\eta = \frac{\phi_P}{\phi_P + \phi_U} \tag{7.4}$$

where ϕ_P and ϕ_U denote productive electron-hole pair transfer rate and unproductive electron-hole pair loss rate.

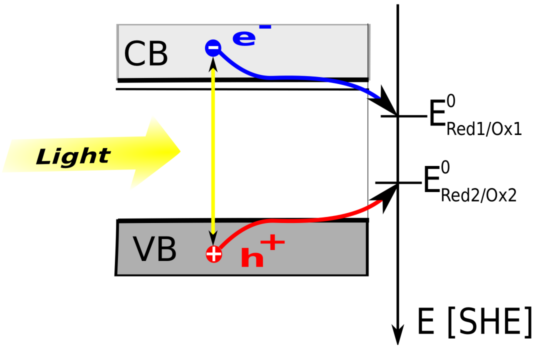

Figure 7.2: Semiconductor band alignment with respect to the electrochemical potential. For the photoelectrochemical process to proceed, the electrochemical potential of the photogenerated electrons (holes) must be lower (higher) that the electrochemical potential of the redox pair.

7.2.1 Effects of Charge Trapping

As discussed in chapter 3, in number of materials excess carriers localize either intrinsically (due to a strong electron-lattice interaction) and/or extrinsically (with assistance of a defect potential). The localized nature of charge carriers strongly affects the basic steps of photocatalytic processes.

First, charge trapping decreases carrier mobility. Carrier delivery to surface reactive sites precedes a photocatalytic reaction therefore a sluggish electron and/or hole transport may limit reaction kinetics. In particular, the important component of the mobility—normal to surface—can be strongly affected in surface layers. This is because of the electrostatic potential variations near surfaces, which create additional barriers for hopping transport.

Second, the spacial and energetic distributions of trapping sites may affect charge carrier availability for the reaction and recombination processes. For high quantum yields η, the electron and the hole populations should not overlap to minimize the recombination rate and be localized on surfaces to facilitate the reaction kinetics.

Third, trapping of the photogenerated carriers lowers the free energy available for redox transformations. For reduction on photocathode (oxidation on photoanode)[1] the electrochemical potential of the electrons (holes) must be lower (higher) than the standard redox potential of the respective half reaction.

Finally, charge localization influences charge transfer processes [122].

Charge trapping can have both negative and positive effects on photocatalyst

---

[1] Product formations at standard conditions (temperature $T = 298$ K, pressure $p = 1$ bar) and unit activities.

performance. If a photochemical process is limited by the kinetics of the photochemical reaction (charge transport is fast) then surface availability of the charge carriers will be decisive. Depending on the energetic and the spacial distribution of trapping sites, charge trapping can both increase and decrease the excess carrier density on surfaces (see paper IV). On the other hand, if the photochemical process is limited by carrier transport to surfaces (the reaction kinetics is fast) then charge trapping can be regarded as unfavorable as it decreases carriers mobility.

7.3 Hole trapping in TiO$_2$

Localized hole states in photoexcited TiO$_2$ have been observed in number of experiments. In particular, solid evidence comes from electron paramagnetic resonance (EPR) measurements which detect unpaired spin density localized on oxygen atoms [12–22].
Another technique that proves a localized nature of the photogenerated holes is the transient absorption spectroscopy. The hole absorption spectra consist of broad peak, typical to vibronic transitions [23–29], whereas free carrier absorption is qualitatively different (the absorption coefficient is $\propto \omega^{-\beta}$ with $\beta \approx 2$ [123]).
Photoluminescence (PL) provides less direct evidence as PL transitions involve both the photogenerated electron and hole. The PL transitions are at sub-band gap energies therefore involve band gap states. Similarly to the absorption band, the emission band is also broad, suggesting a vibronic nature of PL transitions [124–131].

7.3.1 Trapping sites

The atomic structure of hole trapping sites in TiO$_2$ has been difficult to resolve, and centers such as surface hydroxyls groups (−OH), surface bridging oxygen atoms (>O) or lattice oxygens (>O−) have been proposed [6].
Among them surface hydroxyls have long been considered the primary hole trapping centers. EPR experiments, however, indicate that this is not the case since the H^1 hyperfine coupling is too small and only weakly anisotropic, and the EPR signal only slightly shifts in D_2O [13, 21]. Furthermore, the occupied levels of surface hydroxyl groups are below the VB edge therefore they can not trap thermalized holes [128, 132, 133].
Nakamura et al. therefore suggested surface lattice oxygens (>O−) as primary

hole trapping centers [128, 129, 134, 135]. This attribution, however, was disputed as inconsistent [133] with isotope labeling experiments [136].

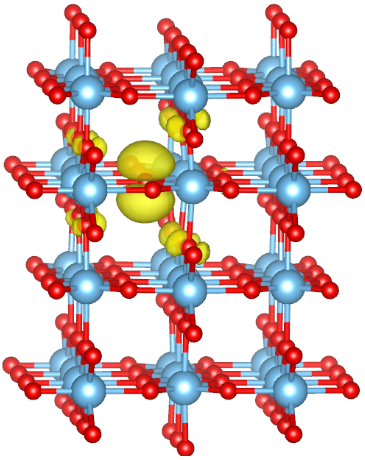

Figure 7.3: The hole trapping on oxygen lattice site in rutile.

Our calculations show that holes self-trap intrinsically on oxygen lattice sites forming O$^-$ small polarons (see paper I). The hole is localized on oxygen p-like orbital perpendicular to the flat OTi$_3$ unit of rutile and anatase structures (see Fig. 7.3).

In surface layers the trapping strength oscillates and converges to the bulk value within 1-2 nm below the surface. Fig. 7.4 shows energy profiles for the anatase (101) and (001) surfaces. Oscillations are larger for the (101) than for the (001) surface as the former is stacked form polar layers and the electrostatic effects determine trapping strength variations (see the bottoms panel of Fig. 7.4 for the electrostatic interaction energy $U(z)$ of the hole density localized at z with the surface potential).

For most anatase and rutile surfaces the trapping strength is the largest on the bridging oxygen site (>O). Hole trapping on this site is consistent with isotope labeling experiments [132, 133, 136]. Trapping on the bridging (or the subsurface) oxygen atoms is also in accordance with a weak hyperfine H^1 coupling of the EPR signal for samples in H$_2$O and a small change of the signal upon replacing H$_2$O with D$_2$O [13, 21]. Since most of EPR measurements are performed using polycrystalline samples and data acquisition times are typically on the order of microseconds, the EPR signal likely originates from the most stable, surface bridging sites. Recently EPR measurements performed on a single crystal rutile, however, were able to detected O$^-$ centers with the lattice oxygen symmetry >O− [14].

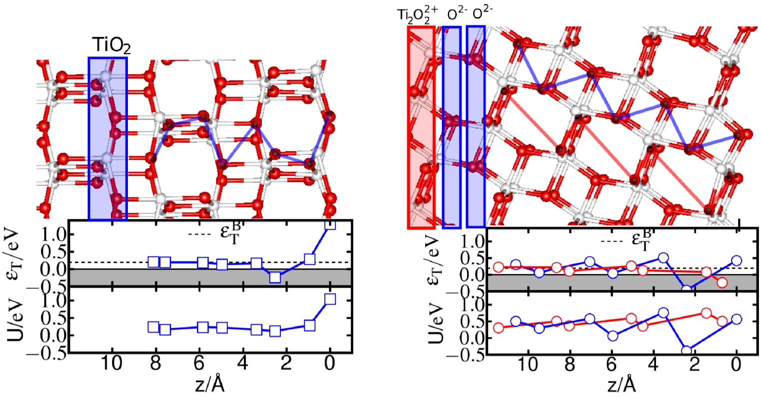

(a) {001}

(b) {011}

Figure 7.4: Self trapping energies ε_{T} with respect to the valence band edge for anatase anatase {001} and {011} surfaces. In surface layers hole stabilisation energies oscillate and within 1-2 nm below the surface the profiles converge to the bulk value $\varepsilon_{\mathrm{T}}^{\mathrm{B}}$. Larger surface hole strapping strength on {001} facets explains their stronger oxidative reactivity compared. $U(z)$ is the overlap of the electrostatic potential $V(\mathbf{r})$ and the density of the hole orbital $n_p(\mathbf{r}-z)$ centered at depth z. Similarity between $U(z)$ and ε_{T} suggest that variation of trapping strength in surface layers is an electrostatic effect. The shaded area denotes the valence band.

7.3.2 Trapping strength

We have found that the O^- small polaron state is 0.20 eV and 0.05 eV more stable than the delocalized hole state in anatase and rutile, respectively (see paper I). This result was obtained by correcting the energies for the inconsistent description of states with different degrees of localization (see chapter 4). Di Valentin et al. has found much larger trapping strength in anatase, 0.75 eV, using hybrid DFT [137].

A method that can access the energetics of band gap states is a photoluminescence (PL). The PL spectra of the photoexcited anatase consists of a Gaussian-shaped peak at 2.2 eV and a wide band extending to 3.4 eV (the anatase band gap energy) [124–131]. The former emission can be attributed to electron-hole recombinations involving trapped states of the hole and/or electron, whereas the latter is due to free (or shallowly trapped) carriers. It is not clear, however, if the signal originates form bulk or surface recombinations.
Nevertheless, the PL at 2.2 eV is consistent with trapping strength of 0.2 eV in the bulk, trapping strength of 0.75 eV [137] would result in PL at ≈ 1.75 eV.

PL transitions from surface states should be even at lower energies.
Rutile photoluminescence is located at 2.7-3.0 eV indicating week carrier trapping (3.0 eV is the rutile band gap energy). PL from the rutile (110) and (001) surface states have been detected at 1.8 eV [128–130].

7.3.3 Dynamics

Studies of dynamics of photogenerated electron-hole pairs in semiconductors require ultrafast techniques [138]. Transient absorption spectroscopy (TAS) allows to monitor carrier dynamics on a sub-picosecond time scale [139]. The method employs a short femtosecond laser pulse (pump) to generate electron-hole pairs and a second pulse (probe) to monitor the photogenerated charge carrier absorption. The spectra is a sum of the electron and the hole absorptions. By scavenging one type of carriers the spectra for the other can be can be recorded and thus both contributions resolved. For instance excess electrons in photoexcited TiO_2 can be removed by depositing Pt, or by suspending particle in a solution containing Ag^+ [23, 23–29]. Such procedure allows to attribute 450-550 nm (2.8-2.3 eV) range of the TAS spectra of TiO_2 to the trapped hole absorption [25–27, 29, 140].
The time evolution of photoexcited TiO_2 TAS spectra is characterised by several time scales. After the excitation the absorption spectra has free electron character that disappears due to trapping. Trapping time is longer at higher energies and takes 50-200 fs [26, 141–143]. The absorption then blue shifts within 1-3 ps to 550 nm (2.3 eV) [26, 29, 142, 144] and then to 450 nm (2.8 eV) within the next 20-100 ps [25–27, 29, 140]. The shape then remains unchanged on nanosecond time scale [24–27, 29, 140, 145].
Section 5.3.2 and paper V discusses the interpolaronic transitions of self-trapped holes in anatase. Positions of optical absorption bands depend on the location of trapping sites. Holes that are trapped in the bulk absorb light at 650 eV, whereas those trapped in surface layers absorb at higher energies. For holes trapped in the first, second, and third surface layer of anatase (101) surface the optical absorption bands peak at 400 nm, 470 nm, 520 nm, respectively, whereas for (001) surface at 350 eV. Thus the experimentally observed blue shift of the hole absorption spectra on a picosecond time scale can be associated with the hole transfer to surfaces. This interpretations is also consistent with experimental measurements of a picosecond hole transfers from photoexcited TiO_2 to SCN^- [96] or aliphatic alcohols [25].
Basing on this assignment, the time evolution of absorption spectra can be linked to the hole transfer toward surfaces. First, the longer trapping time at higher energies could be because of a delay time for free holes to reach the surface.
Second, the change of the spectra withing 1-3 ps can be linked to hole transport after the trapping. This fast transport can not be explained with the hopping

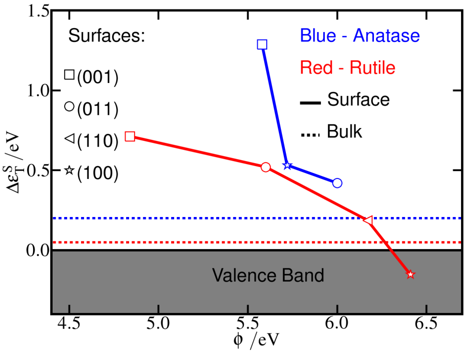

Figure 7.5: Surface hole trapping strength $\varepsilon_{\mathrm{T}}^{\mathrm{S}}$ plotted against the work functions ϕ. Shaded area denotes the valence band whereas dashed lines are the bulk self-trapping strengths $\varepsilon_{\mathrm{T}}^{\mathrm{B}}$ for rutile and anatase.

mechanism as a single hop would take a similar time (Eq. 6.17 and barrier hight of 0.1 eV, $\hbar\Omega = 40$ meV, $T = 300$ K results in a hoping frequency 1/8 ps^{-1}). If holes are not too deeply trapped, however, thermally excited holes could account for this fast transport.
Third, 20-100 ps shift of the spectra from 550 nm to 450 nm surface is likely due hoping transport of deeply trapped holes in surface layers.

7.3.4 Effects on photocatalysis

A picosecond hole delivery to surface reactive sites should not be a limitation for reactions occurring on a longer time scale such as a microsecond hole transfer to to toluene or acetonitryl [146] or millisecond-second water oxidation and oxygen evolution [28]. For slow reactions, charge trapping may reveal itself through its effect on excess charge distribution (see section 7.2.1) as the reactions rate depends on surface excess carrier concentration. For anatase and rutile surfaces hole trapping strength on surface sites vary significantly (up to ≈ 1 eV), see Fig. 7.5, and increases in the following order: for rutile {100}<{110}<{011}<{001}; and for anatase ({011}<{100}<{001}). Therefore there is a large thermodynamic driving force for an uneven distribution of the excess hole density among different facades.
Different reaction rates for the different TiO_2 facets have been indeed observed. For instance Pb^{2+} oxidation (PbO_2 deposition) [147–149] as well as anodic photoetching in H_2SO_4 [150] rates vary among rutile and anatase facades and the

oxidation rate increases with the surface hole trapping strength. These reaction are likely to be slow as they involve significant nuclear rearrangements.

Chapter 8

Conclusions and Outlook

In the present thesis has been studied the localized nature of photogenerated holes in TiO_2. It has been found that the holes self-trap on oxygen lattice sites forming O^- small polarons and anatase offers stronger hole trapping centers than rutile.

In surface layers the trapping strengths oscillate around the bulk value due to the electrostatic potential variation induced by crystal termination. For most surfaces the deepest hole traps are provided by bridging oxygen sites (>O).

Furthermore, trapping strength vary among different rutile and anatase facades and surface hole stability increases in the following order: for rutile $\{100\}<\{110\}<\{011\}<\{001\}$; and for anatase $(\{011\}<\{100\}<\{001\})$. This variation provides a large thermodynamic driving force (up to ≈ 1 eV) for an uneven distribution photogenerated holes among rutile and anatase facades, thus affects the hole availability for photoanodic oxidation reactions. For instance the calculated hole stability order positively correlates with experimental PbO_2 photodeposition and the anodic photoetching rates.

The assignment of the trapped hole optical absorption bands to interpolaronic (charge transfer) transitions has allowed to link the blue shift of TiO_2 transient absorption spectra to the trapped hole transfer towards surfaces. Different time scales of the hole dynamics, however, need to be clarified. In particular, hole transport in surface layers should be addressed in more detail.

Many unexplained aspects of TiO_2 photocatalysis, such as photoinduced hydrophilicity and large amount of experimental data renders this material particularly good subject for computational study. Furthermore, TiO_2, an abundant material, has a technological advantage, especially since many materials become scarce. Increasing capabilities for materials nano-structuring can lead to new functionalities. Here a good example is TiO_2 based memristor—a memory element first envisioned in 1971 but developed only in 2008 [151].

In addition, this thesis has dealt with the problem of a biased treatment of states with different degrees of localization. It has been shown that a more consistent comparison of energies of such states can be achieved by removing the total energy nonlinearity. This a posteriori correction has been applied to number of cases, and resulted in improvement of otherwise qualitative incorrect results. The study of charge localization/delocaliztion processes with DFT, however, remains a big challenge, and a development of new XC functionals that can more accurately account for fractional electron systems is needed.

List of Figures

Bibliography

[1] C. F. Goodeve and J. A. Kitchener. The mechanism of photosensitisation by solids. *Trans. Faraday Soc.*, 34:902, 1938.

[2] Akira Fujishima and Kenichi Honda. Electrochemical photolysis of water at a semiconductor electrode. *Nature*, 238:37, 1972.

[3] Kazuhito Hashimoto. Tio2 photocatalysis: A historical overview and future prospects. *Jpn. J. Appl. Phys.*, 44:8269, 2005.

[4] AL Linsebigler, GQ LU, and JT Yates. Photocatalysis on tio2 surfaces - principles, mechanisms, and selected results. *Chem. Rev.*, 95:735, 1995.

[5] O Carp, CL Huisman, and A Reller. Photoinduced reactivity of titanium dioxide. *Prog. Solid State Chem.*, 32:33, 2004.

[6] Akira Fujishima, Xintong Zhang, and Donald A. Tryk. Tio2 photocatalysis and related surface phenomena. *Surf. Sci. Rep.*, 63:515, 2008.

[7] E Borgarello, J Kiwi, E Pelizzetti, M Visca, and M Gratzel. Photochemical cleavage of water by photocatalysis. *Nature*, 289:158, 1981.

[8] Xiaobo Chen, Shaohua Shen, Liejin Guo, and Samuel S. Mao. Semiconductor-based photocatalytic hydrogen generation. *Chem. Rev.*, 110:6503, 2010.

[9] Krishnan Rajeshwar. Hydrogen generation at irradiated oxide semiconductor-solution interfaces. *J. Appl. Electrochem.*, 37:765, 2007.

[10] AJ Nozik. Photoelectrochemistry - introductory lecture. *Faraday Discuss.*, 70:7, 1980.

[11] Michael G. Walter, Emily L. Warren, James R. McKone, Shannon W. Boettcher, Qixi Mi, Elizabeth A. Santori, and Nathan S. Lewis. Solar water splitting cells. *Chem. Rev.*, 110:6446, 2010.

[12] Nada M. Dimitrijevic, Zoran V. Saponjic, Bryan M. Rabatic, Oleg G. Poluektov, and Tijana Rajh. Effect of size and shape of nanocrystalline tio2 on photogenerated charges. an epr study. *J. Phys. Chem. C*, 111: 14597, 2007.

[13] R. F. Howe and M. Gratzel. Epr study of hydrated anatase under uv irradiation. *J. Phys. Chem.*, 91:3906, 1987.

[14] Shan Yang, A. T. Brant, and L. E. Halliburton. Photoinduced self-trapped hole center in tio2 crystals. *Phys. Rev. B*, 82:035209, 2010.

[15] T Berger, M Sterrer, O Diwald, and E Knozinger. Charge trapping and photoadsorption of o-2 on dehydroxylated tio2 nanocrystals - an electron paramagnetic resonance study. *ChemPhysChem*, 6:2104, 2005.

[16] T Berger, M Sterrer, O Diwald, E Knozinger, D Panayotov, TL Thompson, and JT Yates. Light-induced charge separation in anatase tio2 particles. *J. Phys. Chem. B*, 109:6061, 2005.

[17] T Berger, M Sterrer, S Stankic, J Bernardi, O Diwald, and E Knozinger. Trapping of photogenerated charges in oxide nanoparticles. *Mater. Sci. Eng. C: Biomimetic Supramol. Syst.*, 25:664, 2005.

[18] DC Hurum, AG Agrios, SE Crist, KA Gray, T Rajh, and MC Thurnauer. Probing reaction mechanisms in mixed phase tio2 by epr. *J. Electron Spectrosc. Relat. Phenom.*, 150:155, 2006.

[19] DC Hurum, AG Agrios, KA Gray, T Rajh, and MC Thurnauer. Explaining the enhanced photocatalytic activity of degussa p25 mixed-phase tio2 using epr. *J. Phys. Chem. B*, 107:4545, 2003.

[20] SC Ke, TC Wang, MS Wong, and NO Gopal. Low temperature kinetics and energetics of the electron and hole traps in irradiated tio2 nanoparticles as revealed by epr spectroscopy. *J. Phys. Chem. B*, 110:11628, 2006.

[21] OI Micic, YN Zhang, KR Cromack, AD Trifunac, and MC Thurnauer. Photoinduced hole transfer from tio2 to methanol molecules in aqueous-solution studied by electron-paramagnetic-resonance. *J. Phys. Chem.*, 97: 13284, 1993.

[22] O I. Micic, Y N Zhang, K R Cromack, A D Trifunac, and Mc Thurnauer. Trapped holes on tio2 colloids studied by electron-paramagnetic-resonance. *J. Phys. Chem.*, 97:7277, 1993.

[23] T Yoshihara, R Katoh, A Furube, Y Tamaki, M Murai, K Hara, S Murata, H Arakawa, and M Tachiya. Identification of reactive species in photoexcited nanocrystalline tio2 films by wide-wavelength-range (400-2500 nm) transient absorption spectroscopy. *J. Phys. Chem. B*, 108:3817, 2004.

[24] IA Shkrob and MC Sauer. Hole scavenging and photo-stimulated recombination of electron - hole pairs in aqueous tio2 nanoparticles. *J. Phys. Chem. B*, 108:12497, 2004.

[25] Y Tamaki, A Furube, M Murai, K Hara, R Katoh, and M Tachiya. Direct observation of reactive trapped holes in tio2 undergoing photocatalytic oxidation of adsorbed alcohols: Evaluation of the reaction rates and yields. *J. Am. Chem. Soc.*, 128:416, 2006.

[26] Yoshiaki Tamaki, Akihiro Furube, Ryuzi Katoh, Miki Murai, Kohjiro Hara, Hironori Arakawa, and M. Tachiya. Trapping dynamics of electrons and holes in a nanocrystalline tio2 film revealed by femtosecond visible/near-infrared transient absorption spectroscopy. *C. R. Chim.*, 9: 268, 2006.

[27] Yoshiaki Tamaki, Akihiro Furube, Miki Murai, Kohjiro Hara, Ryuzi Katoh, and M. Tachiya. Dynamics of efficient electron-hole separation in tio2 nanoparticles revealed by femtosecond transient absorption spectroscopy under the weak-excitation condition. *Phys. Chem. Chem. Phys.*, 9:1453, 2007.

[28] Junwang Tang, James R. Durrant, and David R. Klug. Mechanism of photocatalytic water splitting in tio2. reaction of water with photoholes, importance of charge carrier dynamics, and evidence for four-hole chemistry. *J. Am. Chem. Soc.*, 130:13885, 2008.

[29] Yoshiaki Tamaki, Kohjiro Hara, Ryuzi Katoh, M. Tachiya, and Akihiro Furube. Femtosecond visible-to-ir spectroscopy of tio2 nanocrystalline films: Elucidation of the electron mobility before deep trapping. *J. Phys. Chem. C*, 113:11741, 2009.

[30] Emanuele Finazzi, Cristiana Di Valentin, Gianfranco Pacchioni, and Annabella Selloni. Excess electron states in reduced bulk anatase tio2: Comparison of standard gga, gga plus u, and hybrid dft calculations. *J. Chem. Phys.*, 129(15):154113, 2008.

[31] N. Aarori Deskins, Roger Rousseau, and Michel Dupuis. Localized electronic states from surface hydroxyls and polarons in tio2(110). *J. Phys. Chem. C*, 113(33):14583, 2009.

[32] N. Aaron Deskins, Roger Rousseau, and Michel Dupuis. Defining the role of excess electrons in the surface chemistry of tio2. *J. Phys. Chem. C*, 114 (13):5891, 2010.

[33] N. Aaron Deskins and Michel Dupuis. Intrinsic hole migration rates in tio2 from density functional theory. *J. Phys. Chem. C*, 113(1):346, 2009.

[34] N. Aaron Deskins, Roger Rousseau, and Michel Dupuis. Distribution of ti3+ surface sites in reduced tio2. *J. Phys. Chem. C*, 115:7562, 2011.

[35] N. Aaron Deskins and Michel Dupuis. Electron transport via polaron hopping in bulk tio2: A density functional theory characterization. *Phys. Rev. B*, 75(19), 2007.

[36] S. J. Clark, J. Robertson, S. Lany, and A. Zunger. Intrinsic defects in zno calculated by screened exchange and hybrid density functionals. *Phys. Rev. B*, 81, 2010.

[37] J Laegsgaard and K Stokbro. Hole trapping at al impurities in silica: A challenge for density functional theories. *Phys. Rev. Lett.*, 86:2834, 2001.

[38] Walter R. L. Lambrecht. Which electronic structure method for the study of defects: A commentary. *Phys. Status Solidi B*, 248:1547, 2011.

[39] Stephan Lany and Alex Zunger. Polaronic hole localization and multiple hole binding of acceptors in oxide wide-gap semiconductors. *Phys. Rev. B*, 80:085202, 2009.

[40] G Pacchioni, F Frigoli, D Ricci, and JA Weil. Theoretical description of hole localization in a quartz al center: The importance of exact electron exchange. *Phys. Rev. B*, 63, 2001.

[41] L. H. Thomas. The calculation of atomic fields. *Mathematical Proceedings of the Cambridge Philosophical Society*, 23:542, 1926.

[42] Enrico Fermi. A statistical method for the determination of some atomic properties and the application of this method to the theory of the periodic system of elements. *Z. Phys.*, 48:73, 1928.

[43] P. Hohenberg and W. Kohn. Inhomogeneous electron gas. *Phys. Rev.*, 136:B864, 1964.

[44] Tosio Kato. On the eigenfunctions of many-particle systems in quantum mechanics. *Comm. Pure Appl. Math.*, 10:151, 1957.

[45] Mel Levy. Electron densities in search of hamiltonians. *Phys. Rev. A*, 26: 1200, 1982.

[46] J P Perdew, R G Parr, M Levy, and J L Balduz. Density-functional theory for fractional particle number - derivative discontinuities of the energy. *Phys. Rev. Lett.*, 49:1691, 1982.

[47] R. Gaudoin and K. Burke. Lack of hohenberg-kohn theorem for excited states. *Phys. Rev. Lett.*, 93(17):173001–, 2004.

[48] A Nagy and K D Sen. Higher-order cusp of the density in certain highly excited states of atoms and molecules. *J. Phys. B: At., Mol. Opt. Phys.*, 33:1745, 2000.

[49] Jeppe Gavnholt, Thomas Olsen, Mads Engelund, and Jakob Schiotz. Delta self-consistent field method to obtain potential energy surfaces of excited molecules on surfaces. *Phys. Rev. B*, 78:075441, 2008.

[50] L. D. Landau. Über die bewegung der elektronen in kristalgitter. *Phys. Z. Sowjetunion*, 3:644, 1933.

[51] David Emin and T. Holstein. Adiabatic theory of an electron in a deformable continuum. *Phys. Rev. Lett.*, 36:323–, 1976.

[52] Y. Shinozuka and Y. Toyozawa. Self-trapping in mixed-crystal - clustering, dimensionality, percolation. *J. Phys. Soc. Jpn.*, 46:505, 1979.

[53] A. M. Stoneham, J. Gavartin, A. L. Shluger, A. V. Kimmel, D. Munoz Ramo, H. M. Ronnow, G. Aeppli, and C. Renner. Trapping, self-trapping and the polaron family. *J. Phys.: Condens. Matter*, 19:255208, 2007.

[54] Peter Broqvist, Audrius Alkauskas, and Alfredo Pasquarello. A hybrid functional scheme for defect levels and band alignments at semiconductor-oxide interfaces. *Phys. Status Solidi A: Appl. Mat.*, 207:270, 2010.

[55] C. W. M. Castleton, A. Hoglund, and S. Mirbt. Density functional theory calculations of defect energies using supercells. *Model. Simul. Mater. Sci. Eng.*, 17:084003, 2009.

[56] Peter Deak, Balint Aradi, Thomas Frauenheim, and Adam Gali. Challenges for ab initio defect modeling. *Mater. Sci. Eng. B*, 154:187, 2008.

[57] Hannu-Pekka Komsa, Peter Broqvist, and Alfredo Pasquarello. Alignment of defect levels and band edges through hybrid functionals: Effect of screening in the exchange term. *Phys. Rev. B*, 81:205118, 2010.

[58] Stephan Lany and Alex Zunger. Accurate prediction of defect properties in density functional supercell calculations. *Model. Simul. Mater. Sci. Eng.*, 17:084002, 2009.

[59] Risto M. Nieminen. Issues in first-principles calculations for defects in semiconductors and oxides. *Model. Simul. Mater. Sci. Eng.*, 17:084001, 2009.

[60] Fumiyasu Oba, Minseok Choi, Atsushi Togo, Atsuto Seko, and Isao Tanaka. Native defects in oxide semiconductors: a density functional approach. *J. Phys.: Condens. Matter*, 22:384211, 2010.

[61] Gianfranco Pacchioni. Modeling doped and defective oxides in catalysis with density functional theory methods: Room for improvements. *J. Chem. Phys.*, 128:182505, 2008.

[62] G Pacchioni. Ab initio theory of point defects in oxide materials: structure, properties, chemical reactivity. *Solid State Sci.*, 2:161, 2000.

[63] CG Van de Walle and J Neugebauer. First-principles calculations for defects and impurities: Applications to iii-nitrides. *J. Appl. Phys.*, 95: 3851, 2004.

[64] Aron J. Cohen, Paula Mori-Sánchez, and Weitao Yang. Fractional charge perspective on the band gap in density-functional theory. *Phys. Rev. B*, 77:115123, 2008.

[65] Aron J. Cohen, Paula Mori-Sanchez, and Weitao Yang. Second-order perturbation theory with fractional charges and fractional spins. *J. Chem. Theory Comput.*, 5:786, 2009.

[66] Peter Elliott, Morrel H. Cohen, Adam Wasserman, and Kieron Burke. Density functional partition theory with fractional occupations. *J. Chem. Theory Comput.*, 5:827, 2009.

[67] R. Haunschild, T. M. Henderson, C. A. Jimenez-Hoyos, and G. E. Scuseria. Many-electron self-interaction and spin polarization errors in local hybrid density functionals rid a-9925-2010. *J. Chem. Phys.*, 133:134116, 2010.

[68] Paula Mori-Sanchez, Aron J. Cohen, and Weitao Yang. Discontinuous nature of the exchange-correlation functional in strongly correlated systems. *Phys. Rev. Lett.*, 102:066403, 2009.

[69] Paula Mori-Sanchez, Aron J. Cohen, and Weitao Yang. Localization and delocalization errors in density functional theory and implications for band-gap prediction. *Phys. Rev. Lett.*, 100:146401, 2008.

[70] A Ruzsinszky, JP Perdew, and GI Csonka. Binding energy curves from nonempirical density functionals. i. covalent bonds in closed-shell and radical molecules. *J. Phys. Chem. A*, 109:11006, 2005.

[71] Adrienn Ruzsinszky, John P. Perdew, Gabor I. Csonka, Oleg A. Vydrov, and Gustavo E. Scuseria. Spurious fractional charge on dissociated atoms: Pervasive and resilient self-interaction error of common density functionals. *J. Chem. Phys.*, 125:194112, 2006.

[72] J F Janak. Proof that delta-e-delta-ni=epsilon-i in density-functional theory. *Phys. Rev. B*, 18:7165, 1978.

[73] John P. Perdew, Adrienn Ruzsinszky, Gabor I. Csonka, Oleg A. Vydrov, Gustavo E. Scuseria, Viktor N. Staroverov, and Jianmin Tao. Exchangp and correlation in open systems of fluctuating electron number. *Phys. Rev. A*, 76:040501, 2007.

[74] Adrienn Ruzsinszky, John P. Perdew, Gabor I. Csonka, Oleg A. Vydrov, and Gustavo E. Scuseria. Density functionals that are one- and two- are not always many-electron self-interaction-free, as shown for h-2(+), he-2(+), lih+, and ne-2(+). *J. Chem. Phys.*, 126:104102, 2007.

[75] B Hammer, L. B. Hansen, and J. K. Norskov. Improved adsorption energetics within density-functional theory using revised perdew-burke-ernzerhof functionals. *Phys. Rev. B*, 59:7413, 1999.

[76] Jochen Heyd, Gustavo E. Scuseria, and Matthias Ernzerhof. Hybrid functionals based on a screened coulomb potential. *J. Chem. Phys.*, 118:8207, 2003.

[77] Xiao Zheng, Aron J. Cohen, Paula Mori-Sánchez, Xiangqian Hu, and Weitao Yang. Improving band gap prediction in density functional theory from molecules to solids. *Phys. Rev. Lett.*, 107:026403–, 2011.

[78] Ismaila Dabo, Andrea Ferretti, Nicolas Poilvert, Yanli Li, Nicola Marzari, and Matteo Cococcioni. Koopmans' condition for density-functional theory. *Phys. Rev. B*, 82:115121–, 2010.

[79] VI Anisimov, J Zaanen, and OK Andersen. Band theory and mott insulators - hubbard-u instead of stoner-i. *Phys. Rev. B*, 44:943, 1991.

[80] S. L. Dudarev, G. A. Botton, S. Y. Savrasov, C. J. Humphreys, and A. P. Sutton. Electron-energy-loss spectra and the structural stability of nickel oxide: an lsda+u study. *Phys. Rev. B*, 57:1505, 1998.

[81] Matteo Cococcioni and Stefano de Gironcoli. Linear response approach to the calculation of the effective interaction parameters in the lda+u method. *Phys. Rev. B*, 71:035105, 2005.

[82] Heather J. Kulik, Matteo Cococcioni, Damian A. Scherlis, and Nicola Marzari. Density functional theory in transition-metal chemistry: A self-consistent hubbard u approach. *Phys. Rev. Lett.*, 97:103001, 2006.

[83] Vivaldo Leiria Campo Jr and Matteo Cococcioni. Extended dft + u + v method with on-site and inter-site electronic interactions. *J. Phys.: Condens. Matter*, 22:055602, 2010.

[84] J P Perdew and A Zunger. Self-interaction correction to density-functional approximations for many-electron systems. *Phys. Rev. B*, 23:5048, 1981.

[85] Simon Klüpfel, Peter Klüpfel, and Hannes Jónsson. Importance of complex orbitals in calculating the self-interaction-corrected ground state of atoms. *Phys. Rev. A*, 84:050501, 2011.

[86] O. A. Vydrov, G. E. Scuseria, and J. P. Perdew. Tests of functionals for systems with fractional electron number. *Journal of Chemical Physics*, 126(15):154109, 2007.

[87] David Emin. Optical properties of large and small polarons and bipolarons. *Phys. Rev. B*, 48:13691–, 1993.

[88] T. He. Optical absorption of free small polarons at high temperatures. *Phys. Rev. B*, 51:16689–, 1995.

[89] OF Schirmer. Intra-versus inter-small-polaron transitions in a deep oxide acceptor. *J. Phys. Chem. C*, 11:L65, 1978.

[90] O. F. Schirmer. O- bound small polarons in oxide materials. *J. Phys.: Condens. Matter*, 18:R667, 2006.

[91] TH Keil. Shapes of impurity absorption bands in solids. *Phys. Rev.*, 140: A601–&, 1965.

[92] M Lax. The franck-condon principle and its application to crystals. *J. Chem. Phys.*, 20:1752, 1952.

[93] A. M. Stoneham. *Theory of Defects in Solids.* Oxford University Press, 1975.

[94] OF Schirmer. Optical-absorption of small polarons bound in octahedral symmetry - v- type centers in alkaline-earth oxides. *Z. Phys. B*, 24:235, 1976.

[95] B. H. Rose and D. L. Cowan. Electric-field-induced dichroism of the v-center in mgo. *Solid State Commun.*, 15:775, 1974.

[96] DW Bahnemann, M Hilgendorff, and R Memming. Charge carrier dynamics at tio2 particles: Reactivity of free and trapped holes. *J. Phys. Chem. B*, 101:4265, 1997.

[97] H. Böttger and V. V. Bryksin. Hopping conductivity in ordered and disordered solids (i). *Phys. Status Solidi B*, 78:9, 1976.

[98] H Bottger and VV Bryksin. Hopping conductivity in ordered and disordered solids .2. *Phys. Status Solidi B: Basic Res.*, 78:415, 1976.

[99] H. Bottger and V. V. Bryksin. *Hopping Conduction in Solids.* VCH, 1985.

[100] Michael A. Henderson. A surface science perspective on photocatalysis. *Surf. Sci. Rep.*, 66:185, 2011.

[101] JK Burdett, T Hughbanks, GJ Miller, JW Richardson, and JV Smith. Structural electronic relationships in inorganic solids - powder neutron-diffraction studies of the rutile and anatase polymorphs of titanium-dioxide at 15 and 295-k. *J. Am. Chem. Soc.*, 109:3639, 1987.

[102] U Diebold. The surface science of titanium dioxide. *Surf. Sci. Rep.*, 48: 53, 2003.

[103] L. Gerward and J. Staun Olsen. Post-Rutile High-Pressure Phases in TiO_2. *J. Appl. Crystallogr.*, 30:259, 1997.

[104] Ahmed El Goresy, Ming Chen, Leonid Dubrovinsky, Philippe Gillet, and Gunther Graup. An ultradense polymorph of rutile with seven-coordinated titanium from the ries crater. *Science*, 293:1467, 2001.

[105] A. S. Barnard and P. Zapol. Predicting the energetics, phase stability, and morphology evolution of faceted and spherical anatase nanocrystals. *J. Phys. Chem. B*, 108:18435, 2004.

[106] Hengzhong Zhang and Jillian F. Banfield. Understanding polymorphic phase transformation behavior during growth of nanocrystalline aggregates: Insights from tio2. *J. Phys. Chem. B*, 104:3481, 2000.

[107] Daniel R. Hummer, James D. Kubicki, Paul R. C. Kent, Jeffrey E. Post, and Peter J. Heaney. Origin of nanoscale phase stability reversals in titanium oxide polymorphs. *J. Phys. Chem. C*, 113:4240, 2009.

[108] Hai Bo Jiang, Qian Cuan, Ci Zhang Wen, Jun Xing, Di Wu, Xue-Qing Gong, Chunzhong Li, and Hua Gui Yang. Anatase tio2 crystals with exposed high-index facets. *Angew. Chem. Int. Ed.*, 123:3848, 2011.

[109] Min Liu, Lingyu Piao, Lei Zhao, Siting Ju, Zijie Yan, Tao He, Chunlan Zhou, and Wenjing Wang. Anatase tio2 single crystals with exposed {001} and {110} facets: facile synthesis and enhanced photocatalysis. *Chem. Commun.*, 46:1664, 2010.

[110] Shengwei Liu, Jiaguo Yu, and Mietek Jaroniec. Anatase tio2 with dominant high-energy 001 facets: Synthesis, properties, and applications. *Chem. Mater.*, 23:4085, 2011.

[111] Xiao Hua Yang, Zhen Li, Chenghua Sun, Hua Gui Yang, and Chunzhong Li. Hydrothermal stability of 001 faceted anatase tio2. *Chem. Mater.*, 23: 3486, 2011.

[112] H. Perron, C. Domain, J. Roques, R. Drot, E. Simoni, and H. Catalette. Optimisation of accurate rutile tio2 (110), (100), (101) and (001) surface models from periodic dft calculations. *Theor. Chem. Acc.*, 117:565, 2007.

[113] Michele Lazzeri, Andrea Vittadini, and Annabella Selloni. Structure and energetics of stoichiometric tio2 anatase surfaces. *Phys. Rev. B*, 63:155409, 2001.

[114] M Lazzeri, A Vittadini, and A Selloni. Structure and energetics of stoichiometric tio2 anatase surfaces (vol 63, art no 155409, 2001). *Phys. Rev. B*, 65, 2002.

[115] Benjamin J. Morgan and Graeme W. Watson. Polaronic trapping of electrons and holes by native defects in anatase tio2. *Phys. Rev. B*, 80:233102, 2009.

[116] Benjamin J. Morgan and Graeme W. Watson. A density functional theory plus u study of oxygen vacancy formation at the (110), (100), (101), and (001) surfaces of rutile tio2. *J. Phys. Chem. C*, 113:7322, 2009.

[117] Jun He and Susan B. Sinnott. Ab initio calculations of intrinsic defects in rutile tio2. *J. Am. Ceram. Soc.*, 88:737, 2005.

[118] J. Pascual, J. Camassel, and H. Mathieu. Resolved quadrupolar transition in tio_2. *Phys. Rev. Lett.*, 39:1490, 1977.

[119] H. Tang, H. Berger, P.E. Schmid, F. Lévy, and G. Burri. Photoluminescence in tio2 anatase single crystals. *Solid State Commun.*, 87:847, 1993.

[120] Wei Kang and Mark S. Hybertsen. Quasiparticle and optical properties of rutile and anatase tio_2. *Phys. Rev. B*, 82:085203, 2010.

[121] H Tang, F Levy, H Berger, and P E Schmid. Urbach tail of anatase tio2. *Phys. Rev. B*, 52:7771, 1995.

[122] BB Smith and AJ Nozik. Theoretical studies of electron transfer and electron localization at the semiconductor-liquid interface. *J. Phys. Chem. B*, 101:2459, 1997.

[123] Mark Fox. *Optical properties of solids; 2nd ed.* Oxford Master Series in Condensed Matter Physics. Oxford Univ. Press, Oxford, 2010.

[124] Lucia Cavigli, Franco Bogani, Anna Vinattieri, Valentina Faso, and Giovanni Baldi. Volume versus surface-mediated recombination in anatase tio2 nanoparticles. *J. Appl. Phys.*, 106:053516, 2009.

[125] K Fujihara, S Izumi, T Ohno, and M Matsumura. Time-resolved photoluminescence of particulate tio2 photocatalysts suspended in aqueous solutions. *J. Photochem. Photobiol., B*, 132:99, 2000.

[126] Naomi Harada, Masako Goto, Koji Iijima, Hiroshi Sakama, Noriya Ichikawa, Hideyuki Kunugita, and Kazuhiro Ema. Time-resolved luminescence of tio2 powders with different crystal structures. *Jpn. J. Appl. Phys. 1*, 46:4170, 2007.

[127] Fritz J. Knorr, Dongshe Zhang, and Jeanne L. McHale. Influence of ticl4 treatment on surface defect photoluminescence in pure and mixed-phase nanocrystalline tio2. *Langmuir*, 23:8686, 2007.

[128] R Nakamura and Y Nakato. Primary intermediates of oxygen photoevolution reaction on tio2 (rutile) particles, revealed by in situ ftir absorption and photoluminescence measurements. *J. Am. Chem. Soc.*, 126:1290, 2004.

[129] R Nakamura, T Okamura, N Ohashi, A Imanishi, and Y Nakato. Molecular mechanisms of photoinduced oxygen evolution, pl emission, and surface roughening at atomically smooth (110) and (100) n-tio2 (rutile) surfaces in aqueous acidic solutions. *J. Am. Chem. Soc.*, 127:12975, 2005.

[130] Y Nakato, H Akanuma, Y Magari, S Yae, JI Shimizu, and H Mori. Photoluminescence from a bulk defect near the surface of an n-tio2 (rutile) electrode in relation to an intermediate of photooxidation reaction of water. *J. Phys. Chem. B*, 101:4934, 1997.

[131] Xiuli Wang, Zhaochi Feng, Jianying Shi, Guoqing Jia, Shuai Shen, Jun Zhou, and Can Li. Trap states and carrier dynamics of tio2 studied by photoluminescence spectroscopy under weak excitation condition. *Phys. Chem. Chem. Phys.*, 12:7083, 2010.

[132] P. Salvador. On the nature of photogenerated radical species active in the oxidative degradation of dissolved pollutants with tio2 aqueous suspensions: A revision in the light of the electronic structure of adsorbed water. *J. Phys. Chem. C*, 111:17038, 2007.

[133] Pedro Salvador. Mechanisms of water photooxidation at n-tio2 rutile single crystal oriented electrodes under uv illumination in competition with photocorrosion. *Prog. Surf. Sci.*, 86:41, 2011.

[134] R Nakamura, A Imanishi, K Murakoshi, and Y Nakato. In situ ftir studies of primary intermediates of photocatalytic reactions on nanocrystalline tio2 films in contact with aqueous solutions. *J. Am. Chem. Soc.*, 125: 7443, 2003.

[135] R Nakamura, N Ohashi, A Imanishi, T Osawa, Y Matsumoto, H Koinuma, and Y Nakato. Crystal-face dependences of surface band edges and hole reactivity, revealed by preparation of essentially atomically smooth and stable (110) and (100) n-tio2 (rutile) surfaces. *J. Phys. Chem. B*, 109: 1648, 2005.

[136] P. Bogdanoff and N. Alonso-Vante. A kinetic approach of competitive photoelectrooxidation of hcooh and h2o on tio2 anatase thin layers via on-line mass detection. *J. Electroanal. Chem.*, 379:415, 1994.

[137] Cristiana Di Valentin and Annabella Selloni. Bulk and surface polarons in photoexcited anatase tio2. *J. Phys. Chem. Lett.*, 2:2223, 2011.

[138] Jin Z. Zhang. Interfacial charge carrier dynamics of colloidal semiconductor nanoparticles. *J. Phys. Chem. B*, 104:7239, 2000.

[139] Rudi Berera, Rienk van Grondelle, and John Kennis. Ultrafast transient absorption spectroscopy: principles and application to photosynthetic systems. *Photosynth. Res.*, 101:105, 2009. 10.1007/s11120-009-9454-y.

[140] Akihiro Furube, Tsuyoshi Asahi, Hiroshi Masuhara, Hiromi Yamashita, and Masakazu Anpo. Direct observation of a picosecond charge separation process in photoexcited platinum-loaded tio2 particles by femtosecond diffuse reflectance spectroscopy. *Chem. Phys. Lett.*, 336:424, 2001.

[141] David E. Skinner, D. Philip Colombo, Joseph J. Cavaleri, and Robert M. Bowman. Femtosecond investigation of electron trapping in semiconductor nanoclusters. *J. Phys. Chem.*, 99:7853, 1995.

[142] Yoshinori Murakami, Junichi Nishino, Takuya Mesaki, and Yoshio Nosaka. Femtosecond diffuse-reflectance spectroscopy of various commercially available tio2 powders. *Spectrosc. Lett.*, 44:88, 2011.

[143] D. Philip Colombo, Kirsten A. Roussel, Jamal Saeh, David E. Skinner, Joseph J. Cavaleri, and Robert M. Bowman. Femtosecond study of the intensity dependence of electron-hole dynamics in tio2 nanoclusters. *Chem. Phys. Lett.*, 232:207, 1995.

[144] Xiujuan Yang and Naoto Tamai. How fast is interfacial hole transfer? in situ monitoring of carrier dynamics in anatase tio2 nanoparticles by femtosecond laser spectroscopy. *Phys. Chem. Chem. Phys.*, 3:3393, 2001.

[145] A Furube, T Asahi, H Masuhara, H Yamashita, and M Anpo. Charge carrier dynamics of standard tio2 catalysts revealed by femtosecond diffuse reflectance spectroscopy. *J. Phys. Chem. B*, 103:3120, 1999.

[146] Miki Murai, Yoshiaki Tamaki, Akihiro Furube, Kohjiro Hara, and Ryuzi Katoh. Reaction of holes in nanocrystalline tio2 films evaluated by highly sensitive transient absorption spectroscopy. *Catal. Today*, 120:214, 2007.

[147] T Ohno, K Sarukawa, and M Matsumura. Crystal faces of rutile and anatase tio2 particles and their roles in photocatalytic reactions. *New J. Chem.*, 26:1167, 2002.

[148] Eunyoung Bae, Naoya Murakami, and Teruhisa Ohno. Exposed crystal surface-controlled tio2 nanorods having rutile phase from ticl3 under hydrothermal conditions. *J. Mol. Catal. A: Chem.*, 300:72, 2009.

[149] Eunyoung Bae and Teruhisa Ohno. Exposed crystal surface-controlled rutile tio2 nanorods prepared by hydrothermal treatment in the presence of poly(vinyl pyrrolidone). *Appl. Catal. B: Environ.*, 91:634, 2009.

[150] T Kisumi, A Tsujiko, K Murakoshi, and Y Nakato. Crystal-face and illumination intensity dependences of the quantum efficiency of photoelectrochemical etching, in relation to those of water photooxidation, at n-tio2 (rutile) semiconductor electrodes. *J. Electroanal. Chem.*, 545:99, 2003.

[151] Dmitri B. Strukov, Gregory S. Snider, Duncan R. Stewart, and R. Stanley Williams. The missing memristor found. *Nature*, 453(7191):80–83, 2008.

Paper I

Zawadzki P., Jacobsen K. W., Rossmeisl J.; Electronic hole localization in rutile and anatase TiO_2—Self-interaction correction in Δ-SCF DFT. *Chemical Physics Letters* **506** 42 (2011)
doi:10.1016/j.cplett.2011.03.001

Chemical Physics Letters 506 (2011) 42–45

Contents lists available at ScienceDirect

Chemical Physics Letters

journal homepage: www.elsevier.com/locate/cplett

Electronic hole localization in rutile and anatase TiO_2 – Self-interaction correction in Δ-SCF DFT

Paweł Zawadzki *, Karsten Wedel Jacobsen, Jan Rossmeisl

Department of Physics, Center for Atomic-Scale Materials Design, Technical University of Denmark, DK-2800 Kgs. Lyngby, Denmark

ARTICLE INFO

Article history:
Received 30 November 2010
In final form 2 March 2011
Available online 4 March 2011

ABSTRACT

We study electronic hole localization in rutile and anatase titanium dioxide by means of Δ-Self-Consistent Field Density Functional Theory. In order to compare stabilities of the localized and the delocalized hole states we introduce a simple correction to the wrong description of the localization processes within DFT. The correction removes the non-linearity of energy for fractional excitations. We show that the self-trapped and the delocalized hole states have comparable stability in rutile TiO_2 whereas in anatase the former is favoured. The theoretical prediction of the adiabatic Potential Energy Surfaces for the hole localization compares well with published photoluminescence measurements.

1. Introduction

Density Functional Theory (DFT) with the (semi-)local Density Functional Approximation (DFA) is an inexpensive computational method for a wide spectrum of electronic structure problems. However, the introduced approximations turn out to be too crude for certain problems. One of these is the description of localized states in extended systems where spurious electron self-interaction leads to an over-delocalization of electronic states. The evident symptom of this tendency is the wrong curvature of the energy for fractional electron systems. GGAs are δN-convex thus they favor fractional, delocalized states [1,2]. This bias is especially apparent in the failure to predict relative stabilities of free and (self-)trapped charges [3].

An example process where charge trapping is of great technological importance is photo-catalysis on TiO_2 surfaces [4]. TiO_2 is utilized in processes such as water and air purification and is of potential use as a catalyst for solar into chemical energy conversion [4–6]. Oxidative power for those processes is delivered through trapped hole states generated in photoexcited TiO_2. Although a lot of research has been done, the exact nature of the hole traps in TiO_2 remains unclear. Measurements such as electron paramagnetic resonance [7,8], photoluminescence [9–11], transient absorption [12,13] spectroscopies or oxygen photodesorption [14] show that hole trapping sites in rutile and anatase TiO_2 are centered on oxygen atoms, and that both surface and lattice sites are present. However, the two phases differ in photo-catalytic activity and the precise reason for this is not clear [4]. Certainly, a different charge trapping capability of the two phases [15] is of vital importance here as the energetics of trapping sites in the bulk and in the surface layers will determine holes availability for the reaction and their oxidative power.

In this Letter, we consider hole trapping in the bulk of photoexcited TiO_2 by means of the Δ-Self-Consistent Field (Δ-SCF) DFT [16]. We introduce a simple procedure which is parameter free and provides a systematic way to search for trapping sites in extended systems. To estimate relative stabilities of localized versus delocalized states we correct DFT energies for the biased description of charge localization processes. We associate this correction with the non-linearity of the energy for fractional excitations and apply the procedure to rutile and anatase TiO_2. We find that the electronic hole localizes on a lattice oxygen forming a small-polaron [17–19] trapping center in agreement with experimental measurements [20] and LDA + U calculations [21]. Our work provides relative stabilities of the delocalized and the localized hole states and compares them with photoluminescence data.

2. Computational details

We performed DFT calculations within the Projector-Augmented Wave formalism implemented in the GPAW code [22,23]. Pseudo wave-functions/densities and potentials were represented on an uniform, real-space grid with a spacing of 0.2 Å. To account for exchange–correlation effects we used the RPBE functional [24].

Excited-state (ES) energies were obtained with generalized Δ-SCF [25,16]. Application of the more rigorous, but computationally much more demanding, ES methodologies is not feasible since the localized nature of the trapped hole state involves long-range atomic relaxations which can only be captured in large systems.

The TiO_2 rutile ($P4_2/mnm$) and anatase ($I4_1/amd$) atomic structures were optimized, and the resulting cell parameters (rutile: $a = 4.691$, $c = 2.975$, $u = 0.3061$; anatase: $a = 3.829$, $c = 9.744$,

---

* Corresponding author. Fax: +45 4593 2399.
E-mail address: zawpaw@fysik.dtu.dk (P. Zawadzki).

0009-2614/$ - see front matter © 2011 Elsevier B.V. All rights reserved.
doi:10.1016/j.cplett.2011.03.001

$u = 0.2062$) differed by less than 3% from the experimental ones [5,26]. We have studied a range of unit cell sizes defined by lattice vectors $\mathbf{a}' = m(\mathbf{a} + \mathbf{b})$, $\mathbf{b}' = n(\mathbf{a} - \mathbf{b})$, $\mathbf{c}' = o\mathbf{c}$ for rutile; and $\mathbf{a}' = p\mathbf{a}$, $\mathbf{b}' = q\mathbf{b}$, $\mathbf{c}' = r\mathbf{c}$ for anatase, $\mathbf{a}$, $\mathbf{b}$ and $\mathbf{c}$ being the vectors of the respective tetragonal crystallographic cells. For rutile $[m,n,o] = [3,2,2]$ and for anatase $[p,q,r] = [2,3,2]$ cells were found sufficient to describe localization phenomena, both containing 144 atoms. The Brillouin zone was sampled on $3 \times 2 \times 2$ and $3 \times 2 \times 1$ Monhorst–Pack mesh for rutile and anatase, respectively.

3. Procedure

Application of (semi-) local DFA to polaronic systems is often troublesome. Classic example of their failure is hole localization around aluminum substitution in α-quartz. GGA predict the hole to be delocalized over four oxygen atoms surrounding the defect [27] whereas experiments clearly indicate that the hole is mostly confined to one oxygen.

The problem of charge self-trapping is even more difficult as the delocalization error takes its maximum – we compare a completely delocalized state with a fully localized one. Therefore a simple use of (semi)-local DFA does not provide localized solution for the electronic hole in TiO_2. Here we approach the problem by making an assumption on the nature of localized hole state and then we estimate its stability in a possibly unbiased way. The procedure consist of four steps: we (1) produce an initial hole orbital; (2) find a distortion associated with the presence of a hole orbital in the Valence Band (VB); (3) construct the Potential Energy Surface (PES) along the distortion; (4) correct PES for the over-delocalization error.

3.1. Initial guess

A reasonable choice for a trial hole orbital can be derived from the Projected Density of States (PDOS) (Figure 1). Both in rutile and anatase the top of the VB is composted mostly form the oxygen's p orbitals perpendicular to the flat OTi_3 unit, $p_\perp$. Since $p_\perp$ participates in π(Ti–O) bonding which is considerably weaker than σ(Ti–O) it forms the top of the VB and offers less destabilization upon electron removal. Choice of a single $p_\perp$ is also supported through a group theoretical reasoning: $p_\perp$ is the only oxygen's atomic orbital belonging to the b_1 irreducible representation of the local OTi_3 symmetry point group – C_{2v}. Since b_1 is largely non-bonding it is highest in energy. We construct the orbital by taking the difference between the true and the pseudo oxygen atomic $p_\perp$ orbital inside an augmentation sphere of radius 1.4 Bohr, $\phi_{p_\perp}(\mathbf{r}) = [\phi^{\mathrm{O}}_{p_\perp}(\mathbf{r} - \mathbf{R}^{\mathrm{O}}) - \tilde{\phi}^{\mathrm{O}}_{p_\perp}(\mathbf{r} - \mathbf{R}^{\mathrm{O}})]$, where $\mathbf{R}^{\mathrm{O}}$ is the position of the chosen oxygen atom and $\tilde{\phi}^{\mathrm{O}}_{p_\perp}, \phi^{\mathrm{O}}_{p_\perp}$ are pseudo partial wave and all-electron partial wave respectively, of the atom [16].

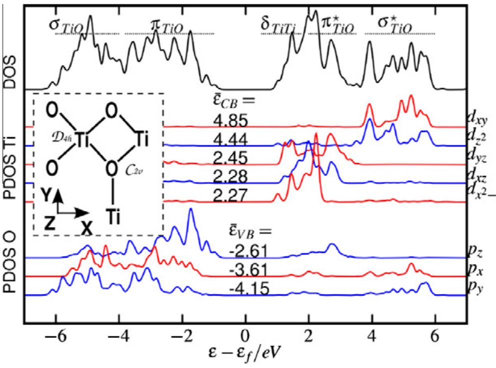

Figure 1. Rutile – PDOS onto O and Ti atomic orbitals. $\hat{\varepsilon}$ denote projections centers. The inset shows the local symmetry around O and Ti atoms. The top of the VB is formed from the oxygen's $p_\perp$ (the p orbital perpendicular to the flat OTi_3 unit, p_z in the inset coordinates) contributing to the π(TiO) bond.

3.2. Finding distortion

To find the distortion associated with the presence of the localized hole orbital, $\phi_{p_\perp}$, in the VB we excite an electron from its normalized expansion in M occupied states to the lowest conduction band. This is achieved by modifying the electron density at each self-consistency cycle,

$$n(\mathbf{r}) = \sum_{i=1}^{M} |\psi_i(\mathbf{r})|^2 - \sum_{i,j=1}^{M} c_i^* c_j \psi_i^*(\mathbf{r})\psi_j(\mathbf{r}) + |\psi_{M+1}(\mathbf{r})|^2, \tag{1}$$

where $c_i = \langle \phi_{p_\perp} | \psi_i \rangle / \left\{ \sum_{j=1}^{M} |\langle \phi_{p_\perp} | \psi_j \rangle|^2 \right\}^{1/2}$. With such constraint density we now relax the atomic structure. Initially the expansion of the hole orbital, $\phi_{p_\perp}(\mathbf{r})$, in Bloch states is largely delocalized over all the equivalent oxygen atoms. However, as the self-consistency cycle and the structure relaxation proceed a single band-gap state localized on the chosen oxygen atom is formed. Hence a rather simple approximation, $\phi_{p_\perp}(\mathbf{r})$, leads to a state having O^- ionic character. The electron removal weakens the π(TiO) bond and results in its elongation. The direction of the distortion around the created localized hole is along the OTi_3 breathing mode.

3.3. Constructing PES

Using linear interpolation between the equilibrium Ground State (GS) geometry and the distorted one we generate set of structures. Along this path we then calculate PES by removing an electron from the top of the Valence Band (VB) and placing it at the bottom of the Conduction Band (CB).

$$n(\mathbf{r}) = \sum_{i}^{M-1} |\psi_i(\mathbf{r})|^2 + |\psi_{M+1}(\mathbf{r})|^2. \tag{2}$$

The frontier bands correspond to VB and CB maximum and minimum, respectively, as large unit cells are used and the band structure is multiply folded. The resulting PES are shown on Figure 2. Clearly, for a larger distortion the ES PES deviates from an ideal

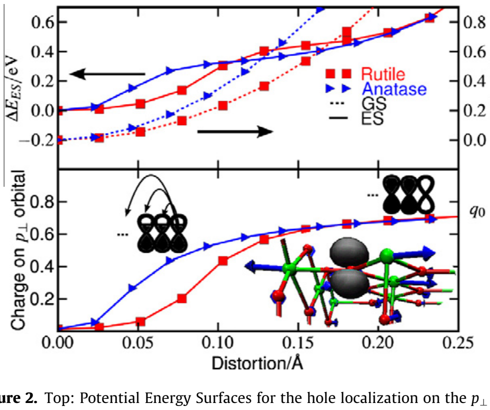

Figure 2. Top: Potential Energy Surfaces for the hole localization on the $p_\perp$ orbital as a function of the distortion along the OTi_3 breathing mode in rutile and anatase. The distortion is an average elongation of the three Ti–O bonds surrounding the trapping center. Bottom: charge localization on the $p_\perp$ orbital. q_0 denotes the maximum contribution of the $p_\perp$ orbital to the hole density. The inset structure shows the direction of the distortion for rutile. Charge localization seems to lead to stabilization of the excited state.

harmonic behavior of the GS PES and the presence of a localized and delocalized states can be distinguished. The hole self-traps on one sites and the degree of localization is monitored with the contribution of $\phi_{p_\perp}(\mathbf{r})$ to the hole density. This contribution increases from $\propto N^{-1}$, N being unit cell size, to about 0.75 (for all cell sizes used) as the structure distorts. The excited electron remains delocalized over all the titanium atoms thus it does not bias the localized or the delocalized nature of the hole through Coulombic interaction. We calculated a non-screened Coulomb interaction between the hole and the excited electron and found a difference of $\approx 0.05 - 0.10$ eV between the localized and the delocalized hole states. The inclusion of screening (optical dielectric constant $\epsilon_\infty \approx 7$ [28]) makes this effect negligible. A proper description of titanium d states might lead to electron self-trapping [29] but it is not an issue here.

3.4. Correcting PES

States along the calculated PES are characterized by different degree of localization. At the non-distorted structure the hole is delocalized over all the oxygen lattice sites, the degree of the hole localization is $1/N$ where N is the number of oxygen lattice sites. As we move along the distorting coordinate the hole localizes on one site therefore the degree of localization tends to 1. δN-convexity of (semi-) local DFA energetically favors charge delocalization therefore areas on PES due to more localized states are erroneously elevated. To correct for this inconsistent description we employ the fact that the exact DFT energy is linear with a change in the occupation of the Highest Occupied State (HOS) [30]. The more localized the HOS is the larger is its nonlinear deviation. If HOS is completely delocalized (delocalized limit) a straight line behavior is recovered, though with incorrect slope [2].

The ES energy is generally not linear in fractional excitation number. However, at low intensity excitation when one of the excited carries remains delocalized over large unit cell the electron–hole interaction is small and more importantly constant along the distortion. The latter is in analogy to the interaction of a charge with uniformly charged background. Therefore only a residual, fixed nonlinearly will be added to a larger effect due to charge localization.

Accordingly, by removing the non-linearity of ES energy at different distortion we achieve a more consistent description – we treat all the points along ES PES at delocalized limit. Assuming that the shape of GS PES is correct along the distortion the ES energy at delocalized limit equals

$$E_{\rm ES}^{\infty} = E_{\rm ES} - E_{\rm LC} = E_{\rm GS} + \left.\frac{\partial E_{\rm ES}(\lambda)}{\partial \lambda}\right|_{\lambda=0}, \qquad (3)$$

where λ is fractional excitation number and E_{LC} is the sought correction to ES PES.

We calculate the correction to the ES PES at different distortion by constructing, $E_{ES}(\lambda)$ and fitting to a parabola $E_{ES}(\lambda) = a\,\lambda^2 + b\lambda + c$, where a is the sought correction, E_{LC} (Figure 3a).

4. Discussion

On Figure 3b the corrected PESs are presented. In rutile stabilities of the delocalized and the localized hole stats are comparable, whereas in anatase the latter is favoured by 0.2 eV. Energetics of band gap states can be accessed with photoluminescence (PL) measurements. At low temperatures a PL peak of a vibronic transition is centered at the direct (Franck–Condon) transition from the minimum of the ES PES to the GS PES (see the inset in Figure 3b). Neglecting the difference between zero point energies of the GS and the ES the position of the PL peak is given by $P = E_g - R - S$, where E_g is the band gap (3.0 eV and 3.2 eV [5] for rutile and anatase, respectively), R is the GS energy associated with the excited state PES displacement and S is the small-polaron stabilization. Accordingly, we locate PL peaks at 2.2 and 2.5 eV for anatase and rutile, respectively. The P value for anatase is smaller that for rutile, despite anatase larger band gap, E_g. The reason for this is both stronger polaron binding and larger energy associated with the distortion, R. The experimental value of the PL transition for anatase, measured picoseconds after excitation, amounts to 2.3 eV and is red-shifted by 0.2 eV within nanoseconds [11]. For rutile only nanosecond data is available and values in the range of 2.6–2.9 eV [9,10] are reported. Sub-nanosecond evolution of the photoluminesence [11], and also of the absorption [13] spectra, is possibly due to redistribution of holes between trapping sites both in the bulk and on the surface. The agreement between the experimental and the calculated values, and more importantly the prediction of a smaller P value for anatase despite a larger band gap, suggests that these transitions are due to the bulk hole small-polaron and the conduction band electron recombinations.

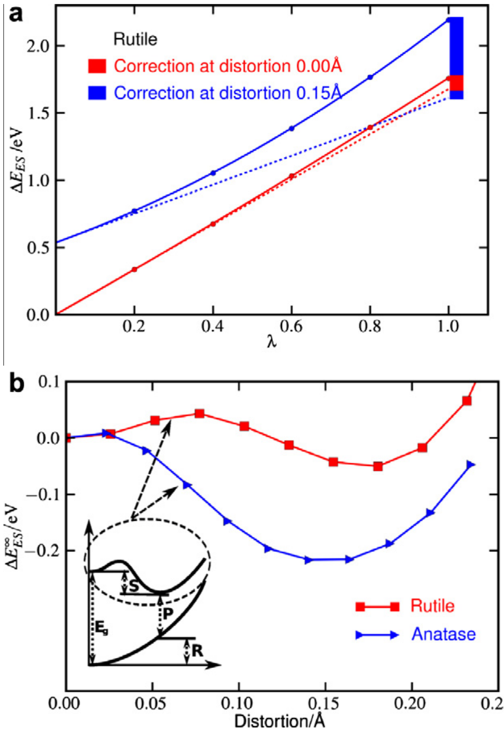

Figure 3. (a) Fractional excitation energy. λ is a fraction of an electron moved from the VB to the CB. The localization error is a non-linearity of the fractional excitation energy taken at one electron excitation ($\lambda = 1$). (b) The corrected PES. The distortion leads to the formation of a small-polaron trapping center. Since the VB edges in rutile and anatase coincide we conclude that anatase offers stronger bulk trapping centers. The inset scheme shows the photoluminescent transition, P, from the minimum of the ES PES. S is the small-polaron stabilization, R is the GS energy associated with the ES PES displacement.

Based on Huang–Rhys model [31] for a single frequency, ω_0, coupled vibronic transition we estimate the band's Full Width at Half Maximum. For Gaussian shaped peak $FWHM = 2\sqrt{2\ln(2)R\hbar\omega_o}$, what gives 0.5 and 0.7 eV using $\hbar\omega_o$ values of the high frequency longitudinal optic mode of 0.10 eV [32] and 0.11 eV [33] for rutile and anatase, respectively. Calculated widths agree with the observed broadness of the PL peaks.

The positions of the valence band edges with respect to the vacuum level coincide in rutile and anatase TiO_2 [4]. This allows us to directly compare stabilities of the localized hole states in both phases. Clearly anatase offers stronger bulk trapping centers.

5. Conclusion

In conclusion, our simple procedure provides a systematic way to search for trapping sites in extended systems. Application of Δ-SCF allows to probe a system with a desired density perturbation. To estimate stabilities of the found trapping sites we use a simple correction based on the non-linearity of the energy versus the fractional electron number. In this respect the procedure resembles DFT + U which for a certain parameter U removes the incorrect curvature of energy as a function of number of electrons [34]. However, DFT + U also affects eigenvalues, here we only remove the biased description of localization process. Our procedure is simple and parameter free. By far the largest material-specific variable is a choice of an initial orbital. A more thorough discussion will be published in future.

Using the described methodology we have shown that the stability of the delocalized and the self-trapped polaron hole states in rutile TiO_2 bulk is comparable, whereas in anatase the trapped hole state is favoured by 0.2 eV. Our results are in good agreement with the published photoluminesence spectra and provide a compelling argument favouring small-polaron as the searched hole trapping center in TiO_2.

Acknowledgments

CAMD is funded by the Lundbeck foundation. The Catalysis for Sustainable Energy initiative is funded by the Danish Ministry of Science, Technology and Innovation. This work was supported by the Danish Center for Scientific Computing. Support from the Danish Council for Technology and Innovation's FTP program and the Danish Council for Strategic Research though the HyCycle Center (No. 2104-07-0041) is acknowledged.

References

[1] P. Mori-Sanchez, A.J. Cohen, W. Yang, Phys. Rev. Lett. 102 (6) (2009) 066403.
[2] P. Mori-Sanchez, A.J. Cohen, W. Yang, Phys. Rev. Lett. 100 (14) (2008) 146401.
[3] J.L. Gavartin, P.V. Sushko, A.L. Shluger, Phys. Rev. B 67 (3) (2003) 035108.
[4] A. Fujishima, X. Zhang, D.A. Tryk, Surf. Sci. Rep. 63 (12) (2008) 515.
[5] U. Diebold, Surf. Sci. Rep. 48 (5-8) (2003) 53.
[6] A. Valdes, G.-J. Kroes, J. Phys. Chem. C 114 (3) (2010) 1701.
[7] O.I. Micic, Y.N. Zhang, K.R. Cromack, A.D. Trifunac, M. Thurnauer, J. Phys. Chem. 97 (28) (1993) 7277.
[8] R.F. Howe, M. Gratzel, J. Phys. Chem. 91 (14) (1987) 3906.
[9] K. Fujihara, S. Izumi, T. Ohno, M. Matsumura, J. Photochem. Photobiol. B 132 (1) (2000) 99.
[10] N. Harada, M. Goto, K. Iijima, H. Sakama, N. Ichikawa, H. Kunugita, K. Ema, Jpn. J. Appl. Phys. 1 46 (7A) (2007) 4170.
[11] L. Cavigli, F. Bogani, A. Vinattieri, V. Faso, G. Baldi, J. Appl. Phys. 106 (5) (2009) 053516.
[12] T. Yoshihara et al., J. Phys. Chem. B 108 (12) (2004) 3817.
[13] Y. Tamaki, A. Furube, M. Murai, K. Hara, R. Katoh, M. Tachiya, Phys. Chem. Chem. Phys. 9 (12) (2007) 1453.
[14] T.L. Thompson, J.T. Yates, J. Phys. Chem. B 109 (39) (2005) 18230.
[15] H. Tang, F. Levy, H. Berger, P.E. Schmid, Phys. Rev. B 52 (11) (1995) 7771.
[16] J. Gavnholt, T. Olsen, M. Engelund, J. Schiotz, Phys. Rev. B 78 (7) (2008) 075441.
[17] A.M. Stoneham et al., J. Phys.: Condens. Matter 19 (25) (2007) 255208.
[18] O.F. Schirmer, J. Phys.: Condens. Matter 18 (43) (2006) R667.
[19] A.L. Shluger, A.M. Stoneham, J. Phys.: Condens. Matter 5 (19) (1993) 3049.
[20] S. Yang, A.T. Brant, L.E. Halliburton, Phys. Rev. B 82 (3) (2010) 035209.
[21] N.A. Deskins, M. Dupuis, J. Phys. Chem. C 113 (1) (2009) 346.
[22] J.J. Mortensen, L.B. Hansen, K.W. Jacobsen, Phys. Rev. B 71 (3) (2005) 035109.
[23] J. Enkovaara et al., J. Phys.: Condens. Matter 22 (25) (2010) 253202.
[24] B. Hammer, L.B. Hansen, J.K. Norskov, Phys. Rev. B 59 (11) (1999) 7413.
[25] R.O. Jones, O. Gunnarsson, Rev. Mod. Phys. 61 (3) (1989) 689.
[26] J.I. Martinez, H.A. Hansen, J. Rossmeisl, J.K. Norskov, Phys. Rev. B 79 (4) (2009) 045120.
[27] J. Laegsgaard, K. Stokbro, Rev. Lett. 86 (53) (2001) 2834.
[28] G.M. Rignanese, X. Rocquefelte, X. Gonze, A. Pasquarello, Int. J. Quant. Chem. 101 (6) (2005) 793.
[29] E. Finazzi, C. Di Valentin, G. Pacchioni, A. Selloni, J. Chem. Phys. 129 (15) (2008) 154113.
[30] J.F. Janak, Phys. Rev. B 18 (12) (1978) 7165.
[31] A.M. Stoneham, Theory of Defects in Solids, Oxford University Press, 1975.
[32] J.G. Trayler, H.G. Smith, R.M. Nicklow, M.K. Wilkinson, Phys. Rev. B 3 (10) (1971) 3457.
[33] R.J. Gonzalez, R. Zallen, H. Berger, Phys. Rev. B 55 (11) (1997) 7014.
[34] M. Cococcioni, S. de Gironcoli, Phys. Rev. B 71 (3) (2005) 035105.

Paper II

Zawadzki P., Rossmeisl J., Jacobsen K. W.; Electronic hole transfer in rutile and anatase TiO_2: Effect of a delocalization error in the density functional theory on the charge transfer barrier height.
Physical Review B **84** 121203 (2011)
doi:10.1103/PhysRevB.84.121203

RAPID COMMUNICATIONS

PHYSICAL REVIEW B **84**, 121203(R) (2011)

Electronic hole transfer in rutile and anatase TiO_2: Effect of a delocalization error in the density functional theory on the charge transfer barrier height

Paweł Zawadzki,[*] Jan Rossmeisl, and Karsten Wedel Jacobsen
Department of Physics, Center for Atomic-Scale Materials Design, Technical University of Denmark, DK-2800 Kgs. Lyngby, Denmark

(Received 1 August 2011; published 29 September 2011)

We analyze the deformation of the potential energy surface (PES) due to the incorrect description of fractional electron systems (the nonlinearity of the energy with electron number) within a (semi)local density functional theory (DFT). Particularly sensitive to this failure are polaronic systems where charge localization is strongly coupled to lattice distortion. As an example we calculate the adiabatic PES for the hole transfer process in rutile and anatase TiO_2. (Semi)local DFT leads to qualitatively wrong, barrierless curves. Removal of the nonlinearity improves the PES shape and allows us to calculate hole mobilities.

DOI: 10.1103/PhysRevB.84.121203 PACS number(s): 72.20.Ee, 71.38.Ht, 71.15.Mb, 81.05.Hd

Introduction. Inconsistent treatment of states with different degrees of localization is a known failure of standard (semi)local density functional theory (DFT). A clear case is the dissociation of ${X_2}^+$ systems, such as ${He_2}^+$, for which the solutions X^{λ}-$X^{1-\lambda}$ should be degenerated for $0 \leqslant \lambda \leqslant 1$ at infinite separation whereas (semi)local DFT favors energetically homolytic $X^{+0.5}$-$X^{+0.5}$ dissociation.[1] This bias can be traced back to the behavior of fractional electron systems. The exact energy is linear as the number of electrons is varied between integers.[2] (Semi)local approximations are δN convex, thus solutions with electron density delocalized over several fragments are artificially favored over those having an electron localized on one fragment.[1,3,4] This biased behavior is related to the spurious electron self-interaction present in the common functionals. The relation, however, is by far not a straightforward one as it has been shown that even one-electron self-interaction free methods fail to reproduce linearity of the energy as a function of electron number.[1,3]

The inconsistent description of states with different degrees of localization is especially troublesome in polaronic systems where the charge localization is coupled to lattice distortion.[5,6] (Semi)local DFT artificially elevates areas on the potential energy surface (PES) related to more localized states, therefore it provides too delocalized solutions and incorrect atomic structures. Such PES deformations lead to incorrect pictures of processes where the degree of localization changes. Charge transfer is one of these processes as states along a charge transferring coordinate vary in the amount of charge sharing between the transferring sites. Here we analyze the PES arising from the electronic hole transfer in a technologically important photocatalyst—titanium dioxide. Transport of photogenerated holes to surfaces is a necessary step preceding photocatalytic reaction. In this material hole transfer largely determines photocatalytic efficiency as charge recombination in the bulk and reactions on the surface occur on similar time scales.[7] Various experimental techniques such as electron paramagnetic resonance,[8–10] transient absorption spectroscopy,[11–16] and photoluminescence[17–19] have revealed that photogenerated holes are trapped. Yet the nature of the trapping sites has remained obscure. Only recently it is becoming evident that holes self-trap intrinsically, both in rutile[8,20] and in anatase,[20] forming O^- small polarons.[21]

Model. To examine the effect of the δN convexity of (semi)local functionals on the PES for the self-trapped hole transfer, we first introduce a two-site model of the process. The hole is transferred between lattice sites L and R: $L^{\lambda} + R \rightarrow L + R^{\lambda}$, where the hole number can be fractional, $\lambda \in [0,1]$. We assume that the system interacts with the lattice via a single mode x and at $\lambda = 0$ the PES is harmonic, $E(x,\lambda = 0) = \frac{1}{2}Kx^2$. In the basis of orthonormal states localized on these sites, the electronic Hamiltonian takes the form

$$H_e = \begin{pmatrix} \varepsilon_L + Vx & t \\ t & \varepsilon_R - Vx \end{pmatrix}. \tag{1}$$

ε_L,ε_R are the on-site energies associated with the basis functions $|L\rangle$ and $|R\rangle$; t is the electronic coupling between the sites; and V is the strength of the electron-mode interaction.

In the static approximation—excluding the mode kinetic energy—the hole transfer occurs on a single PES. We construct the PES by removing a fraction λ of a hole from the highest occupied eigenstate ε of H_e:

$$\Delta E(x,\lambda) = \tfrac{1}{2}Kx^2 - \lambda\varepsilon(x). \tag{2}$$

For L and R representing O^{2-} lattice ions, ε is the antibonding solution of H_e:

$$\varepsilon(x) = \{\varepsilon_L + \varepsilon_R + t\sqrt{\tan[2\zeta(x)]^{-2} + 1}\}/2, \tag{3}$$

where $2\zeta(x) = \arctan{[2t/(\varepsilon_L - \varepsilon_R + 2Vx)]}$. In the following we consider $x \leqslant 0$; for $x > 0$ indexes L and R should be interchanged.

The hole then occupies the antibonding state $|\Psi\rangle = |L\rangle\cos[\zeta(x)] + |R\rangle\sin[\zeta(x)]$. If $\zeta(x) = 0$, the hole is confined to the L site; if $\zeta(x) = \pi/4$, the hole is equally shared between the two sites—therefore $\zeta(x)$ defines the degree of hole localization. In the absence of electron-mode coupling, ζ is independent of the coordinate x. The composition of eigenstates then does not change along the coordinate; the PES should not be deformed if there is any bias toward a more localized or delocalized state. Contrary, for a nonzero V the states along x differ in the degree of localization and their inconsistent treatment will result in a deformed PES.

A δN convexity of a (semi)local DFT leads to such inconsistent descriptions. For a quadratic behavior of the total energies of subsystems L and R, the on-site energies vary linearly with their occupations: $\varepsilon_L'(\zeta) = \varepsilon_L - \alpha\lambda\cos^2(\zeta)$ and

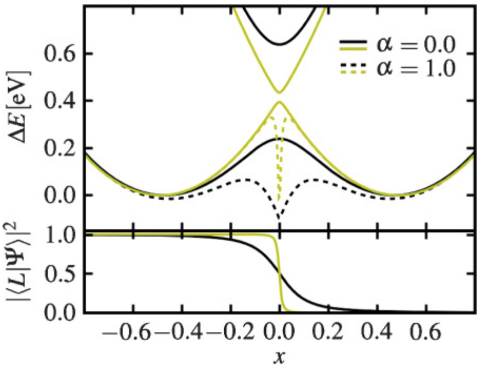

FIG. 1. (Color online) Top: The PESs for a two-state model of a hole transfer between equivalent fragments (full lines) and the deformed PESs due to δN convexity of the energy (dashed lines). Bottom: The hole localization on the L site. Curves are plotted for $t = 0.2$ eV (black) and $t = 0.02$ eV (yellow/gray) with $V = 1.7$, $K = 3.5$ eV corresponding to the path E in rutile [see Fig. 2 b]. Zero energy is at the minimum of the nondeformed PES and the deformed PES is aligned at $|x| \to \infty$.

$\varepsilon'_R(\zeta) = \varepsilon_R - \alpha\lambda\sin^2(\zeta)$, $\alpha > 0$. In Fig. 1 we show the effect of such a quadratic deviation on the PES when sites L and R are equivalent. For $\alpha = 0$ the PES exhibits a barrier at $x = 0$; for $\alpha = 1$ the PES shape is deformed around the transition point. The deformation increases with stronger electronic coupling t as the variation of the degree of localization extends toward larger $|x|$.

A non-self-consistent (preserving the site occupations) first-order expansion in α of the deformed PES yields

$$\Delta E'(x,\lambda) \approx \Delta E(x,\lambda) + \alpha\lambda^2 f[\zeta(x)], \qquad (4)$$

where $f(\zeta) = \{1 + [2\cos^2(\zeta) - 1]/\sqrt{\tan(2\zeta)^2 + 1}\}/2$, The correction to the PES of the system with a single hole is then $\alpha f(x)$ and can be calculated as a quadratic nonlinearity of $\Delta E'(x,\lambda)$. As one could expect, the correction is twice as large for the localized hole, $f(\zeta = 0) = 1$, compared to the hole shared between two sites, $f(|\zeta| \to \pi/4) = \frac{1}{2}$.

*Computational details.*We perform revised Perdew-Burke-Ernzerhof (RPBE) DFT[22] calculations within the projector augmented-wave formalism implemented in the GPAW code.[23] The wave functions, densities and potentials are described on a grid with a spacing of 0.2 Å. Atomic structures are defined by lattice vectors $\mathbf{a}' = 3(\mathbf{a} + \mathbf{b})$, $\mathbf{b}' = 2(\mathbf{a} - \mathbf{b})$, $\mathbf{c}' = 2\mathbf{c}$ for rutile, and $\mathbf{a}' = 3\mathbf{a}$, $\mathbf{b}' = 3\mathbf{b}$, $\mathbf{c}' = 2\mathbf{c}$ for anatase, $\mathbf{a}$, $\mathbf{b}$, and $\mathbf{c}$ being the vectors of the respective tetragonal crystallographic cells.[20,24] The Brillouin zone is sampled on $3 \times 2 \times 2$ and $2 \times 2 \times 1$ Monkhorst-Pack meshes for rutile and anatase, respectively.

The basic, oxygen-based, building motif of the anatase and rutile structures is a flat C_{2v}-symmetric OTi$_3$ unit. Upon hole localization the three OTi bonds elongate by 0.1–0.2 Å, preserving the initial symmetry.[20] The hole occupies a p-like orbital centered on the oxygen site and is perpendicular to the OTi$_3$ plane. In anatase such distortion renders the localized hole state more stable than the delocalized one, whereas in rutile the two have a comparable stability.[20] We consider hole transfer between two neighboring oxygen sites L and R. There are several such possible pairs of oxygen atoms (see Fig. 2). For each pair we construct a set of structures $\mathbf{Q}$ defined through linear interpolation between the distortions localized on the two sites $\mathbf{Q_L}$ and $\mathbf{Q_R}$, respectively: $\mathbf{Q} = [x(\mathbf{Q_R} - \mathbf{Q_L}) + \mathbf{Q_R} + \mathbf{Q_L}]/2$.

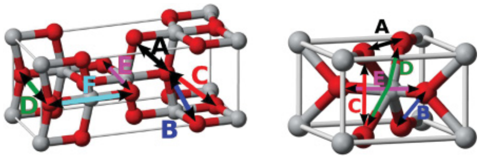

(a)Anatase (b)Rutile

FIG. 2. (Color online) Hole transfer paths between neighboring oxygen lattice sites in TiO$_2$.

For the constructed paths, we then calculate a set of PESs, $\Delta E'(x,\lambda)$, by removing a fraction of an electron λ from the highest occupied state and placing it at the bottom of the conduction band using linear expansion Δ-SCF (delta self-consistent field).[20,25,26] To correct the PESs for the spurious delocalization error, we remove the PES quadratic nonlinarity in λ: $\Delta E(x,\lambda = 1) = \Delta E'(x,\lambda = 1) - \alpha f(x)$.

Results and discussion. In the top plots of Fig. 3 we show PESs resulting from RPBE DFT calculations for different paths. The curves are seen to exhibit a drop around the transition point. We have shown that this characteristic kink is caused by the δN convexity of (semi)local functionals. At $x = 0$ the delocalization of the hole charge is the largest—the hole is shared between two sites; therefore the relative error with respect to the localized state takes its maximum. The quadratic nonlinearity of $\Delta E'(x,\lambda)$, αf, is shown in the middle plots of Fig. 3. The two-state model predicts that at large $|x|$ the correction should be twice as big as at $x = 0$. This ratio is not strictly conserved for some paths. The hole orbital

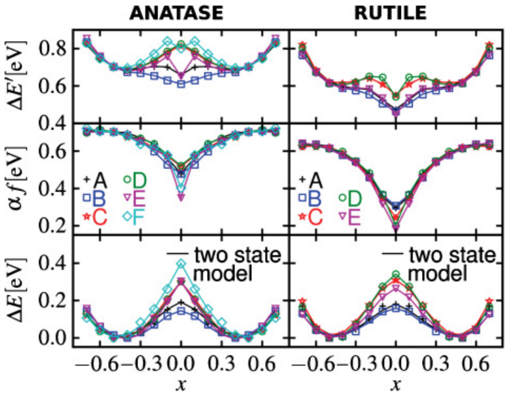

FIG. 3. (Color online) Top: PESs $\Delta E'(x,\lambda = 1)$ resulting from RPBE DFT calculations are plotted for different hole transfer paths. Middle: The nonlinearity of PES $\alpha f(x)$ with respect to hole number λ. Bottom: The corrected PES, $\Delta E(x,\lambda = 1) = \Delta E'(x,\lambda = 1) - \alpha f(x)$.

hybridizes with the surrounding orbitals, therefore the degree of localization can to some extent be different than in the model. In the bottom plots of Fig. 3 we show the corrected PESs, $\Delta E(x,\lambda = 1)$. Their shape is improved, notably the kinks around $x = 0$ are removed.

We use the thus corrected PESs to calculate high-temperature hole mobility. At high T small-polaron transport is dominated by the hopping mechanism. If the relative dynamics of the hole is fast compared to lattice fluctuations, the hole instantaneously follows the lattice coordinate and the charge transfer proceeds via barrier crossing at the transition point—the adiabatic limit. The hopping frequency in this case is given by[27]

$$k = [\Omega/(2\pi)] \exp\left[-E_b^{\mathrm{ad}}/(k_B T)\right], \qquad (5)$$

where E_b^{ad} is the adiabatic barrier height and Ω is the transferring mode frequency. In the nonadiabatic regime the hole is not able to follow the distortion. The transfer between two sites occurs at the intersection of two nonadiabatic PESs with a certain transition probability. The resulting hopping frequency in this case is given by[27]

$$k = t^2\sqrt{\pi/\left(4\hbar^2 E_b^{\mathrm{nad}} k_B T\right)}\exp\left[-E_b^{\mathrm{nad}}/\left(k_B T\right)\right], \qquad (6)$$

where $E_b^{\mathrm{nad}} = E_b^{\mathrm{ad}} + t$ is the nonadiabatic barrier height and t is the electronic coupling. We discriminate between these cases by calculating the parameter $\eta_2 = t^2/(\hbar\Omega\sqrt{E^{\mathrm{nad}}kT})$ describing the relative inertia of the nuclear and electronic motion.[27] For $\eta_2 > 1$ we assume adiabatic transport and otherwise the nonadiabatic one. At 1300 K we find all the nearest paths in rutile and paths A and B in anatase adiabatic. Apart from paths C and E in rutile, this is in accordance with wave-function calculations[28] (our notation $ABC\ldots$ corresponds to $DFBCEA$ and $BCADE$ in Ref. 28 for anatase and rutile, respectively).

We calculate the drift mobility using the Einstein-Smoluchowski relation $\mu = eD/(k_B T)$. D is the average hole diffusion coefficient $D = \sum_{i\in \mathrm{A}\ldots} n_i k_i |\mathbf{R_i}|^2/3$, where n_i is a number of equivalent paths, k_i is the transfer frequency, and $|\mathbf{R_i}|$ is the transfer distance. The two-site model for small-polaron hopping holds if $\eta_1 = t/E_b^{\mathrm{nad}} \ll 1$.[27] For anatase we find $\eta_1 \in (0.05,0.56)$ eV and for rutile $\eta_1 \in (0.27, 0.67)$ eV. Smaller η_1 in anatase indicates that the hole in this phase is more localized. (For what is also reflected in larger nonlinearities αf, see the middle plots in Fig. 3.)

The characteristic parameters of the different hole transfer paths in anatase and rutile are shown in the Supplemental Material.[29] We only note here that $\hbar\Omega$ ($\approx$20 meV in rutile and $\approx$40 meV in anatase) is much lower than the highest-frequency mode at $\sim$100 meV used to calculate hole mobility in Ref. 28. We find our values in accordance with the fact that the transfer coordinate arises mostly from the displacements of the cationic sublattice corresponding to the breathing mode of the flat $\mathrm{OTi_3}$ unit. Such vibrations resemble the optical modes B_{1g} at 50 meV and 64 meV in anatase[30] and B_{1u} at 14 meV and 50 meV in rutile.[31]

In units of $\mathrm{cm^2\,V^{-1}\,s^{-1}}$, mobilities measured in electrical conductivity experiments at 1300 K are 0.25 (Ref. 32) for single crystal and 0.16,[32] 5.0×10^{-2} (Ref. 33) for polycrystalline samples. At this temperature we find hole mobilities of 5.2×10^{-2} and 4.0×10^{-2} for anatase and rutile, respectively. At 873 K the transient grating technique predicts a value of 0.18,[34] whereas we find 3.3×10^{-2} for anatase and 3.1×10^{-2} for rutile.

Clearly, the calculated values underestimate the hole mobility. A better guess for the transition points (achieved by constraining the hole to be equally shared between the hole transferring sites) lowers the adiabatic barriers from $E_{\mathrm{ad}} \in (0.14,0.39)$ to $E_{\mathrm{ad}} \in (0.09,0.39)$ eV in anatase and from $E_{\mathrm{ad}} \in (0.14,0.29)$ to $E_{\mathrm{ad}} \in (0.06,0.21)$ eV in rutile, whereas only barrierless paths could provide mobilities close to the experimental ones.

This underestimation is likely due to the contribution of valence-band (VB) holes to the hole conduction mechanism. At 1300 K—assuming hole stabilization of 0.05 eV in rutile and 0.2 eV in anatase[20]—$\sim$39% and $\sim$14% of the total hole concentration occupies the VB in rutile and anatase, respectively. Two types of hole transport mechanisms are more evident at lower temperatures, where the disparity between the band and small-polaron mobilities increases (the latter becomes relatively immobile). Room-temperature experiments indicate the existence of two hole dynamics time scales: a fast one, after excitation—hole transfer to the surface within $\tau \approx r^2 D/(kT)$, where r is the particle diameter and D corresponds to the VB hole diffusion coefficient; and a much slower, nanosecond-microsecond decay of surface trapped holes.[11–19] We think that these two time scales are related to the VB band and the small-polaron transport mechanisms.

Conclusion. In summary, we have shown that the spurious nonlinearity of the total energy in a (semi)local DFT leads to a significant deformation of the PES if the states on the PES differ in the degree of charge localization. As an example we studied the electronic hole hopping in $\mathrm{TiO_2}$. (Semi)local DFT results in a quantitatively incorrect barrierless PES. By removing the energy nonlinearity in the fractional hole number from the PES, we improved the PES shape. With the thus corrected PES we calculated high-temperature hole hopping mobilities. Our results indicate that both the trapped and the VB holes contribute to the hole transport mechanism.

CAMD is funded by the Lundbeck foundation. This work was supported by the Danish Center for Scientific Computing. Support from the Danish Council for Technology and Innovation's FTP program and the Danish Council for Strategic Research though the HyCycle Center (No. 2104-07-0041) is acknowledged.

---

[*] zawpaw@fysik.dtu.dk

[1] A. Ruzsinszky, J. P. Perdew, G. I. Csonka, O. A. Vydrov, and G. E. Scuseria, J. Chem. Phys. **126**, 104102 (2007).

[2] J. F. Janak, Phys. Rev. B **18**, 7165 (1978).

[3] A. Ruzsinszky, J. P. Perdew, G. I. Csonka, O. A. Vydrov, and G. E. Scuseria, J. Chem. Phys. **125**, 194112 (2006).

[4] J. P. Perdew, A. Ruzsinszky, G. I. Csonka, O. A. Vydrov, G. E. Scuseria, V. N. Staroverov, and J. Tao, Phys. Rev. A **76**, 040501 (2007).

[5] J. L. Gavartin, P. V. Sushko, and A. L. Shluger, Phys. Rev. B **67**, 035108 (2003).

[6] S. Lany and A. Zunger, Phys. Rev. B **80**, 085202 (2009).

[7] A. Fujishima, X. Zhang, and D. A. Tryk, Surf. Sci. Rep. **63**, 515 (2008).

[8] S. Yang, A. T. Brant, and L. E. Halliburton, Phys. Rev. B **82**, 035209 (2010).

[9] O. I. Micic, Y. N. Zhang, K. R. Cromack, A. D. Trifunac, and M. Thurnauer, J. Phys. Chem. **97**, 7277 (1993).

[10] R. F. Howe and M. Gratzel, J. Phys. Chem. **91**, 3906 (1987).

[11] T. Yoshihara, R. Katoh, A. Furube, Y. Tamaki, M. Murai, K. Hara, S. Murata, H. Arakawa, and M. Tachiya, J. Phys. Chem. B **108**, 3817 (2004).

[12] Y. Tamaki, A. Furube, R. Katoh, M. Murai, K. Hara, H. Arakawa, and M. Tachiya, C. R. Chim. **9**, 268 (2006).

[13] D. Bahnemann, M. Hilgendorff, and R. Memming, J. Phys. Chem. B **101**, 4265 (1997).

[14] A. Furube, T. Asahi, H. Masuhara, H. Yamashita, and M. Anpo, J. Phys. Chem. B **103**, 3120 (1999).

[15] Y. Tamaki, A. Furube, M. Murai, K. Hara, R. Katoh, and M. Tachiya, Phys. Chem. Chem. Phys. **9**, 1453 (2007).

[16] X. Yang and N. Tamai, Phys. Chem. Chem. Phys. **3**, 3393 (2001).

[17] L. Cavigli, F. Bogani, A. Vinattieri, V. Faso, and G. Baldi, J. Appl. Phys. **106**, 053516 (2009).

[18] N. Harada, M. Goto, K. Iijima, H. Sakama, N. Ichikawa, H. Kunugita, and K. Ema, Jpn. J. Appl. Phys. 1 **46**, 4170 (2007).

[19] K. Fujihara, S. Izumi, T. Ohno, and M. Matsumura, J. Photochem. Photobiol. B **132**, 99 (2000).

[20] P. Zawadzki, K. W. Jacobsen, and J. Rossmeisl, Chem. Phys. Lett. **506**, 42 (2011).

[21] O. F. Schirmer, J. Phys. Condens. Matter **18**, R667 (2006).

[22] B. Hammer, L. B. Hansen, and J. K. Norskov, Phys. Rev. B **59**, 7413 (1999).

[23] J. Enkovaara *et al.*, J. Phys. Condens. Matter **22**, 253202 (2010).

[24] J. I. Martinez, H. A. Hansen, J. Rossmeisl, and J. K. Norskov, Phys. Rev. B **79**, 045120 (2009).

[25] J. Gavnholt, T. Olsen, M. Engelund, and J. Schiotz, Phys. Rev. B **78**, 075441 (2008).

[26] R. O. Jones and O. Gunnarsson, Rev. Mod. Phys. **61**, 689 (1989).

[27] H. Bottger and V. V. Bryksin, *Hopping Conduction in Solids* (VCH, Berlin, 1985).

[28] N. A. Deskins and M. Dupuis, J. Phys. Chem. C **113**, 346 (2009).

[29] See Supplemental Material at http://link.aps.org/supplemental/10.1103/PhysRevB.84.121203 for the characteristic parameters of the different hole transfer paths in anatase and rutile.

[30] T. Ohsaka, F. Izumi, and Y. Fujiki, J. Raman Spectrosc. **7**, 321 (1978).

[31] J. G. Trayler, H. G. Smith, R. M. Nicklow, and M. K. Wilkinson, Phys. Rev. B **3**, 3457 (1971).

[32] T. Bak, M. K. Nowotny, L. R. Sheppard, and J. Nowotny, J. Phys. Chem. C **112**, 12981 (2008).

[33] U. Balachandran and N. Eror, J. Mater. Sci. **23**, 2676 (1988).

[34] S. Nakabayashi, S. Komuro, Y. Aoyagi, and A. Kira, J. Phys. Chem. **91**, 1696 (1987).

SUPPLEMENTAL MATERIAL

The effective force constant K is calculated from $E(x, \lambda = 0) = Kx^2/2$. Then by fitting $E(x, \lambda = 1) - E(x, \lambda = 0)$ to the antibonding eigenstate of the model Hamiltonian we obtain t and V.
From these we determine: The effective mode frequencies

$$\Omega = K^{1/2}/|(\mathbf{Q_R} - \mathbf{Q_L})\mathbf{M}^{1/2}|,$$

where $\mathbf{M}$ is a diagonal matrix of atomic masses; The non-adiabatic barriers

$$E_b^{\mathrm{nad}} = V^2/2K + Kt^2/2V^2;$$

The adiabatic barriers

$$E_b^{\mathrm{ad}} = E_b^{\mathrm{nad}} - t.$$

TABLE I: Characteristic parameters for the different hole transfer paths.

		$\lvert\mathbf{R}\rvert$	$\hbar\Omega$	E_b^{nad}	E_b^{ad}	t		T=1300K		
	n	[Å]	[meV]	[eV]	[eV]	[eV]	η_1	η_2		k[s^{-1}]
					Anatase					
A	2	2.48	39	0.38	0.19	0.15	0.44	3.00	a	1.7 10^{12}
B	4	2.84	42	0.37	0.14	0.18	0.56	4.43	a	2.7 10^{12}
C	4	3.10	39	0.38	0.29	0.06	0.17	0.45	n	9.9 10^{11}
D	2	3.83	41	0.39	0.30	0.03	0.09	0.12	n	3.4 10^{11}
E	2	3.83	42	0.42	0.30	0.05	0.14	0.27	n	6.7 10^{11}
F	1	4.02	45	0.44	0.39	0.02	0.05	0.05	n	7.2 10^{10}
					Rutile					
A	1	2.57	19	0.41	0.15	0.26	0.64	17.00	a	1.3 10^{12}
B	8	2.83	23	0.42	0.14	0.28	0.67	15.99	a	1.6 10^{12}
C	2	2.98	15	0.40	0.23	0.17	0.42	8.60	a	4.6 10^{11}
D	1	3.93	16	0.40	0.29	0.10	0.27	3.13	a	3.1 10^{11}
E	1	4.06	24	0.45	0.25	0.20	0.45	7.60	a	6.3 10^{11}

Paper III

Zawadzki P., Rossmeisl J., Jacobsen K. W.; Polaronic defect states from (semi)local DFT. Application of Δ-SCF DFT to optical absorption of the V^- center in MgO. (manuscript)

Polaronic defect states from (semi)local DFT. Application of Δ-SCF DFT to optical absorption of the V^- center in MgO.

Paweł Zawadzki,[*] Jan Rossmeisl, and Karsten Wedel Jacobsen
Department of Physics,
Center for Atomic-Scale Materials Design,
Technical University of Denmark,
DK-2800 Kgs. Lyngby, Denmark

Abstract

By means of the linear expansion Δ-self consistent field density functional theory (Δ SCF DFT) we calculate defect states and optical absorption spectra of the charged Mg vacancy in MgO (V^- center). The states are localized on $M \in \{1, 2, 4, 6\}$ oxygen sites surrounding the vacancy. (Semi)-local provides the defect state energies that are burden with relative error proportional to $1/M$. Removal of this error necessary to obtain qualitatively good defect optical absorption spectra. Furthermore such correction reduces the dependence of DFT+U results on the choice of parameter U.

PACS numbers: 71.38.Ht,71.70.Ch,71.55.Ht,71.15.Mb

The small polaron concept—an electron-polarisation field quasiparticles with size comparable lattice spacing[1, 2]—has been extensively used to describe charge carriers in materials ranging from DNA[3, 4] and proteins[5], organic semiconductors for optoelectronic devises and solar cells[6], to inorganic materials such as $LiFePO_4$ for batteries[7], HfO_2 high-k dielectric oxide for metal-oxide-semiconductor field-effect transistors [8] and Fe_2O_3 [9, 10] or TiO_2[11] for photocatalysis, etc. Since the charge transport phenomena is strongly affected by small-polaron formation and it is an essential steps in many applications, a through understanding of polaronic effects is important to elucidate materials limitations and opportunities.

First principles calculations can provide an important insight into the nature of charge carries. The density functional theory (DFT) is most commonly used method as studies of polaronic systems often require simulation cells with ∼100 atoms—a size that is currently intractable by accurate wave function techniques. Applications of state of the art DFT approximations to small-polarons, however, often leads to qualitatively incorrect predictions[12–16] as the technique provides biased treatment of states with different degrees of localization [11, 17, 18].

Here we analyze the incorrect treatment of the polaronic defect states of the V^- center in MgO. The states are localized on $M \in \{1, 2, 4, 6\}$ oxygen orbitals. Approximate DFT provides defect state energies that are burden with relative error inversely proportional to M. Removal of this inconsistency is necessary for qualitatively correct descriptions of polaronic systems. We further calculate defect optical absorption spectra by means of the linear expansion Δ-SCF DFT[19, 20]. This simple extension of the convectional DFT is particularly useful to polaronic systems as it allows to form localized charge states and calculate such key parameters as electron couplings.

A V^- center in MgO is formed upon neutron or gamma irradiation[21, 22]. The defect contains a single hole localized on an oxygen p-like orbital pointing towards the vacancy and the O_h symmetry of the Mg lattice site is lowered to the C_{4v}[23]. The electronic structure of the center is most easily understood within symmetry adapted linear combinations (SALCs) of orbitals. At the O_h symmetry the six oxygen orbitals directed towards the vacancy (see

Fig.1) span A_{1g}, T_{1u} and E_g irreducible representations with basis functions:

$$\begin{aligned}
A_{1g} &= (|\gamma_0\rangle + |\gamma_1\rangle + |\gamma_2\rangle + |\gamma_3\rangle + |\gamma_4\rangle + |\gamma_5\rangle)/\sqrt{6} \\
T^1_{1u} &= (|\gamma_0\rangle - |\gamma_5\rangle)/\sqrt{2} \qquad T^2_{1u} = (|\gamma_1\rangle - |\gamma_3\rangle)/\sqrt{2} \\
T^3_{1u} &= (|\gamma_2\rangle - |\gamma_4\rangle)/\sqrt{2} \\
E^1_g &= (|\gamma_1\rangle - |\gamma_2\rangle + |\gamma_3\rangle - |\gamma_4\rangle)/\sqrt{4} \\
E^2_g &= (2|\gamma_0\rangle - |\gamma_1\rangle - |\gamma_2\rangle - |\gamma_3\rangle - |\gamma_4\rangle + 2|\gamma_5\rangle)/\sqrt{12}
\end{aligned}$$

The electronic coupling J between equatorial pairs of orbitals is 0.19 eV and is negligible for axial ones[23]. Therefore the states A_{1g}, T_{1u} and E_g have relative stabilisations of $4J$ (bonding), $0J$ (non-bonding) and $-2J$ (anti-bonding), respectively.

An electron hole present in E_g couples to $\mathcal{T}_{1u}$ asymmetric mode lowering the symmetry to C_{4v}. SALCs then take the forms:

$$\begin{aligned}
A^1_1 &= |\gamma_0\rangle \qquad A^2_1 = (|\gamma_1\rangle + |\gamma_2\rangle + |\gamma_3\rangle + |\gamma_4\rangle)/\sqrt{4} \\
A^3_1 &= |\gamma_5\rangle \qquad B_2 = (|\gamma_1\rangle - |\gamma_2\rangle + |\gamma_3\rangle - |\gamma_4\rangle)/\sqrt{4} \\
E^1 &= (|\gamma_1\rangle - |\gamma_3\rangle)/\sqrt{2} \qquad E^2 = (|\gamma_2\rangle - |\gamma_4\rangle)/\sqrt{2}
\end{aligned}$$

and the hole occupies a single p-like orbital, say γ_0 of A^1_1 state, surrounded by the deformed lattice—a bound small O$^-$ polaron is formed.

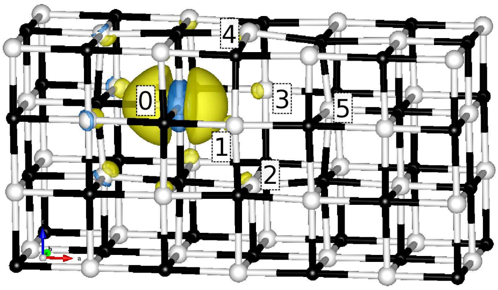

FIG. 1: A V^- center in MgO lattice; oxygen (gray), Mg (black). A single electron hole localized on the oxygen p-like orbital on site 0 induces $O_h \rightarrow C_{4v}$ distortion along 0–5 axis. The isosurface shows the electron density difference between the V^- with the hole constrained to the A^1_1 state and the V^{2-} charge states at 0.03 e/Å^{-3}; yellow and blue are hole and electron densities, respectively. The figure was drawn using VESTA [24].

To calculate the PESs for the SALCs we perform DFT calculations within the Projector Augmented Wave formalism implemented in the GPAW code[25]. Wave-functions, densities and potentials are described on a real space grid with a spacing ≈ 0.2 Å. The MgO cubic unit cell is optimized and the resulting lattice constant is 4.267Å (the experimental value is 4.212 Å). For the defect center we use a 215 atom 3x3x3 supercell for which we sample the Brillouin zone with a 2x2x2 Monkhorst-Pack mesh.

We construct SALCs by means of the linear expansion Δ-SCF[19, 20]. The method allows to subtract the electron density of the SALC expanded in KS states at each SCF cycle. The SALCs are formed from p-like orbitals defined as a difference between the true and the pseudo oxygen $1p$ orbital of the PAW formalism[11, 17, 19]. These are zero outside the sphere of radius 0.74 Å. The expansion, however, is determined by the symmetry and the nodal structure of the composite orbitals rather than their exact extent. Moreover, since the SALCs form the basis for irreducible representations of the symmetry point group of the supercell, the expansions are largely formed by a single KS state of the appropriate symmetry and the nodal structure.

We construct the PESs along the $O_h \rightarrow C_{4v}$ distortion. Since the distortion is not spontaneous in (semi)local DFT we determine it by relaxing the system with an electron hole constraint to the A_1^1 state. The structure minimizing Hellmann-Feynman forces corresponds to the minimum energy on the A_1^1 PES (see arrows tangent to the A_1^1 PES in Fig.1).

In Fig.2 we plot the non-adiabatic PESs along the $O_h \rightarrow C_{4v}$ distortion. The upper part shows results of PBE exchange-correlation (XC) [26] DFT calculations. Clearly, this (semi)local XC functional fails to predict the spontaneous distortion. The ground state is the E_g at the O_h symmetry instead of the A_1^1 at C_{4v}. Furthermore the separation between the O_h states is rather different from the expected $4J$, 0, $-2J$. The T_{1u} almost coincides with the A_{1g} whereas it should be $4J = 0.76$ eV up in energy.

Apart from these system specific inaccuracies there is an elemental error. Upon symmetry lowering the A_1^1 and A_1^3 states split from the O_h state therefore their origin must be contained between O_h states. Precisely, their energies at $\rho = 0$ should be $0J$ which is also the energy of the T_{1u} state. The origin of the A_1^1 and A_1^3, however, lays well above the O_h states—1.1 eV above the T_{1u} state.

This shift arises because of the biased treatment of states with a different degree of localization—both the A_1^1 and A_1^3 are localized on a single p-like orbital whereas states

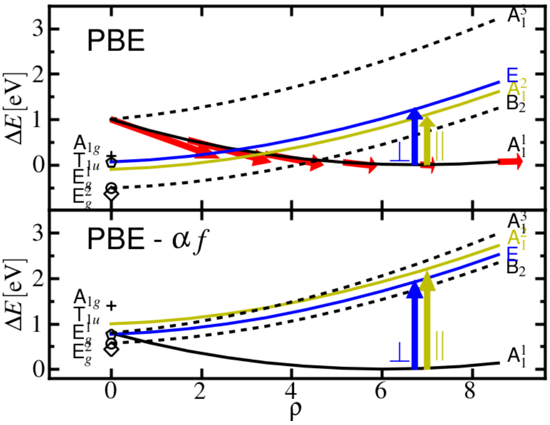

FIG. 2: The non-adiabatic potential energy surfaces (PESs) for the different symmetry states of the V^- center along the $O_h(\rho = 0) \rightarrow C_{4v}$ distortion. Top: PBE PESs not corrected for the delocalization error; Bottom: PESs corrected by removal of the energy nonlinearity αf. Full lines denote states involved in optical transitions of the center; arrows tangent to the A_1^1 are proportional to sum over Hellman-Feynman forces.

at O_h symmetry are composed of 6 (A_{1g}), 4 (T_{1u}) and 2 (E_g) orbitals. Due to the non-linearly of the total energy (semi)local DFT favours more delocalized states [11, 18, 27, 28]. If α is the quadratic energy nonlinearity of a single orbital $|\gamma_i\rangle$ then for a composite system $|\Gamma\rangle = \sum_i^M c_i|\gamma_i\rangle$ the energy nonlinearity is $\alpha f = \alpha \sum_i^M |c_i|^4$, where f is the degree of the electron localization in $|\Gamma\rangle$. For equal weights $|c_i| = 1/\sqrt{M}$ the relative error is inversely proportional to the number of orbitals contributing to the state: $f = 1/M$.

On Fig.3 we plot the energy nonlinearly for O_h and C_{4v} states. The relative error follows a $1/M$ trend and is constant along the $O_h \rightarrow C_{4v}$ distortion (see the inset plot in Fig.3) indicating that the states do not change along the distortion. The exception here is the A_1^1 state. This state is coupled to the distortion and the atomic surrounding of a single γ_0 orbital relaxes outward along the distortion. Therefore the spacial extent of this orbital becomes larger (more delocalized) hence its energy nonlinearity decreases as observed.

We remove the bias of the PESs description by subtracting the energy nonlinearity αf. The bottom part of Fig.2 shows the corrected results. Firstly, the distortion is now spontaneous and rightly the A_1^1 is the ground state. The separation between the O_h states also improves, specifically the A_{1g}^1 is 0.63 eV above the T_{1u}. Finally the correction recovers the correct

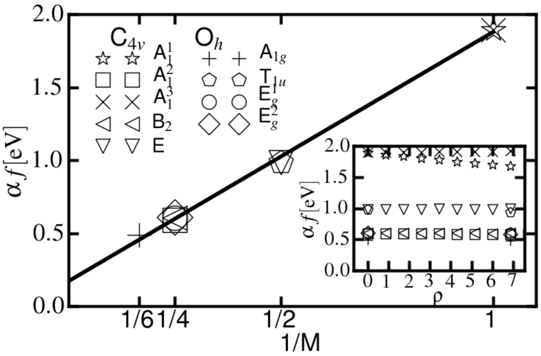

FIG. 3: The energy nonlinearity αf follows $f = 1/M$ trend; f is the degree of state localization, e.g. $f = 1/2$ for the T_{1u} as this state is localized over two orbitals. The inset plot shows the energy nonlinearity along the $O_h(\rho = 0) \rightarrow C_{4v}$ distortion.

splitting of the A_1^1 and A_1^3 states from the O_h states. A_1^1 and A_1^3 now originate at the T_{1u} state.

To further check the quality of the corrected PESs we calculate the defect absorption spectra. The experimental absorption band consists of a broad peak centered at around 2.3 eV. The low energy part of the spectra is due to $A_1^1 \rightarrow A_1^2$ and $A_1^1 \rightarrow E$ transitions; absorption at higher energies involve π states of the center[23, 29, 30]. In an electric field V^- centers align and absorption of light polarized parallel to the direction of the applied electric field peaks at 1.85eV ($A_1^1 \rightarrow A_1^2$); band due to perpendicular light polarization is located at 2.30eV ($A_1^1 \rightarrow E$)[23, 29, 30].

Assuming single effective mode model in reduced coordinates $\rho = (m\Omega/\hbar)^{1/2}q$: The initial state $I = A_1^1$ is described by a displaced harmonic oscillator $E_I(\rho) = \frac{1}{2}\hbar\Omega(\rho - s)^2$ where $s = 6.9$ is the equilibrium lattice distortion; Ω is the effective mode angular frequency (calculated $\hbar\Omega$ is 0.065 eV and agrees with Ref.[23]). The final states $F \in \{A_1^2, A_1^3, B_2, E\}$ are not coupled to the coordinate and are given by $E_F(\rho) = \frac{1}{2}\hbar\Omega\rho^2 + \Delta_{IF}$ where Δ_{IF} describes their relative shift with respect to A_1^1 (for values of Δ see Supplemental Material). The absorption cross-section per defect $\sigma(\omega)$ due to vertical transitions from vibrational states located on the E_I to states on the E_F is proportional to the shape function $G_{IF}(\omega)$ and the oscillator strength $\vec{f}_{IF}$. For large deformation $s >> 1$ the E_F can be treated

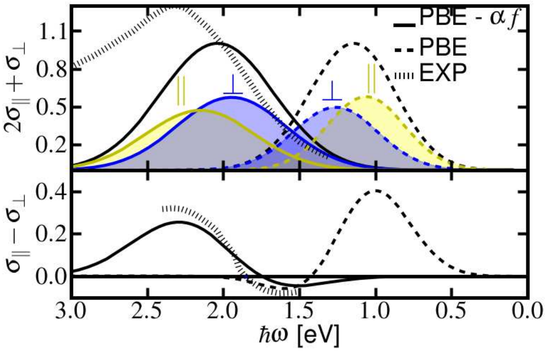

FIG. 4: Top: the optical absorption of the V^- center. Bottom: the dichroism curve. PBE results (dashed lines) fail to reproduce the experimental data [29] (dotted lines) predicting absorption peak at too low energies and providing incorrect sign of the dichroic effect. Subtraction of the energy nonlinearity αf leads to a semi-quantitative agreement (full lines).

classically and G_{IF} is a Gaussian centered at $\hbar\omega_{IF} = \hbar\Omega s^2 + \Delta_{IF}$:

$$G_{IF}(\omega) = [w(T)/\pi]^{1/2} \exp\left[(\hbar\omega - \hbar\omega_{IF})^2 w(T)\right]^{1/2} \tag{1}$$

with $w(T) = \tanh(\hbar\Omega/2kT)/(s\hbar\Omega)^2$ [23, 31]. To calculate oscillator strength $\vec{f}_{IF} = (2m_e\omega_{IF}/e^2\hbar)\vec{\mu}_{IF}^2$ we use approximate electronic transition moment $\vec{\mu}_{IF} \approx (e/\sqrt{M_F}\hbar\omega_{IF})\sum_{n\in F} J_{0n}\vec{d}_{0n}$ [30] where $\vec{d}_{0n}$ and J_{0n} are the vector connecting lattice site 0 and n and the electronic coupling between $|\gamma_0\rangle$ and $|\gamma_n\rangle$, respectively; $1/\sqrt{M_F}$ is the normalization factor of the final state F. We calculate J_{0n} as a one half of the energy difference between systems with hole constraint to the antibonding and the bonding combinations of the two orbitals: $((|\gamma_0\rangle \pm |\gamma_n\rangle)/\sqrt{2})$. For axial pairs we find 0.01 eV whereas for equatorial 0.19 eV. These values agree with Ref[23]. (For the calculated oscillator strength see Supplemental Material.)

In Fig. 4 we show calculated absorption bands. Transitions based on the corrected PES (PBE-αf) reproduce the low energy part of the experimental spectra and lead to the zero dichroism point at 1.75 eV compared to experimental value of 1.85 eV [29]. The not-corrected absorption band is off by ≈ 1.0 eV. Furthermore, semi-local DFT locates the $A_1^1 \rightarrow A_1^2$ at higher energy than the $A_1^1 \rightarrow E$ therefore predicts incorrect sign of the dichroic effect.

An extension of DFT that is often used to localize electrons or holes is DFT+U [32, 33].

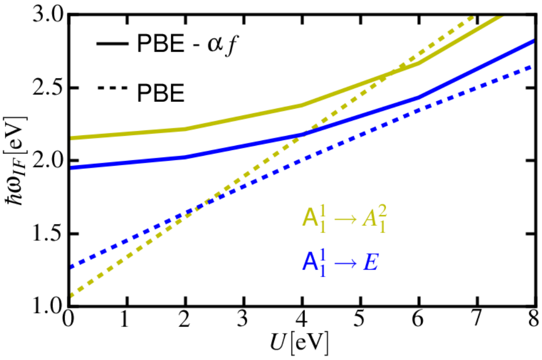

FIG. 5: Optical transition energies calculated with DFT+U (dashed lines). Removal of the total energy non-linearity (full lines) reduces the dependence of the results on the choice of parameter U.

Using rotationally invariant formulation of the method [33] we have calculated optical transitions energies for different parameters U—dashed lines on Fig. 5. Clearly, DFT+U results are strongly depended on choice of the parameter U. A simple removal of the total energy non-linearity (full lines), however, reduces this dependence. Moreover, for all U such a posteriori correction preserves the energy difference between $A_1^1 \to A_1^2$ and $A_1^1 \to E$ transitions. This energy difference equals to J and is directly related to the degree of the states localization. Thus for $U \in [0, 8]$ eV the correction removes the energetic bias in description of states with a different degree of localization.

In conclusion, we have studied the defect states of the V^- center in MgO—an example where a single hole can localized on $M \in \{1, 2, 4, 6\}$ oxygen lattice sites. We have shown that the violation of the linearity of the total energy introduces relative errors that are inversely proportional M. Removal of this error is necessary for a quantitatively good description of the defect states PESs. We have further calculated the optical absorption spectra of the V^- center by means of the linear expansion Δ-SCF. The technique is particularly useful for studies of polaronic systems as it allows to form localized charge states and to obtain such key parameters as electron couplings.

CAMD is funded by the Lundbeck foundation. The Catalysis for Sustainable Energy initiative is funded by the Danish Ministry of Science, Technology and Innovation. This work was supported by the Danish Center for Scientific Computing. Support from the

Danish Council for Technology and Innovation's FTP program and the Danish Council for Strategic Research though the HyCycle Center (No. 2104-07-0041) is acknowledged.

---

* `zawpaw@fysik.dtu.dk`

[1] T. Holstein, Ann. Phys. **8**, 343 (1959).

[2] H. Bottger and V. V. Bryksin, *Hopping Conduction in Solids* (VCH Berlin, 1985).

[3] T. Shigematsu, K. Shimotani, C. Manabe, H. Watanabe, and M. Shimizu, J. Chem. Phys. **118**, 4245 (2003).

[4] K.-H. Yoo, D. H. Ha, J.-O. Lee, J. W. Park, J. Kim, J. J. Kim, H.-Y. Lee, T. Kawai, and H. Y. Choi, Phys. Rev. Lett. **87**, 198102 (2001).

[5] M. J. Bollinger, Science **320**, 1730 (2008).

[6] T. Strobel, C. Deibel, and V. Dyakonov, Phys. Rev. Lett. **105**, 266602 (2010).

[7] T. Maxisch, F. Zhou, and G. Ceder, Phys. Rev. B **73**, 104301 (2006).

[8] D. Muñoz Ramo, A. L. Shluger, J. L. Gavartin, and G. Bersuker, Phys. Rev. Lett. **99**, 155504 (2007).

[9] P. Liao, M. C. Toroker, and E. A. Carter, Nano Lett. **11**, 1775 (2011).

[10] N. Iordanova, M. Dupuis, and K. M. Rosso, J. Chem. Phys. **122**, 144305 (2005).

[11] P. Zawadzki, J. Rossmeisl, and K. W. Jacobsen, Phys. Rev. B **84**, 121203 (2011).

[12] S. Lany and A. Zunger, Phys. Rev. B **80** (2009).

[13] S. J. Clark, J. Robertson, S. Lany, and A. Zunger, Phys. Rev. B **81** (2010).

[14] G. Pacchioni, F. Frigoli, D. Ricci, and J. Weil, Phys. Rev. B **63** (2001).

[15] W. R. L. Lambrecht, Phys. Status Solidi B **248**, 1547 (2011).

[16] J. Laegsgaard and K. Stokbro, Phys. Rev. Lett. **86**, 2834 (2001).

[17] P. Zawadzki, K. W. Jacobsen, and J. Rossmeisl, Chem. Phys. Lett. **506**, 42 (2011).

[18] P. Mori-Sánchez, A. J. Cohen, and W. Yang, Phys. Rev. Lett. **100**, 146401 (2008).

[19] J. Gavnholt, T. Olsen, M. Engelund, and J. Schiotz, Phys. Rev. B **78**, 075441 (2008).

[20] R. O. Jones and O. Gunnarsson, Rev. Mod. Phys. **61**, 689 (1989).

[21] L. E. Halliburton, D. L. Cowan, W. B. J. Blake, and J. E. Wertz, Phys. Rev. B **8**, 1610 (1973).

[22] A. Schoenberg, J. T. Suss, S. Szapiro, and Z. Luz, Phys. Rev. Lett. **27**, 1641 (1971).

[23] O. Schirmer, Z. Phys. B-Condens. Mat. **24**, 235 (1976).

[24] K. Momma and F. Izumi, J. App. Cryst. **44**, 1272 (2011).

[25] J. Enkovaara, C. Rostgaard, J. J. Mortensen, J. Chen, M. Dulak, L. Ferrighi, J. Gavnholt, C. Glinsvad, V. Haikola, H. A. Hansen, et al., J. Phys.-Condes. Matter **22**, 253202 (2010).

[26] J. P. Perdew, K. Burke, and M. Ernzerhof, Phys. Rev. Lett. **78**, 1396 (1997).

[27] J. P. Perdew, R. G. Parr, M. Levy, and J. L. Balduz, Phys. Rev. Lett. **49**, 1691 (1982).

[28] J. P. Perdew, A. Ruzsinszky, G. I. Csonka, O. A. Vydrov, G. E. Scuseria, V. N. Staroverov, and J. Tao, Phys. Rev. A **76** (2007).

[29] B. H. Rose and D. L. Cowan, Solid State Commun. **15**, 775 (1974).

[30] O. F. Schirmer, J. Phys.-Condes. Matter **18**, R667 (2006).

[31] T. Keil, Phys. Rev. **140**, A601 (1965).

[32] V. Anisimov, J. Zaanen, and O. Andersen, Phys. Rev.B **44**, 943 (1991).

[33] S. L. Dudarev, G. A. Botton, S. Y. Savrasov, C. J. Humphreys, and A. P. Sutton, Phys. Rev. B **57**, 1505 (1998).

Polaronic defect states from (semi)local DFT. Application of Δ-SCF DFT to optical absorption of the V^- center in MgO.

Paweł Zawadzki,* Jan Rossmeisl, and Karsten Wedel Jacobsen
Department of Physics,
Center for Atomic-Scale Materials Design,
Technical University of Denmark,
DK-2800 Kgs. Lyngby, Denmark

(Dated: January 6, 2012)

Supplemental Material

TABLE I: Parameters for the calculation of the optical absorption from the initial state $I = A_1^1$ to the final states F. Δ_{IF} is the vertical shift the F PES with respect to the A_1^1 PES; $\hbar\omega_{IF}$ is vertical transition energy. Superscripts denote PBE and PBE corrected for the delocaliztion error results $(\mathrm{PBE} - \alpha f)$. f_{IF} is the oscillator strength for light polarized $\parallel$ or $\perp$ to the distortion axis.

F	$\Delta_{IF}^{\mathrm{PBE}}$	$\Delta_{IF}^{\mathrm{PBE}-\alpha f}$	$\hbar\omega_{IF}^{\mathrm{PBE}}$	$\hbar\omega_{IF}^{\mathrm{PBE}-\alpha f}$	$f_{IF}^{\parallel}$	$f_{IF}^{\perp}$
A_1^3	0.00	0.00	2.57	2.33	0.000	0.000
A_1^2	-1.01	0.20	1.06	2.15	0.082	0.000
E	-0.96	0.03	1.26	1.95	0.000	0.050
B_2	-1.51	0.22	0.69	1.76	0.000	0.000

---

* zawpaw@fysik.dtu.dk

Paper IV

Zawadzki P., Jacobsen K. W., Dahl S., Rossmeisl J.; Explaining oxidative trends of TiO_2—Hole trapping at anatase and rutile surfaces. (manuscript)

Explaining oxidative trends of TiO_2—Hole trapping at anatase and rutile surfaces.

Paweł Zawadzki,[1,*] Karsten Wedel Jacobsen,[1] Søren Dahl,[2] and Jan Rossmeisl[1]

[1] *Center for Atomic-Scale Materials Design, Department of Physics,*
Technical University of Denmark, DK-2800 Kgs. Lyngby, Denmark

[2] *Center for Individual Nanoparticle Functionality, Department of Physics,*
Technical University of Denmark, DK-2800 Kgs. Lyngby, Denmark

Abstract

Photo-catalysis is presently used in a large variety of applications such as water and air purification, self-cleansing surfaces, anti-fogging coatings. Furthermore, for future sustainable fuel production from solar light efficient photo-catalysis is crucial. A successful photo-catalytic transformation of absorbed photon energy must comprise: separation of photo-generated electron-hole pairs, carrier transport to surface active sites and finally chemical reaction. Understanding the nature of charge carries involved in these steps is therefore important for the recognition of photo-catalyst limitations. In particular in a number of materials strong electron-lattice interaction leads to carrier self-trapping. The influence of charge self-trapping on photo-catalytic activity however, is unclear. Basing on density functional theory calculation we show here that for the most popular photo-catalyst, TiO_2, the electron hole self-trapping leads to states of which the position in band gap is dependent on the local electrostatic environment and thereby the type of surface termination. This finding explains previously not understood trends of rutile and anatase surfaces in photo-deposition and photo-etching reactions. Furthermore it allows us to shed light on other important issues such as synergism of rutile and anatase mixtures and generally observed higher photocatalytic activity of the anatase phase. We anticipate that our results can aid the design of more reactive photo-catalysts based on TiO_2 and our approach can be utilized for other relevant photo-catalysts as well.

Titanium dioxide is abundant, harmless, and chemically inert therefore technologically a very attractive material. This businesslike motivation has driven an extensive research on TiO_2 and especially on its photo-catalytic properties. Many aspects of TiO_2 photo-catalysis however, still remain obscure[1, 2]. Issues regarding different activities of rutile and anatase phases, surface termination dependence of oxidative properties and synergism in phase mixtures are especially important as these effects can directly be exploited in photo-catalyst design. A clear illustration of such dependencies comes from observations of PbO_2 photo-deposition rates (see Fig.1). Bae et al.[3] found that for rutile nanorods terminated by {001}, {110}, {111} planes oxidation of Pb^{2+} to PbO_2 takes place on {001} surfaces whereas reduction of $PtCl_6^{2-}$ to Pt takes place on {110} surfaces. In a similar experiment by Ohno et al. rutile {011} were more oxidative than {110} and anatase {001} were more oxidative than {011}[4]. Furthermore, in anodic photo-etching of rutile in aqueous sulfuric acid {001} and {100} planes were found the most and the least oxidative, respectively—TiO_2 dissolution ($TiO_2 + h^+ + HSO_4^- \rightarrow O_2 + TiHSO_4^{3+}$) occurs preferentially along the [001] direction and leads to formation of holes or grooves with {100} surfaces exposed[5, 6]. These experiments allow to order the surface facets by increasing oxidative properties: for rutile {100}<{110}<{011}<{001} and for anatase {011}<{001}.

A photocatalytic process relays on a sequence of a charge transport to surface reactive sites, and surface reaction steps. Depending on relative kinetics of these two steps the rate of the overall photocatalytic process can be limited by either of them. The photogenerated holes reach surface within picoseconds after the excitation [7, 8]. Many reactions, especially those involving nuclear rearrangements, occur on much longer time scales, for instance a microsecond hole transfer to to toluene or acetonitryl [9], or millisecond-second water oxidation and oxygen evolution [10]. Therefore, in those cases the population of photogenerated carries has sufficient time to attain a certain degree of thermal equilibrium, and their concentration on surfaces is determined by their stability on surface sites.

We show in the following that differences of excess surface hole density among rutile and anatase surfaces arise due to variation of spacial and energetic distribution of hole trapping states. Hole trapping states have been observed in many experiments including electron paramagnetic resonance (EPR), transient absorption spectroscopy (TAS) and photoluminesecne (PL) (for a review see Fujishima et al.[1] and Henderson[2]) but their exact nature remained unclear. Only recently it is becoming more evident that holes in TiO_2 self-trap forming O^- small polarons[11–15]—an electronic hole localized on an oxygen lattice site surrounded by a deformed lattice. The hole trapping state is formed by a *p*-like orbital perpendicular to the flat OTi_3 building blocks of TiO_2. Our DFT calculation predicted that trapping in anatase is stronger than in rutile and the small-polaron stabilisation energy with respect to the delocalized holes in the valence band (VB) is 0.2 eV; in rutile the two types of hole states have comparable stability[12]. DiValentin et al. found trapping strength of 0.75 eV in anatase[13]. Here our focus is on the effect of surface termination on the trapping strength as this issue is particularly relevant to the understanding of the TiO_2 photo-catalysis.

A surface, as any other crystal imperfection, induces lattice relaxation and charge redistribution. These processes create potential variations in surface layers. The localized nature of trapped hole states makes their energetics highly sensitive to such potential changes. Fig.2 shows a schematic energy diagram of a surface terminated semiconductor with upward bended bands. The hole trapping level ε_{T} (dashed line) is located in the band gap and in the same way as the VB and the CB edges it follows the space charge potential. At the very surface layers, however, crystal structure interruption give rise to potential variations that modify the stability of the trapped (localized) hole states.

In Fig.3 we plot the energy diagram for anatase {001} and {011} surfaces (for anatase {100} and rutile {001}, {011}, {110}, {100} see Supplementary Fig.6). The hole stabilisation energy (the trapping level) oscillates along the surface layers and converges to the bulk value within 1–2 nm. For most terminations the hole stabilisation energy is the largest at the surface oxygen bridge site. This site is doubly coordinated by Ti cations therefore a positive hole charge is less destabilized compared to OTi_3 sites. An active role of bridging oxygen sites in photo-oxidation mechanisms is also supported by isotope labeling experiments[6, 16]. For surfaces composed of charged layers, such as anatase {011} formed by $[O^{2-}(TiO)_2^{4+}O^{2-}]_n$, the energy strongly oscillates around the bulk value. For neutral layer stacking, as in case of anatase {001} composed of $[TiO_2]_n$, the trapping strength is more even and only the strengths of the surface-most trapping sites are significantly modified. Moreover, for some surfaces there are two possible hole orbital alignments with respect to the surface. For instance, for anatase {011} the lobe of the hole orbital can be parallel or nearly perpendicular to the surface (see Fig.4). In the former case the hole stability oscillates more strongly (blue circles in Fig.3(b)).

These observations suggest the electrostatic potential in the surface layers as responsible for the variation of the trapping strength. To check our presumption we construct a similar depth profile for the electrostatic energy $U(z) = \int V(\mathbf{r})n_p(\mathbf{r}-z)\mathbf{dr}$ (see the bottom plots in Fig.3) where $V(\mathbf{r})$ is the electrostatic potential, and $n_p(\mathbf{r}-z)$ is the charge density of the oxygen atomic p orbital centered at the oxygen lattice site at depth z. Similarity between $U(z)$ and $\varepsilon_{\mathrm{T}}(z)$ is clear. A stronger $U(z)$ variation in case of hole states with orbital parallel to the surface arise because of the overlap of the hole density with the electrostatic potential that vary between surface layers. Electrostatic effects also explain the instability of the hole state on rutile $\{100\}$. This surface is formed by $[\mathrm{Ti}^{4+}\ \mathrm{O}_2^{4-}]_n$ stacking (see Supplemental Fig.7 and Fig.6(a)) and the lobe of the hole orbital is immersed in the Ti^{4+} layer that destabilizes the positive hole charge. In contrast for the stable holes on $\{001\}$ rutile and anatase surfaces the hole orbital is aligned parallel to neutral layers.

A quantity directly related to the surface electrostatic potential is the work function $\phi = (\bar{V}^{\mathrm{B}} - V^{\mathrm{V}}) - \mu/e$ where the difference between the average electrostatic potential in the bulk $\bar{V}^{\mathrm{B}}$ and the reference value in the vacuum V^{V} is due to the surface dipole moment and μ is the chemical potential of the electron—a bulk property[17]. In Fig.5 we plot the trapping strength of the hole states localized on the bridging oxygen sites $\varepsilon_{\mathrm{T}}^{\mathrm{S}}$ against the work function. Intelligibly, the lower the work function the more stable the hole state is, as it is easier remove an electron. The correlation, however, is not linear as local effects are important. Nevertheless, now it is easy to see the trends in surface hole stability: for rutile $\{100\}<\{110\}<\{011\}<\{001\}$; for anatase $\{011\}<\{100\}<\{001\}$. These trends agree with experimental photo-deposition and photo-etching rates. Since surface trapping levels, with the exception of $\{100\}$ rutile, are well above the VB edge the surface hole distribution will be dominated by the trapped rather than the VB holes. Therefore if photo-generated holes are in equilibrium between themselves the trend in hole stability will translate into the surface hole density. For instance hole stability of 1.1 eV on anatase $\{001\}$ with respect to the bulk value will enhance the equilibrium surface hole density by $p^{\mathrm{S}}/p^{\mathrm{B}} = \exp\left[(\varepsilon_{\mathrm{T}}^{\mathrm{S}} - \varepsilon_{\mathrm{T}}^{\mathrm{B}})/k_B T\right] \approx 10^{20}$ at room temperature. In a non-equilibrium situation such an enormous factor provides large driving force for hole transport to the surface and enhances electron-hole separation necessary for obtaining any photo-catalytic effect. An increase in O^- concentration with increasing $\{001\}$ surface area has been observed in EPR experiment by D'Arienzo et al. and correlated with stronger photo-catalytic activity[14].

A higher hole stabilisation on most abundant anatase {110} and{100} compared to rutile {110} surfaces also reflects the fact that anatase is generally more photo-catalytically active. For most reactions self-trapped holes at surface should be sufficiently oxidative as the VB edge in TiO_2 lays quite high on the electrochemical scale (3.0 V [NHE])[1]. For instance hole stabilization on anatase {001} of 1.3 eV reduces oxidative power to ca. 1.7 V [NHE] while for instance $E^0_{\mathrm{PbO_2/Pb^{+2}}} = 1.46$ V [NHE]. For trapped hole states in anatase Lawless et al.[18] and Tojo et al.[19] reported oxidation potentials of ca. 1.5-1.7 V [NHE] from pulse raiolysis and flash photolyis experiments, respectively. Bahnemann et al. found two types of trapped states: a deeply trapped holes at ca. 1.5 V [NHE] not reacting with dichloroacetate and thiocyanate; and reactive shallowly trapped holes at higher redox potentials[7].

Further support for the surface hole self-trapping comes from observations of shifts of the flat band potential upon light irradiation. Hagfeldt et al.[20] compared Mott-Schottky plots for TiO_2 nanocrystaline films under dark and UV-light conditions. Irradiated films showed larger capacitance and the response shifted anodicaly indicating presence of high density surface hole states. Since the self-trapping centers are associated with the oxygen lattice sites high density of trapping states is possible and can arise at strong UV illumination. Such high density of photo-generated surface hole states could also explain a dramatic improvement of Dye-Sensitized solar cell performance when exposed to UV light[21, 22]. Electrostatic field induced by the positive surface hole charge will decrease the Schottky barrier at the metal/TiO_2 contact and therefore facilitate electron transfer.

Self-trapping is especially important for nano-sized TiO_2 particles. There the band bending do not develop fully and the facial dependence of trapping strength can be the only driving force for charge separation. Under a typical donor density $N_d = 10^{17}$ cm^{-3} in TiO_2 for particle size of 20nm the potential drop across space charge layer is of the order of thermal energy[23] thus irrelevant. Phase and morphology dependent hole self-trapping strengths will also enhance charge separation in mixtures. Such effect has been observed, in particular for Degussa P25[24, 25], and attributed to charge transfer between the two TiO_2 phases[25, 26]. But, there is no consensus on the direction of such transfer. A simple consideration of the positions of the VB and the CB edges or the averaged work function[27, 28] is not sufficient and the morphology dependent positions of surface hole (and electron) states has to be taken into account.

In conclusion, we have shown that the position of the hole trapping states in the band gap vary among rutile and anatase facets. Differences in the hole trapping strengths provide a driving force for electron-hole separation and lead to the variation in facets activity toward oxidation processes. We think that this understanding could help to design more efficient photo-catalyst for instance by depositing an oxidation catalyst on an appropriate surface[29] or by tuning a nano-particle shape for a better charge separation step.

METHOD

We performed DFT calculations within the Projector-Augmented Wave formalism implemented in the GPAW code. Pseudo wave-functions, densities and potentials were represented on a uniform, real-space grid with a spacing of 0.2Å. To account for exchange-correlation effects we chose RPBE functional. Brillouin zone was sampled with a Monkhorst-Pack mesh ensuring that $ka \geq 18$ Å where k is number of sampling points and a is a periodicity in any direction.

We optimized lattice parameters of rutile (P4_2/mnm) and anatase (I4_1/amd) TiO_2 (rutile: a=4.691, c=2.975, u=0.3061; anatase: a=3.829, c=9.744, u=0.2062). Calculations were performed for supercells defined through tetragonal lattice vectors, $[\mathbf{a}, \mathbf{b}, \mathbf{c}]$, of the respective crystallographic cells: For rutile {001}, {011}, {110}, {100} surfaces we used $[\mathbf{a}-\mathbf{b}, \mathbf{a}+\mathbf{b}, 8\mathbf{c}]$, $[-\mathbf{b}+\mathbf{c}, +\mathbf{a}, 4\mathbf{b}+4\mathbf{c})]$, $[2\mathbf{c}, \mathbf{a}-\mathbf{b}, 4(\mathbf{a}+\mathbf{b})]$, $[\mathbf{b}, 2\mathbf{c}, 5\mathbf{a}]$, respectively; For anatase {001}, {100}, {101} we used: $[2\mathbf{a}, 2\mathbf{b}, 2\mathbf{c}]$, $[2\mathbf{b}, \mathbf{c}, 4\mathbf{a}]$, $[-\mathbf{a}+\mathbf{c}, -2\mathbf{b}, 3\mathbf{a}+3\mathbf{c}]$, respectively.

To create an electron hole state we employed linear expansion Δ-self consistent field (Δ−SCF). The method allows to add/subtract the electron density of the specified orbital at each SCF cycle. The hole state was generated by removing the electron density of the oxygen p-like orbital perpendicular to C_{2v} symmetric TiO_3 unit and placing it in the bottom of the CB. With such a constraint on the electronic structure we relaxed the atomic coordinates keeping one bottom layer of the slab fixed.

Convergence of the energy and the maximum force of 0.05 eV/Å was achieved in most cases. In some, however, the hole is unstable and the above convergence criterion has not been attained therefore there we report local minima. These does not change the overall picture as unstable states to not trap holes. Supplemental Fig. 9 shows that change in unit cell size have minor effect on the hole stabilisation depth profile.

Work function has been calculated as a difference between the vacuum potential and the Fermi level of a symmetric slab (both surfaces relaxed). Supplemental Fig. 10 shows convergence of the work function with respect to the slab thickness.

---

* `zawpaw@fysik.dtu.dk`

[1] A. Fujishima, X. Zhang, and D. A. Tryk, Surf. Sci. Rep. **63**, 515 (2008).

[2] M. A. Henderson, Surf. Sci. Rep. **66**, 185 (2011).

[3] E. Bae and T. Ohno, Appl. Catal. B: Environ. **91**, 634 (2009).

[4] T. Ohno, K. Sarukawa, and M. Matsumura, New J. Chem. **26**, 1167 (2002).

[5] T. Kisumi, A. Tsujiko, K. Murakoshi, and Y. Nakato, J. Electroanal. Chem. **545**, 99 (2003).

[6] P. Salvador, Prog. Surf. Sci. **86**, 41 (2011).

[7] D. Bahnemann, M. Hilgendorff, and R. Memming, J. Phys. Chem. B **101**, 4265 (1997).

[8] Y. Tamaki, A. Furube, M. Murai, K. Hara, R. Katoh, and M. Tachiya, J. Am. Chem. Soc. **128**, 416 (2006).

[9] M. Murai, Y. Tamaki, A. Furube, K. Hara, and R. Katoh, Catal. Today **120**, 214 (2007).

[10] J. Tang, J. R. Durrant, and D. R. Klug, J. Am. Chem. Soc. **130**, 13885 (2008).

[11] S. Yang, A. T. Brant, and L. E. Halliburton, Phys. Rev. B **82**, 035209 (2010).

[12] P. Zawadzki, K. W. Jacobsen, and J. Rossmeisl, Chem. Phys. Lett. **506**, 42 (2011).

[13] C. Di Valentin and A. Selloni, J. Phys. Chem. Lett. **2**, 2223 (2011).

[14] M. D'Arienzo, J. Carbajo, A. Bahamonde, M. Crippa, S. Polizzi, R. Scotti, L. Wahba, and F. Morazzoni, J. Am. Chem. Soc. **0**, null (0).

[15] P. Zawadzki, J. Rossmeisl, and K. W. Jacobsen, Phys. Rev. B **84**, 121203 (2011).

[16] P. Salvador, J. Phys. Chem. C **111**, 17038 (2007).

[17] H. Reiss, J. Phys. Chem. **89**, 3783 (1985).

[18] D. Lawless, N. Serpone, and D. Meisel, J. Phys. Chem. **95**, 5166 (1991).

[19] S. Tojo, T. Tachikawa, M. Fujitsuka, and T. Majima, Phys. Chem. Chem. Phys. **6**, 960 (2004).

[20] A. Hagfeldt, U. Bjorksten, and M. Gratzel, J. Phys. Chem. **100**, 8045 (1996).

[21] H. J. Snaith and M. Gratzel, Adv. Mat. **18**, 1910+ (2006).

[22] B. Gregg, S. Chen, and S. Ferrere, J. Phys. Chem. B **107**, 3019 (2003).

[23] J. Bisquert, G. Garcia-Belmonte, and F. Fabregat-Santiago, J. Solid State Electrochem. **3**, 337 (1999).

[24] Y. K. Kho, A. Iwase, W. Y. Teoh, L. Maedler, A. Kudo, and R. Amal, J. Phys. Chem. C **114**, 2821 (2010).

[25] D. Hurum, A. Agrios, K. Gray, T. Rajh, and M. Thurnauer, J. Phys. Chem. B **107**, 4545 (2003).

[26] F. J. Knorr, C. C. Mercado, and J. L. McHale, J. Phys. Chem. C **112**, 12786 (2008).

[27] T. Kawahara, Y. Konishi, H. Tada, N. Tohge, J. Nishii, and S. Ito, Angew. Chem. Int. Ed.

41, 2811+ (2002).

[28] X. Zhang, Y. Lin, D. He, J. Zhang, Z. Fan, and T. Xie, Chem. Phys. Lett. **504**, 71 (2011).

[29] E. Borgarello, J. Kiwi, E. Pelizzetti, M. Visca, and M. Gratzel, Nature **289**, 158 (1981).

FIGURES

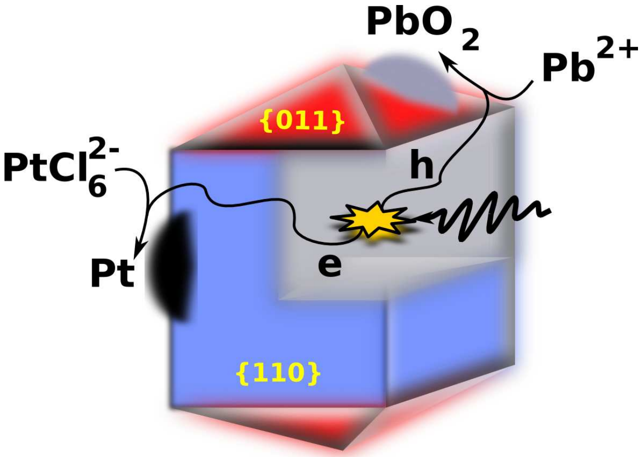

FIG. 1: Schematic photo deposition experiment performed by Ohno et al.[4]. Different rutile facets have different photo-catalytic activity towards reduction and oxidation reactions— Pb^{2+} oxidation and deposition of PbO_2 occurs on rutile {011}; reduction of $PtCl_6^{2-}$ and Pt deposition occures on {110}.

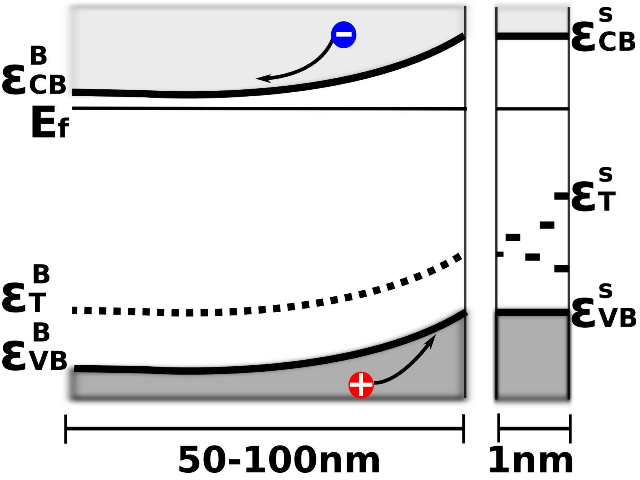

FIG. 2: Energy diagram for a n-type semiconductor with upward band banding. Hole self-trapping energies ε_{T} are sensitive to potential variation in surface layers of ≈1 nm in thickens. $\varepsilon_{\mathrm{CB}}$ and $\varepsilon_{\mathrm{VB}}$ are the valence band and the conduction band edges, respectively; superscripts S and B denote surface and bulk values, respectively.

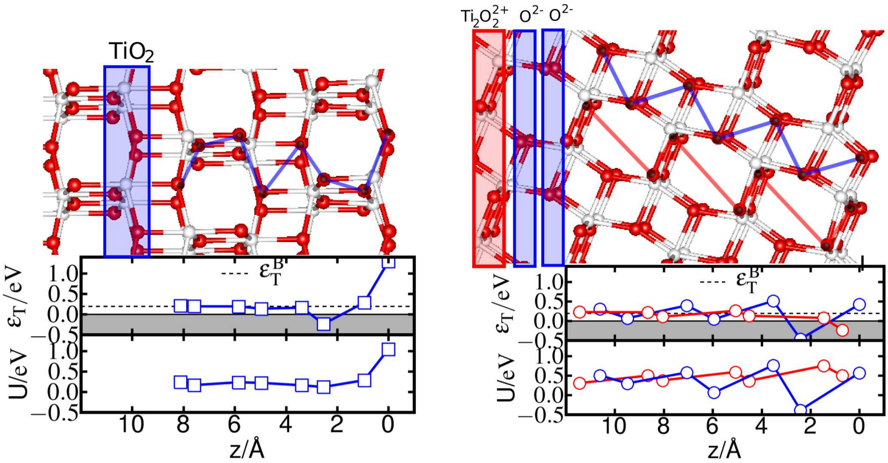

(a){001}

(b){011}

FIG. 3: Self trapping energies $\varepsilon_{\rm T}$ with respect to the valence band edge for anatase anatase {001} and {011} surfaces. In surface layers hole stabilisation energies oscillate and within 1-2 nm below the surface the profiles converge to the bulk value $\varepsilon_{\rm T}^{\rm B}$. Larger surface hole strapping strength on {001} facets explains their stronger oxidative reactivity compared. $U(z)$ is the overlap of the electrostatic potential $V(\mathbf{r})$ and the density of the hole orbital $n_p(\mathbf{r}-z)$ centered at depth z. Similarity between $U(z)$ and $\varepsilon_{\rm T}$ suggest that variation of trapping strength in surface layers is an electrostatic effect. The shaded area denotes the valence band.

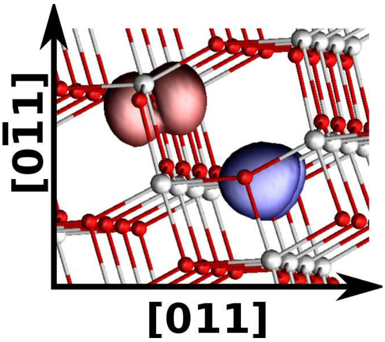

FIG. 4: Two possible p-like orbital alignments along [011] direction in anatase.

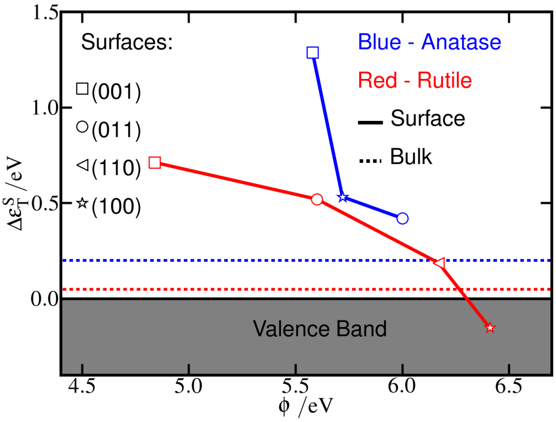

FIG. 5: Correlation between the work functions ϕ and the stabilities of the self-trapped holes ε_{T} for the different rutile and anatase surfaces. Shaded area denotes the Valence Band whereas dashed lines are the bulk self-trapping strengths $\varepsilon_{\mathrm{T}}^{\mathrm{B}}$.

SUPPLEMENTAL MATERIAL

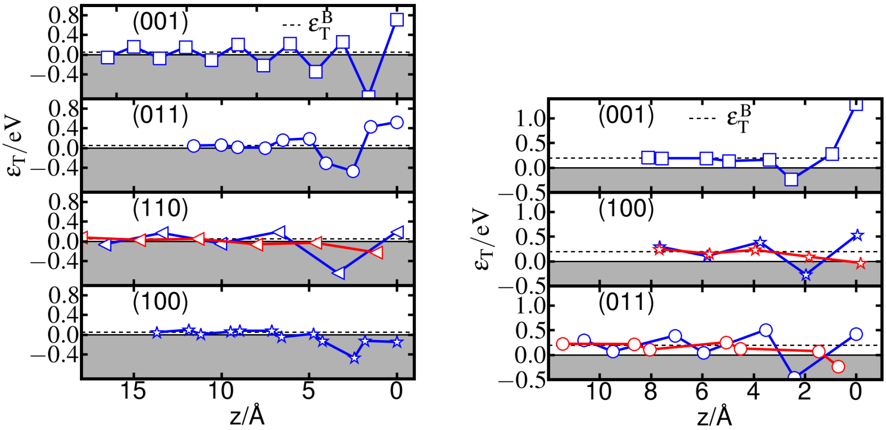

(a)rutile

(b)anatase

FIG. 6: Self trapping energies ε_T with respect to the valence band edge for rutile and anatase surfaces. In surface layers hole stabilisation energies oscillate and within 1-2 nm below the surface the profiles converge to the bulk value ε_T^B. Larger surface hole trapping strengths in anatase reflects its generally stronger oxidative activity. The shaded area denotes the valence band.

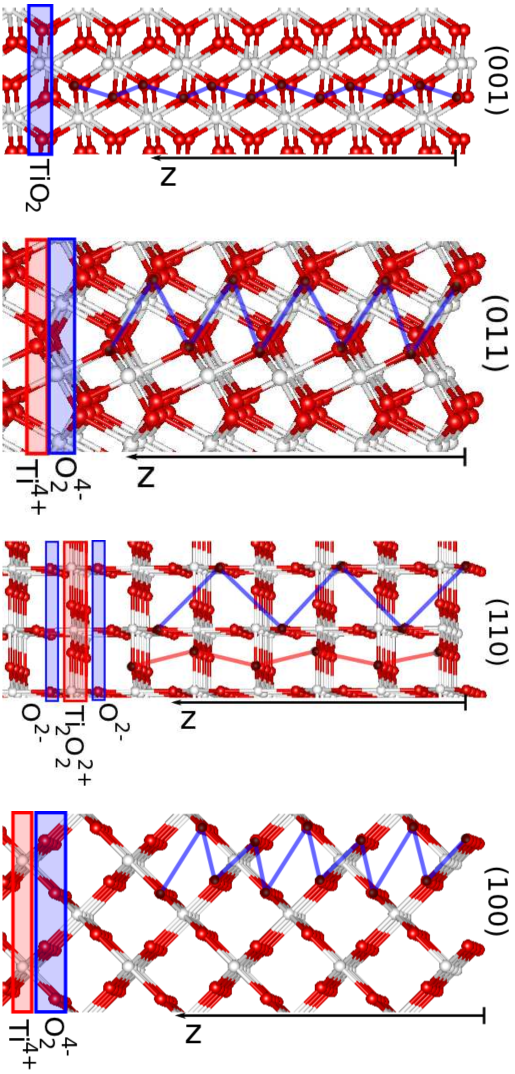

FIG. 7: Rutile surfaces. Blue and red lines link the hole trapping sites for which the hole stabilisation energies are plotted on Fig.6.

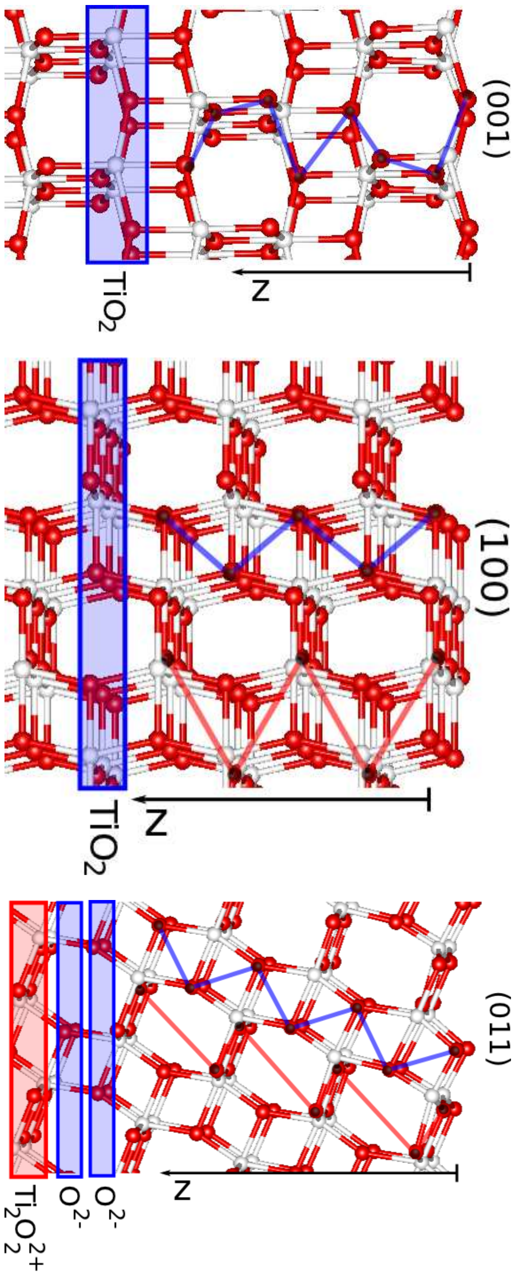

FIG. 8: Rutile surfaces. Blue and red lines link the hole trapping sites for which the hole stabilisation energies are plotted on Fig.6.

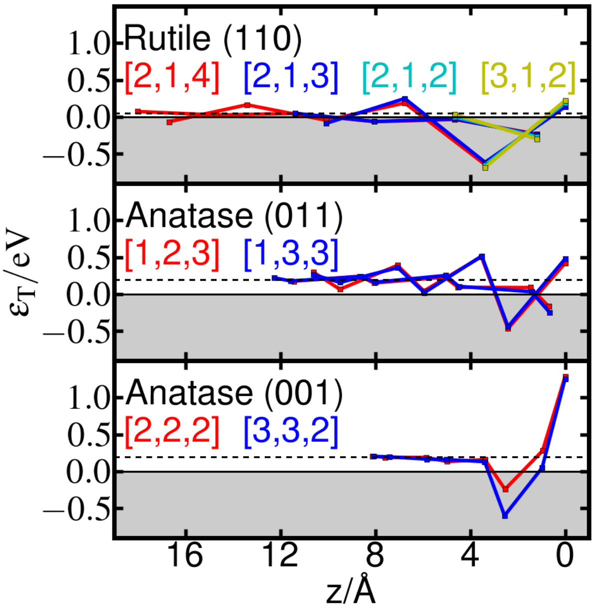

FIG. 9: Hole stabilisation calculated with different cell sizes.

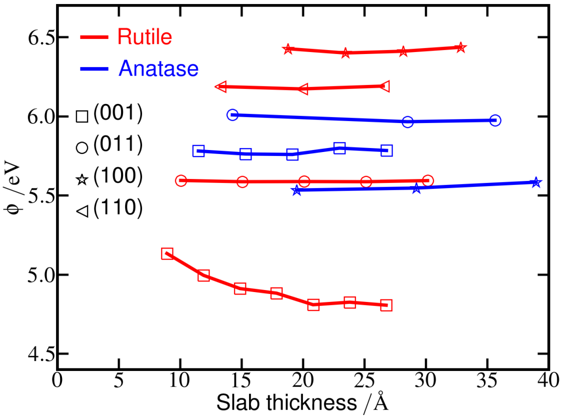

FIG. 10: Convergence of the work function with slab thickness.

Paper V

Zawadzki P.; Transient absorption spectra of anatase TiO_2. (manuscript)

Transient absorption spectra of anatase TiO_2

Paweł Zawadzki*

Department of Physics,

Center for Atomic-Scale Materials Design,

Technical University of Denmark,

DK-2800 Kgs. Lyngby, Denmark

(Dated: January 9, 2012)

Abstract

We have performed density functional theory calculations of optical charge transfer transitions of small polaron O^- centers in the anatase TiO_2 and assigned the experimentally observed trapped hole absorption range of 430-550 nm to stable surface and subsurface O^- centers. Furthermore, since bulk centers absorb at 600-750 nm, subsurface centers at 430-600 nm, whereas surface centers at > 450 nm, we link a blue shift of the spectra after excitation to holes transfer toward surface layers.

I. INTRODUCTION

Understanding charge carriers dynamics in a photoexcited semiconductor photocatalyst is critical for elucidation of factors limiting a photocatalyst performance. Semiconductor photocatalysis comprises several consecutive steps. The process begins with photogeneration of electron-hole pairs, then is followed by charge separation and transport to surface reactive sites, where finally chemical transformations occur. Studies of this dynamics require ultrafast techniques [1]. Transient absorption spectroscopy (TAS) is a technique that allows to monitor photogenerated carriers on a sub-picosecond time scale [1, 2]. The method employs a short femtosecond laser pules (pump) to photoexcite a semiconductor and then a second pules (probe) to measure time resolved absorption spectra.

TAS has been extensively used to study charge carrier dynamics in the most popular photocatalyst—anatase titanium dioxide. The TAS spectra of TiO_2 consist of free and trapped carriers contributions. The former can be explained with Drude-Lorentz model and follows λ^n power law [3]. The latter is a broad feature located in the visible spectral range, but the optical transitions behind this contribution are unclear [4–9, 9, 10].

Particularly important is elucidation of optical transitions involving trapped holes as these carriers are predominately trapped [9] and TAS could help to elucidate the effects of charge trapping photocatalyst performance. Deriving such an insight from TAS spectra, however, requires at least knowledge of spacial and energetic distribution of hole trapping sites, and optical transitions energies associated with these centers.

The first two issues, only recently are becoming more clear. An electron hole in TiO_2 self-traps on the oxygen p-like orbital perpendicular to the OTi_3 building block of the anatase and rutile structures [11–13]—an O^- small polarons is formed. Trapping strengths oscillate in surface layers and within 1-2 nm below surfaces converge to the bulk value [14].

Here, we analyze optical transition energies of O^- centers. By means of the linear expansion Δ self-consistent field (Δ-SCF) DFT [15] we calculate optical charge transfer transitions for hole trapping sites in anatase bulk and in surface layers of the (101) and the (001) facades. The obtained bands explain experimentally observed strong optical absorption of photogenerated holes in TiO_2 at 430-520 nm [4–9, 9, 10] and a blue shift of the spectra within picoseconds after excitation [4, 4–7, 16–18].

II. MODEL

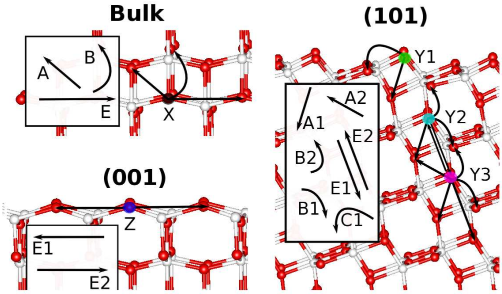

FIG. 1: Location of trapping centers $X, Y1, Y2, Y3, Z$. Arrows indicate the strongest transitions (oscillator strength $f > 10^{-3}$). Letters $A - E$ denote distinct charge transfer paths in the anatase bulk[19], and accompanied numbers denote nonequivalence of paths in surface layers.

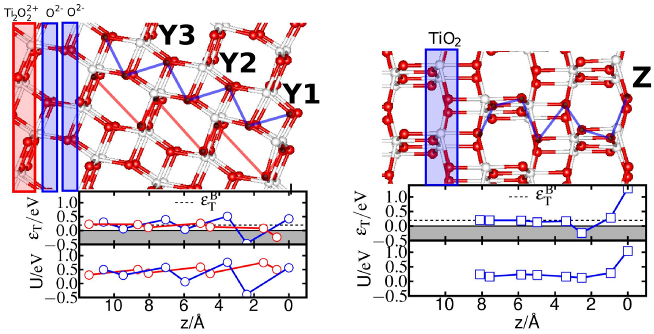

(a){101}

(b){001}

FIG. 2: Self trapping energies ε_T with respect to the valence band edge for anatase anatase {001} and {101} surfaces [14]. In surface layers hole stabilisation energies oscillate and within 1-2 nm below the surface the profiles converge to the bulk value $\varepsilon_\mathrm{T}^\mathrm{B}$. $U(z)$ is the electrostatic interaction energy of the electron density of the hole trapped at z with the surface electrostatic potential. Similarity between $U(z)$ and ε_T suggest that variation of trapping strength in surface layers is an electrostatic effect. The shaded area denotes the valence band.

A small polaron refers to a carrier localized on a single lattice site together with a surrounding lattice deformation. An optical charge transfer from one such center, I, to another, F, is often termed as an interpolaron transition [20]. On Fig.1 we illustrate this concept with a single effective mode, two site model. Potential energy surfaces (PESs) for a small polaron state localized on sites I and F are $E_I(\rho) = \frac{1}{2}\hbar\Omega(\rho+s/2)^2 - \Delta_{IF}$, and $E_F(\rho) = \frac{1}{2}\hbar\Omega(\rho-s/2)^2$, respectively, where we use reduced coordinates $\rho = (m\Omega/\hbar)^{1/2}q$. s is lattice distortion due to the electron-lattice interaction whereas Δ_{IF} describes relative bias toward charge localization on the site I. The interpolaron absorption band is due to optical transitions from the vibrational states located on E_I to the vibrational states located on E_F. For large relative PES displacement, $s >> 1$, the E_F can be treated classically and the band shape G_{IF} is a Gaussian centered at $\hbar\omega_{IF}$ [21]:

$$G_{IF}(\omega) = [w_{IF}/\pi]^{1/2} \exp\left[(\hbar\omega - \hbar\omega_{IF})^2 w_{IF}\right]^{1/2}, \tag{1}$$

with $w_{IF}(T) = \tanh(\hbar\Omega/2kT)/(s\hbar\Omega)^2$ and

$$\hbar\omega_{IF} = \hbar\Omega s^2 + \Delta_{IF}. \tag{2}$$

The absorption band of a single a small polaron center at I is a sum over possible charge transfer paths F weighted by their oscillator strength:

$$f_{IF}(E) = \frac{2m_e\omega_{IF}}{3\hbar}|\mu_{IF}|^2. \tag{3}$$

The electronic transition moment between states $|I\rangle$ and $|F\rangle$, $|\mu_{IF}| = |\langle I|(-e\mathbf{r})|F\rangle|$, can be approximated in a first order by [20]

$$|\mu_{IF}| \approx \frac{et_{IF}d_{IF}}{\hbar\omega_{IF}}, \tag{4}$$

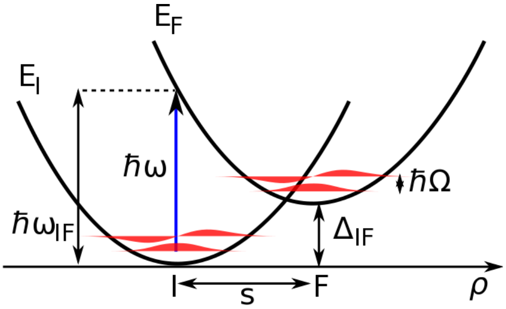

FIG. 3: Schematic energy diagram for charge transfer transition. Initial and final states $|I\rangle$ and $|F\rangle$ are associated with a localized charge on site I and F, respectively. Δ_{IF} is the relative shift of the initial and the final potential energy surfaces, E_I and E_F; ρ is lattice coordinate; $\hbar\Omega$ is the quantum of vibrational energy.

where d_{IF} and t_{IF} are the distance and the electronic coupling element, respectively, between sites I and F.

III. METHOD

Interpolaron transitions can originate from bulk and surface trapping sites. In the anatase bulk, all oxygen lattice sites are equivalent therefore it is sufficient to consider transitions from one trapping site $I = X$ to its surrounding $F = A, B, ...$ (see Fig. 1). Anatase has several stable surface terminations and each surface layer contains up to two nonequivalent oxygen lattice sites. Therefore, due to large number of possible transitions, we limit our analysis to the most stable and often reported as photocatalytically the most active, the (101) and (001) anatase facades, respectively. For the (101) surface we consider three most stable hole trapping sites $Y1, Y2, Y3$ located 0.48 eV, 0.52 eV, 0.36 eV above the valence band edge, respectively [14] (see Fig. 2(a) and Fig. 1). For the (001) surface we consider only transitions from the most stable trapping site Z, located 1.29 eV above the valence band edge [14] as subsurface centers are much less stable (see Fig. 2(b) and Fig. 1).

To calculate optical transition parameters we employ Δ-SCF DFT [15]. This simple extension of the conventional DFT allows to calculate the total energy of a system with a constrained electron density. We form an O^- center by removing the electron density of the oxygen p orbital expanded in Kohn-Sham states from the total electron density, for details see Ref. [11, 19]. The system is kept neutral by adding an electron to the bottom of the conduction band.

The transition energy $\hbar\omega_{IF}$ is obtained as the energy difference between systems with an electron hole confined to I site and to F site at the equilibrium distortion associated with the site I (ρ_I): $\hbar\omega_{IF} = E_F(\rho_I) - E_I(\rho_I)$.

The relative shift of PESs Δ_{IF} is the energy difference between states $|I\rangle$ and $|F\rangle$ calculated at their equilibrium distortions ρ_I and ρ_F, respectively, and equals to trapping strength difference between sites I and F:

$$\Delta_{IF} = E_I(\rho_I) - E_F(\rho_F) = \varepsilon_T(I) - \varepsilon_T(R). \tag{5}$$

where $\varepsilon_T(I)$ and $\varepsilon_T(F)$ are the trapping strengths (see Fig. 2 for trapping strengths profiles). To obtain the electron coupling t_{IF} we construct a bonding and an antibonding combinations of hole orbitals ($|+\rangle = (|I\rangle + |F\rangle)/\sqrt{2}$ and $|-\rangle = (|I\rangle - |F\rangle)/\sqrt{2}$), and calculate energy gap between systems with the hole density confided to these states at non-distorted structure: $t_{IF} = |E_{+}(0) - E_{-}(0)|/2$.

We have applied a similar procedure to calculate optical charge transfer transitions of the V^{-} center in MgO. After correction for the delocaliztion error the results were in good agreement with the experimental data [22]. Here the situations is simpler as the initial and final states have the same degree of localization—they are localized on a single site—thus no delocaliztion error correction is needed.

We perform RPBE DFT[23] calculations within the Projector Augmented Wave formalism implemented in the GPAW code[24]. The wave-functions/densities and potentials are described on a grid with a spacing of 0.2 Å. Atomic structures are defined by lattice vectors: $\vec{a'} = 3\vec{a}$, $\vec{b'} = 3\vec{b}$, $\vec{c'} = 2\vec{c}$ for the bulk and for the (001) surface, and $\vec{a'} = (-\vec{a} + \vec{c})$, $\vec{b'} = -3\vec{b}$, $\vec{c'} = 3(\vec{a} + \vec{c})$ for the (101) surface; $\vec{a}$, $\vec{b}$, $\vec{c}$ being the vectors of the respective tetragonal crystallographic cells. The lattice constants are optimized: $|\vec{a}| = |\vec{b}| = 3.829$, $|\vec{c}| = 9.744$ [11]. For surface slabs no periodic boundary condition in the direction normal to the surface, and a vacuum layer of 5Å were applied. During geometry optimization two bottom layers of the slabs were kept fixed. All cells contain 216 atom and the Brillouin zone is sampled on a 2x2x1 Monkhorst-Pack mesh.

IV. RESULTS

In Tab. I we present characteristics parameters of the strongest ($f > 10^{-3}$) interpolaron transitions. Transfers of type A and B dominate the absorption of the bulk (X) and the (101) surface centers ($Y1, Y2, Y3$). A and B are not possible for the Z trapping center due to specificity of the anatase (001) surface termination. Transitions energies are most easily analyzed with Eq. 2. For the (101) surface hole stability oscillates in surface layers and converges to the bulk value at larger depths (see Fig. 2(a)). Therefore Δ_{IF} will gradually decay to zero as we move from the surface to the bulk trapping centers. Transitions from deeper surface layers of the (101) surface will therefore be positioned between the $Y3$ surface and the X bulk transitions. Subsurface trapping sites in the (001) surface layers are much less stable than the surface center Z, therefore no significant occupation is expected at any time after the photo excitation. Furthermore, the trapping strength for this facade only

TABLE I: Parameters for the strongest (oscillator strength $f > 10^{-3}$) charge transfer optical transitions from sites $I \in X, Y1, Y2, Z$ to neighboring sites F. n_F denotes number of equivalent sites F; d_{IF} is the distance between I and F; $\hbar\omega_{IF}$ is the transitions energy; Δ_{IF} is the relative displacement of the potential energy surfaces E_I and E_F; t_{IF} is the electronic coupling and f_{IF} is the oscillator.

R	n_F	d_{IF} [Å]	$\hbar\omega_{IF}$ [eV]	Δ_{IF} [eV]	t_{IF} [eV]	f_{IF}
X						
A	2	2.81	1.96	0.00	0.41	3.8e-01
B	4	2.56	1.85	0.00	0.29	1.7e-01
E	2	3.88	2.53	0.00	0.11	4.5e-02
Y1						
A1	1	2.62	3.11	0.92	0.32	1.3e-01
C1	2	3.01	3.04	0.72	0.04	2.7e-03
Y2						
A1	1	2.63	2.70	0.50	0.32	1.5e-01
B1	2	2.85	2.61	0.26	0.21	7.7e-02
B2	2	2.81	2.67	0.45	0.16	4.4e-02
E1	1	3.96	3.08	0.16	0.09	2.4e-02
Y3						
A1	1	2.48	2.52	0.34	0.30	1.2e-01
A2	1	2.49	2.35	0.20	0.32	1.6e-01
B1	2	2.84	2.40	0.11	0.19	6.8e-02
B2	2	2.84	2.50	0.12	0.20	7.2e-02
E1	1	3.85	2.78	-0.16	0.09	2.6e-02
E2	1	3.81	2.95	0.10	0.10	3.1e-02
Z						
E1	1	4.80	3.74	0.00	0.04	5.0e-03
E2	1	3.26	3.15	0.00	0.04	2.7e-03

weakly oscillates in surface layers (see Fig. 2(b)) therefore transition energies from subsurface sites will be close to those originating from the bulk.

In Fig. 4 we show absorption bands for X, $Y1$, $Y2$, $Y3$, and Z centers calculated at $T = 300$ K and $\hbar\Omega = 40$ meV [19]. Bulk centers absorb at 600-750 nm, subsurface sites at 430-600 nm, whereas surface centers at >450 nm.

V. DISCUSSION

Charge transfer transitions energies (Eq. 2) are strongly dependent on a relative difference of charge trapping strengths between the initial and final states (Δ_{IF}). The hole trapping strength profiles oscillate in surface layers, and are dependent on the type of surface termination. This explains experimentally observed sensitivity of TAS spectra to TiO_2 morphology [16].

The time evolution of TAS spectra of photoexcited TiO_2 is characterised by several time scales. After excitation holes trap within 50-200 fs [4, 16, 25, 26]. The absorption spectra then blue shifts within 1-3 ps to 550 nm [4, 5, 16, 18] and then to 450 nm within the next 20-100 ps [4–7, 17]. The shape then remains unchanged on a nanosecond time scale [4–8, 17, 27]. Basing on the calculated optical transition energies, these spectral changes can be attributed to hole transfer toward surfaces. On a femtosecond time scale the transfer is likely due to hot holes as the trapping time increases for higher energy pump photons. The change of the spectra within 1-3 ps may be linked to hole transport after the trapping and the 550 nm spectra range corresponds to subsurface trapping sites (below $Y2$ or Z). This fast change, however, can not be explained with the hopping mechanism as a single hop would take a similar time. For a barrier height $E_b = 0.1$ eV and an effective mode quantum $\hbar\Omega = 40$ meV [19] a single hop at $T = 300$ K occurs on average every $\tau \approx (2\pi/\Omega)\exp(E_b/kT) = 8$ ps. Since the hopping mechanism also underestimates high temperature hole hopping mobility [19], we suggest that thermally excited to the valence band holes contribute to hole transport mechanism. Spectral changes on 20-100 ps time scale are likely due to hopping transport of deeply trapped holes in surface layers.

By scavenging one of the carriers, the absorption of trapped holes has been attributed to 430-550 nm range of TAS spectra[4–7, 17]. This part of the spectra corresponds to the interpolaronic transitions from the surface and the immediate subsurface centers—the most

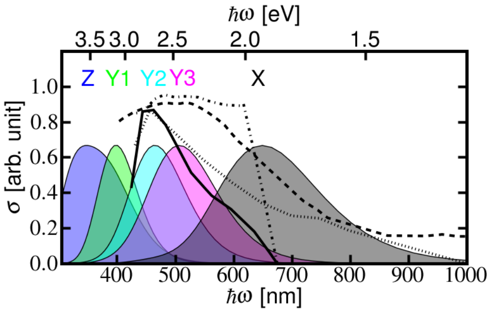

FIG. 4: Optical absorption spectra of the self-trapped hole in anatase TiO_2. Absorption bands from the $X, Y1, Y2, Y3, Z$ trapping centers (see Fig. 1) are marked by colored peaks. Experimental hole absorption spectra are marked with lines—full: 20 nm TiO_2 (hole scavenged by CD_3OD) time resolution 50 ns [9]; dashed: 2.4 nm TiO_2 (electron scavenged by Pt(1%)) measured after 5 μs [30]; dash-dotted: 2.4 nm TiO_2 (electron scavenged by Pt(1%)) measured after 20 ns [30]; dotted: 15 nm TiO_2 (electrons scavenged by Pt(1.4%)), measured after 20 μs [10].

stable hole trapping sites. Furthermore, the tail of the hole absorption band extends to long wavelengths (see Fig. 4) therefore subsurface trapping is evident and may limit hole availability for photooxidation reactions. Since the stability of surface and subsurface sites is comparable for the (101) facade, in contrast to the (001) facade where the surface trapping is much stronger, the subsurface trapping can partially account for the observed weaker photooxidative activity of the (101) compared to the (001) facade [28, 29].

VI. CONCLUSION

In conclusion, we have calculated optical charge transfer transitions of the O^- centers in anatase TiO_2. Bulk centers absorb at 600-750 nm, subsurface centers at 430-600 nm, whereas surface centers at >450nm. A picosecond blue shift of the transient absorption spectra can be associated with the photogenerated hole transfer to surfaces.

---

* `zawpaw@fysik.dtu.dk`

[1] J. Z. Zhang, J. Phys. Chem. B **104**, 7239 (2000).

[2] R. Berera, R. van Grondelle, and J. Kennis, Photosynth. Res. **101**, 105 (2009).

[3] M. Fox, *Optical properties of solids; 2nd ed.*, Oxford Master Series in Condensed Matter Physics (Oxford Univ. Press, Oxford, 2010).

[4] Y. Tamaki, A. Furube, R. Katoh, M. Murai, K. Hara, H. Arakawa, and M. Tachiya, C. R. Chim. **9**, 268 (2006).

[5] Y. Tamaki, K. Hara, R. Katoh, M. Tachiya, and A. Furube, J. Phys. Chem. C **113**, 11741 (2009).

[6] Y. Tamaki, A. Furube, M. Murai, K. Hara, R. Katoh, and M. Tachiya, J. Am. Chem. Soc. **128**, 416 (2006).

[7] Y. Tamaki, A. Furube, M. Murai, K. Hara, R. Katoh, and M. Tachiya, Phys. Chem. Chem. Phys. **9**, 1453 (2007).

[8] I. Shkrob and M. Sauer, J. Phys. Chem. B **108**, 12497 (2004).

[9] T. Yoshihara, R. Katoh, A. Furube, Y. Tamaki, M. Murai, K. Hara, S. Murata, H. Arakawa, and M. Tachiya, J. Phys. Chem. B **108**, 3817 (2004).

[10] J. Tang, J. R. Durrant, and D. R. Klug, J. Am. Chem. Soc. **130**, 13885 (2008).

[11] P. Zawadzki, K. W. Jacobsen, and J. Rossmeisl, Chem. Phys. Lett. **506**, 42 (2011).

[12] C. Di Valentin and A. Selloni, J. Phys. Chem. Lett. **2**, 2223 (2011).

[13] S. Yang, A. T. Brant, and L. E. Halliburton, Phys. Rev. B **82**, 035209 (2010).

[14] P. Zawadzki, K. Jacobsen, D. Søren, , and J. Rossmeisl, in preparation.

[15] J. Gavnholt, T. Olsen, M. Engelund, and J. Schiotz, Phys. Rev. B **78**, 075441 (2008).

[16] Y. Murakami, J. Nishino, T. Mesaki, and Y. Nosaka, Spectrosc. Lett. **44**, 88 (2011).

[17] A. Furube, T. Asahi, H. Masuhara, H. Yamashita, and M. Anpo, Chem. Phys. Lett. **336**, 424 (2001).

[18] X. Yang and N. Tamai, Phys. Chem. Chem. Phys. **3**, 3393 (2001).

[19] P. Zawadzki, J. Rossmeisl, and K. W. Jacobsen, Phys. Rev. B **84**, 121203 (2011).

[20] O. F. Schirmer, J. Phys.: Condens. Matter **18**, R667 (2006).

[21] T. Keil, Phys. Rev. **140**, A601 (1965).

[22] P. Zawadzki, J. Rossmeisl, and K. Jacobsen, in preparation.

[23] B. Hammer, L. B. Hansen, and J. K. Norskov, Phys. Rev. B **59**, 7413 (1999).

[24] J. Enkovaara, C. Rostgaard, J. J. Mortensen, J. Chen, M. Dulak, L. Ferrighi, J. Gavnholt, C. Glinsvad, V. Haikola, H. A. Hansen, et al., J. Phys.: Condens. Matter **22**, 253202 (2010).

[25] D. E. Skinner, D. P. Colombo, J. J. Cavaleri, and R. M. Bowman, J. Phys. Chem. **99**, 7853 (1995).

[26] D. Philip Colombo, K. A. Roussel, J. Saeh, D. E. Skinner, J. J. Cavaleri, and R. M. Bowman, Chem. Phys. Lett. **232**, 207 (1995).

[27] A. Furube, T. Asahi, H. Masuhara, H. Yamashita, and M. Anpo, J. Phys. Chem. B **103**, 3120 (1999).

[28] S. Liu, J. Yu, and M. Jaroniec, Chem. Mater. **23**, 4085 (2011).

[29] T. Ohno, K. Sarukawa, and M. Matsumura, New J. Chem. **26**, 1167 (2002).

[30] D. W. Bahnemann, M. Hilgendorff, and R. Memming, J. Phys. Chem. B **101**, 4265 (1997).